

**MOLECULAR SIMULATION OF THE  
ADSORPTION OF ORGANICS FROM WATER**

by

Ahmet Ozgur Yazaydin

A Dissertation

Submitted to the Faculty

of the

WORCESTER POLYTECHNIC INSTITUTE

in partial fulfillment of the requirements for the

Degree of Doctor of Philosophy

in

Chemical Engineering

February 2007

**MOLECULAR SIMULATION OF THE  
ADSORPTION OF ORGANICS FROM WATER**

by

Ahmet Ozgur Yazaydin

A Dissertation

Submitted to the Faculty

of the

WORCESTER POLYTECHNIC INSTITUTE

in partial fulfillment of the requirements for the

Degree of Doctor of Philosophy

in

Chemical Engineering

February 2007

APPROVED:

Prof. R.W. Thompson, Major Advisor

---

Prof. N.K. Kazantzis

---

Prof. N. A. Gatsonis

---

Prof. D. DiBiasio, Head of Department

---

## ABSTRACT

Molecular simulations have become an important tool within the last few decades to understand physical processes in the microscale and customize processes in the macroscale according to the understanding developed at the molecular level. We present results from molecular simulations we performed to study the adsorption of hazardous organics in nanoporous materials.

Adsorption of water in silicalite, a hydrophobic material, and the effect of defects were investigated by Monte Carlo simulations. Silanol nests were found to have a big impact on the hydrophobicity of silicalite. Even the presence of one silanol nest per unit cell caused a significant amount of water adsorption. We also investigated the effect of four different cations,  $H^+$ ,  $Li^+$ ,  $Na^+$ , and  $Cs^+$ . Their presence in silicalite increased the amount of water adsorbed.

Monte Carlo and molecular dynamics simulations of MTBE adsorption in silicalite, mordenite, and zeolite beta with different  $Na^+$  cation loadings were carried out. The results revealed the importance of the pore structure on the adsorption of MTBE. Although these three zeolites have similar pore volumes, zeolite beta, with its pore structure which is mostly accessible to MTBE molecules, is predicted to adsorb significantly more MTBE than silicalite and mordenite. The  $Na^+$  cation loading, up to four cations does not have a significant effect on the adsorption capacity of the zeolites studied here, however, for silicalite and zeolite beta increasing the  $Na^+$  content increases the amount adsorbed at very low pressures.

A new force field was developed by Monte Carlo simulations for 1,4-Dioxane, an important industrial solvent which has emerged as a potentially significant threat to

human health. The objective was to develop reliable atom-atom interaction parameters to use in the simulations of the adsorption of 1,4-Dioxane in different adsorbent materials. Predictions of critical point data, liquid and vapour densities, heats of vaporization with our new force field were in good agreement with experimental data and outperformed predictions from simulations with other force field parameters available in literature.

To obtain the isotherms of MTBE and 1,4-Dioxane adsorption from water in silicalite Monte Carlo simulations were performed. First we optimized the interaction parameters between the atoms of silicalite and the atoms of MTBE and 1,4-Dioxane. Using these optimized parameters we simulated the adsorption of MTBE and 1,4-Dioxane from water in silicalite. Despite the agreement of simulated and experimental isotherms of pure components, simulated isotherms of MTBE and 1,4-Dioxane adsorption from water in silicalite did not yield satisfactory results.

Monte Carlo simulations were performed to investigate the affinity between two hazardous materials, PFOA and 1,1-DCE; and four different zeolites. Binding energies and Henry's constants were computed. For both PFOA and 1,1-DCE zeolite-beta had the highest affinity. The affinity between activated carbon with polar surface groups and water, and 1,4-Dioxane were investigated to shed light on why activated carbon is ineffective to remove 1,4-Dioxane from water. Results showed that presence of polar surface groups increased the affinity between water and activated carbon, while the affinity between 1,4-Dioxane and activated carbon was not effected by the presence of polar surface groups.

*To my grandmother*

*Melihat Aras*

## ACKNOWLEDGEMENTS

I would like to sincerely thank to Professor Robert W. Thompson for his guidance and especially for his friendship throughout my PhD years at WPI. His great communication skills with his students and his famous open door policy deserve strong appreciation. I will always remember him as a good friend and mentor, and with his miller time escapes. I extend my thanks to my mom and dad, Civan and Nedim Yazaydin, and my brother Bahadir Yazaydin for always being there to support me while pursuing my degree in US far from my home. I want to thank to my committee members Professor Kazantzis and Professor Gatsonis for carefully evaluating my thesis. Many thanks go to Dr. Marcus G. Martin who generously hosted me at Sandia National Labs, despite my red badge, during the 2006 summer and helped me to improve my skills on molecular simulation with his experience, and also many thanks to his Towhee project for giving me a chance to contribute to the molecular simulation community. I sincerely appreciate the support of my labmate Rasesh and my dear friend Ertan and his wife Nuriye while walking on the same path together for our degrees. WPI Unix systems administrator Josh Brandt also deserves a lot of credit and thanks for giving enormous technical support for computing clusters, without him running jobs would be very uneasy. I also want to thank to Alex, my work-study student, for bailing me out on the deadline of my thesis submission to the committee, and his useful help in the lab. I also can not forget the support of our former department secretary Joe Kaupu and his Hawaiian smile in our first days at WPI. Finally, my roommates Joseph Policelli, Bulent Ataman, Mehmet Hergunsel and Kevin (Seung-Han) Lee, thank you for making 20 Bergin Lane a great place to live.

## TABLE of CONTENTS

ABSTRACT.....	iii
ACKNOWLEDGEMENTS.....	vi
TABLE of CONTENTS .....	vii
LIST of FIGURES .....	iv
LIST of TABLES .....	ix
1. INTRODUCTION and THEORY.....	1
1.1. Forcefield.....	3
1.1.1. Intermolecular Potentials.....	3
1.1.1.1. Electrostatic Potentials.....	3
1.1.1.2. Van der Waals Potentials.....	4
1.1.2. Intramolecular Potentials.....	5
1.1.2.1. Bond Stretching.....	6
1.1.2.2. Angle Bending.....	6
1.1.2.3. Dihedral Angle.....	7
1.1.3. Forcefield Parameterization.....	9
1.2. Molecular Dynamics Simulations.....	9
1.3. Monte Carlo Simulations.....	12
1.3.1. Grand Canonical Monte Carlo (GCMC).....	14
1.3.2 Gibbs Ensemble Monte Carlo (GEMC).....	15
1.3.3 Single Box Monte Carlo Simulations in NPT and NVT Ensembles.....	16

1.4. Nanoporous Materials of Interest.....	17
1.5. Objectives.....	30
Bibliography.....	31
2. MOLECULAR SIMULATION of WATER ADSORPTION in SILICALITE: EFFECT OF SILANOL GROUPS AND DIFFERENT CATIONS.....	32
2.1. Introduction.....	32
2.2. Models and Methods .....	34
2.2.1. Silicalite and Water Model .....	34
2.2.2. Force Field.....	35
2.2.3. Chemical Potential of Water in the Gas Phase.....	36
2.2.4. Optimization of Silicalite Structure with Defects.....	37
2.2.5. Simulation of the Adsorption Isotherms.....	37
2.3. Results and Discussion.....	38
2.3.1. Effect of Silanol Nests.....	39
2.3.2. Effect of Cations.....	42
2.4. Conclusions.....	44
Bibliography.....	46
3. MOLECULAR SIMULATION of THE ADSORPTION of MTBE in SILICALITE, MORDENITE, and ZEOLITE BETA .....	50
3.1. Introduction.....	50
3.2. Theoretical Models and Calculations .....	52
3.3. Results and Discussion.....	57
3.4. Conclusions.....	65
Bibliography.....	66
4. SIMULATING the VAPOUR-LIQUID EQUILIBRIA of 1,4-DIOXANE.....	71

4.1. Introduction.....	71
4.2. Model and Simulation Details .....	73
4.3. Results and Discussion.....	77
4.4. Conclusions.....	84
Bibliography.....	86
5. MOLECULAR SIMULATION of LIQUID PHASE ADSORPTION of MTBE and 1,4-DIOXANE from WATER .....	90
5.1. Introduction.....	90
5.2. Models and Methods .....	91
5.2.1. Silicalite, Water, MTBE and 1,4-Dioxane Models .....	91
5.2.2. Force Field.....	92
5.2.3. Fugacities of the Species in the Gas Phase .....	93
5.2.4. Chemical Potential of Species in the Gas Phase .....	94
5.2.5. Simulation of the Adsorption Isotherms .....	95
5.3. Results and Discussion.....	95
5.3.1. Adsorption of MTBE and 1,4-Dioxane from the Gas Phase Silicalite, Water, MTBE and 1,4-Dioxane Models .....	95
5.3.2. Adsorption of MTBE and 1,4-Dioxane from Water.....	99
5.4. Conclusions.....	102
Bibliography.....	103
6. COMPUTING BINDING ENERGIES and HENRY'S CONSTANTS from MOLECULAR SIMULATIONS .....	105
6.1. Introduction.....	105
6.2. Models and Methods .....	107
6.2.1. Zeolite, Activated Carbon, PFOA, 1,1-DCE, 1,4-Dioxane and Water Models .....	107
6.2.2. Force Field.....	109
6.2.3. Simulations.....	113
6.3. Results and Discussion.....	114
6.3.1. PFOA and 1,1-DCE .....	114

6.3.2. Water and 1,4-Dioxane .....	115
6.4. Conclusions.....	116
Bibliography.....	117
7. CONCLUDING REMARKS and RECOMMENDATIONS for FUTURE RESEARCH .....	119
APPENDIX	

## LIST of FIGURES

1.1. Van der Waals potential.....	5
1.2. Bonding between two atoms.....	6
1.3. Valence angle between two bond vectors.....	7
1.4. Dihedral angle between two planes.....	8
1.5. Schematic of GEMC [from reference 8].....	16
1.6. Silicalite. Y-Z plane .....	18
1.7. Silicalite. X-Z plane .....	19
1.8. Silicalite. X-Y plane .....	20
1.9. Mordenite. Y-Z plane .....	21
1.10. Mordenite. X-Z plane.....	22
1.11. Mordenite. X-Y plane .....	23
1.12. Zeolite-beta. Y-Z plane .....	24
1.13. Zeolite-beta. X-Z plane .....	25
1.14. Zeolite-beta. X-Y plane .....	26
1.15. Zeolite-Y. Y-Z plane .....	27
1.16. Zeolite-Y. X-Z plane .....	28
1.17. Zeolite-Y. X-Y plane .....	29
2.1. Gas phase water adsorption isotherms in silicalite: (♦) simulation <sup>22</sup> at 300 K, (□) experiment <sup>16</sup> at 303 K, (▲) experiment <sup>18</sup> at 303 K, (■) experiment <sup>16</sup> at 298.15 K, (○) experiment <sup>5</sup> at 298.15 K, (*) experiment <sup>15</sup> at 298.15 K, (●) experiment <sup>17</sup> at 298.15 K.....	39
2.2. Gas phase water adsorption isotherms in silicalite: (♦) simulation <sup>22</sup> at 300 K - siliceous, (■) simulation <sup>this work</sup> at 298.15 K - siliceous, (▲) simulation <sup>this work</sup> at 298.15 K - 1 silanol nest per unit cell, (○) simulation <sup>this work</sup> at 298.15 K - 2 silanol nests per unit cell, (*) simulation <sup>this work</sup> at 298.15 K - 3 silanol nests per unit cell, (□) simulation <sup>this work</sup> at 298.15 K - 4 silanol nests per unit cell.....	40
2.3. Snapshot of a silanol nest. (yellow) silicon atoms, (red) oxygen atoms, (white) hydrogen atoms.....	41

2.4. Gas phase water adsorption isotherms in silicalite: (♦) simulation <sup>this work</sup> at 298.15 K – 3 silanol nests per unit cell, (Δ) simulation <sup>this work</sup> at 298.15 K - 4 silanol nests per unit cell, (□) experiment <sup>16</sup> at 303 K, (▲) experiment <sup>18</sup> at 303 K, (■) experiment <sup>16</sup> at 298.15 K, (○) experiment <sup>5</sup> at 298.15 K, (*) experiment <sup>15</sup> at 298.15 K, (●) experiment <sup>17</sup> at 298.15 K.....	42
2.5. Gas phase water adsorption isotherms in silicalite: (♦) simulation <sup>this work</sup> at 298.15 K - siliceous, (□) experiment <sup>16</sup> at 303 K, (▲) experiment <sup>18</sup> at 303 K, (■) experiment <sup>16</sup> at 298.15 K, (○) experiment <sup>5</sup> at 298.15 K, (*) experiment <sup>15</sup> at 298.15 K, (●) experiment <sup>17</sup> at 298.15 K.....	43
2.6. Gas phase water adsorption isotherms in silicalite: (♦) simulation <sup>this work</sup> at 298.15 K - siliceous, (■) simulation <sup>this work</sup> at 298.15 K – 2 Cs <sup>+</sup> per unit cell, (▲) simulation <sup>this work</sup> at 298.15 K – 2 H <sup>+</sup> per unit cell, (○) simulation <sup>this work</sup> at 298.15 K – 2 Li <sup>+</sup> per unit cell, (*) simulation <sup>this work</sup> at 298.15 K – 2 Na <sup>+</sup> per unit cell.....	44
3.1. Comparison of MTBE adsorption in siliceous zeolites: (♦) silicalite, (□) mordenite and (Δ) beta. Lines represent fitted curves.....	59
3.2. Effect of increasing Na <sup>+</sup> content on MTBE adsorption in silicalite: (♦) siliceous, (Δ) Si/Al=195 and (*) Si/Al=97. Lines represent the fitted curves.....	59
3.3. Effect of increasing Na <sup>+</sup> content on MTBE adsorption in mordenite: (♦) siliceous, (Δ) Si/Al=195 and (*) Si/Al=97. Lines represent the fitted curves.....	60
3.4. Effect of increasing Na <sup>+</sup> content on MTBE adsorption in zeolite beta: (♦) siliceous, (Δ) Si/Al=127 and (*) Si/Al=63. Lines represent the fitted curves.....	61
3.5. Orientation of MTBE molecule near Na <sup>+</sup> cation in silicalite (Si/Al=97). MTBE oxygen atom (white), carbon (cyan), zeolite oxygen (red), silicon (yellow), aluminium (green), Na <sup>+</sup> (blue).....	62
3.6. Effect of aluminium site distribution on the adsorption of MTBE in zeolite beta (Si/Al=63): (♦) aluminium sites were kept as far as possible from each other, (□) aluminum sites are only separated by an O-Si-O bridge. ....	63

3.7. Comparison of RDF of oxygen atoms of liquid MTBE (—) and RDFs of oxygen atoms of MTBE adsorbed in siliceous silicalite (- - -), mordenite (- -) and zeolite beta (- · -).	64
4.1. Vapour-liquid coexistence curve for 1,4-dioxane. New force field (○), Trappe-UA (□), OPLS-UA (Δ), Geerlings (◇) <sup>14</sup> , Krienke (+) <sup>15</sup> , Experimental critical data (*). Solid lines represent the experimental liquid densities <sup>31</sup> and vapour densities calculated from the experimental vapour pressure <sup>33</sup> using Pitzer's <sup>34</sup> method.	79
4.2. A magnified view of the vapour densities. New force field (○), Trappe-UA (□), OPLS-UA (Δ), Geerlings (◇) <sup>14</sup> , Krienke (+) <sup>15</sup> . Solid line represent the vapour densities calculated from the experimental vapour pressures <sup>33</sup> using Pitzer's <sup>34</sup> method.	80
4.3. Radial distribution functions of O-O (- - -), CH <sub>2</sub> -O (— — —), CH <sub>2</sub> - CH <sub>2</sub> (——) pairs of 1,4-Dioxane molecule in the vapour phase at 298.15 K.	81
4.4. Liquid densities of 1,4-Dioxane. New force field 180 molecules (○), New force field 300 molecules (□). Solid line represent the experimental liquid densities. <sup>31</sup>	83
4.5. Vapour densities of 1,4-Dioxane. New force field 180 molecules (○), New force field 300 molecules (□). Solid lines represent the vapour densities calculated from the experimental vapour pressures <sup>33</sup> using Pitzer's <sup>34</sup> method.	84
5.1. Binary-mixture three phase equilibrium. Equilibrium between liquid and gas can be calculated with an EOS model. GCMC simulations can calculate equilibrium between gas and zeolite. (from reference 3)	91
5.2. Gas phase pure MTBE adsorption isotherms in silicalite: (◇) experiment <sup>23</sup> at 425.15 K, (□) simulation at 425.15 K.	96
5.3. Gas phase pure MTBE adsorption isotherms in silicalite: (◇) experiment <sup>23</sup> at 448.15 K, (□) simulation 448.15 K.	96
5.4. Gas phase pure MTBE adsorption isotherms in silicalite: (◇) experiment <sup>23</sup> at 473.15 K, (□) simulation at 473.15 K.	97
5.5. Gas phase pure MTBE adsorption isotherm in silicalite:(□) simulation at 298.15K.	97

5.6. Gas phase pure 1,4-Dioxane adsorption isotherms in silicalite: ( $\diamond$ ) experiment <sup>8</sup> at 298.15 K, ( $\square$ ) simulation at 298.15 K .....	98
5.7. Isotherms of MTBE adsorption from water in silicalite at 298.15 K: ( $\diamond$ ) experiment <sup>24</sup> , ( $\circ$ ) simulation (OZ $\varepsilon = 150$ K), ( $\square$ ) simulation, (OZ $\varepsilon = 260$ K) .....	100
5.8. Isotherm of 1,4-Dioxane adsorption from water in silicalite: ( $\diamond$ ) simulation at 298.15 K. ....	101
6.1. 1,1-Dichloroethylene.....	106
6.2. Perfluorooctanoic Acid.....	107
6.3. Schematic representation for the simulated carbon slit pores. Three carbon layers are considered both above and below the pore. (from reference 25).....	108
6.4. Schematic representation of the polar surface sites studied in this work: (a) a carboxyl group; (b) a hydroxyl group; (c) a carbonyl group. (from reference 1) .....	109

## LIST of TABLES

2.1. Silicalite-Water Non-bonded force field parameters.....	34
3.1. Zeolite-MTBE nonbonded force field parameters .....	53
3.2. Pore volumes (cm <sup>3</sup> /gr) of silicalite, mordenite and zeolite beta.....	57
4.1. Non-bonded force field parameters used in this study. ....	73
4.2. Parameters for intramolecular terms.....	74
4.3. Comparison of the critical density and temperature obtained from experiments and simulations with the new force field. The subscripts denote the statistical uncertainties in the last digit(s) where available.....	77
4.4. Compressibility factors calculated from experimental vapour pressure data and those computed from simulations with new force field. The subscripts denote the statistical uncertainties in the last digit(s) where available.....	80
5.1. Force field parameters.....	93
6.1. Geometric Parameters for Polar Surface Groups on Graphite Surface.....	109
6.2. Non-bonded Forcefield Parameters for Zeolite Atoms and 1,1-DCE, and PFOA.....	111
6.3. Non-bonded Forcefield Parameters for Graphite Plates, Polar Surface Groups, Water and 1,4-Dioxane.....	112
6.4. Binding Energies and Henry's Constants of PFOA and 1,1-DCE in silicalite, mordenite, zeolite-beta, zeolite-Y. ....	114
6.5. Binding Energies and Henry's Constants of Water and 1,4-Dioxane in activated carbon pore with polar surfaces of carbonyl, carboxyl, and hydroxyl.....	115

## 1. INTRODUCTION and THEORY

The rapid increase of computer power opened the way for simulating various systems and physical processes within the atomic scale. Today we call this field of science *molecular modeling*. Atomic scale computer simulations can be used for many different applications. A few of them are, but not limited to, drug design, protein engineering, environmental processes and materials science. Computer simulations are useful when the experimental procedure is costly, time consuming or practically impossible. Besides, many thermophysical properties can be evaluated using the results obtained from simulations. Density, free energy, specific heat, viscosity and average structure are some of the properties we can estimate with computer simulations. In light of this brief summary it is fair to say that molecular modeling is a branch of science which carries the scientist and the experiment to our desktop computers, giving us the opportunity to make *computer experiments*.

In theory one can simulate any system regardless of its size. However, even though we have reached a tremendous computational power, today we are capable of simulating number of atoms in the order of  $10^6$ . This means we can only deal around  $10^{-17}$  mole of a substance. Although this seems small, simulating a mole of a substance is not really the main objective of molecular modeling. Information we gather within this scale is often difficult, expensive and sometimes dangerous to obtain with experiments.

Accuracy of computer simulations depends on the reliability of the computational procedure which is also called *algorithm*. So far scientists have done a good job to develop reliable algorithms. Today, developing faster and more efficient algorithms has a very important place for the research community.

Another important point, and perhaps the most important, to be assessed is the interaction potential which describes the relation between the atoms. Interaction potentials are often called a *forcefield*. A forcefield is a set of equations which analytically formulates the interaction of atoms between each other. These interaction potentials are usually classified in to two groups; *intermolecular* and *intramolecular*. Intermolecular potentials are further divided in to two groups as *electrostatic* and *Van der Waals* potentials. While intermolecular potentials are used for the atoms which don't belong to the same molecule or separated by more than two bonds within the same molecule, intramolecular potentials deal with atoms bonded to each other. Usually forcefield equations are distance dependent equations with parameters to model the behavior of the specific interaction between the atoms. Parameterization of these equations can be achieved by two means. First is fitting of parameters to the experimental quantities such as liquid and vapor densities, heat of adsorption, dipole moment or heat of vaporization. Second method is from the core of molecular modeling, quantum mechanical calculations. A detailed explanation of how a forcefield is handled for molecular simulations will be given in the next section.

Molecular simulation is an excellent tool for investigating nanoscale systems. Fluid behavior confined in nanoporous materials is an active research area. Due to their dimensions, nanopores are not easily accessible to experimental methods. Therefore, molecular simulations can provide us useful information such as density, dipole moment, diffusion coefficient, flux of molecules through nanopores, adsorption isotherms and preferred adsorption sites. In this study we used molecular simulation techniques to investigate adsorption of several molecules in different nanoporous materials.

A summary of the theory behind the molecular simulation methods is essential to understand how they are used to study the systems of interest. This chapter will cover two different methods of atomistic simulations, *Molecular Dynamics* and *Monte Carlo*. A key assumption which is valid for both of the methods is the *Born-Oppenheimer* approximation. The Born-Oppenheimer approximation is a technique used in quantum chemistry and condensed matter physics in order to de-couple the motion of nuclei and electrons. It is based on the fact that typical electronic velocities far exceed those of nuclei. Since nuclear motion is much slower than electron motion the electronic wavefunction, or energies, can be calculated assuming a fixed position of the nuclei and nuclear motion can be considered assuming an average distribution of electron density. Without this approximation it is impossible to write the energy as a function of the nuclear coordinates. This approximation is required since many of the problems that we are interested in molecular modeling are too large to be considered by quantum mechanics.<sup>1</sup> Both Molecular Dynamics and Monte Carlo simulations require a forcefield, a set of equations with parameters describing the interactions between atoms. Therefore, a fundamental understanding of a forcefield is important.

## **1.1. Forcefield**

A forcefield has two main parts, intermolecular and intramolecular potentials. Intermolecular potentials are further divided in to two groups as electrostatic and Van der Waals potentials.

### **1.1.1. Intermolecular Potentials**

**1.1.1.1. Electrostatic Potentials.** Electrostatic Potentials arise from interactions due to the unequal charge distribution over the atoms of a molecule. A common way of

representing this charge distribution in a forcefield is to place partial charges on atoms. These charges are determined so that they represent the electrostatic properties of the molecules. The electrostatic interaction between two atoms is calculated according to Coulomb's law:

$$U_{el} = \frac{q_i q_j}{r_{ij}} \quad (1)$$

Partial charges are not experimentally observable quantities and can not be calculated from the wavefunction unambiguously. Different approaches are available in literature to calculate them. A simple yet powerful approach is to place charges on the atoms so that it represents the multiple moments of the molecule such as dipole and quadrupole moment. In some cases the atomic charges are chosen to reproduce the thermodynamic properties of a molecule. In this approach a series of simulations is performed until the results of the simulation agrees with the experiment. Another way of calculating the partial charges is to derive them from the molecular electrostatic potential. The electrostatic potential at a point is the force acting on a unit positive charge placed at that point. The objective is to obtain the partial charges that reproduce the electrostatic potential at a number of points surrounding the molecule.

**1.1.1.2. Van der Waals Potential.** Van der Waals Potential is a short range interaction which has a repulsive and an attractive term. The attractive contribution is due to dispersive forces. Dispersive forces arise from fluctuations which creates instantaneous dipoles. This instantaneous dipole induces a dipole in a nearby molecule giving rise to an attractive inductive effect.

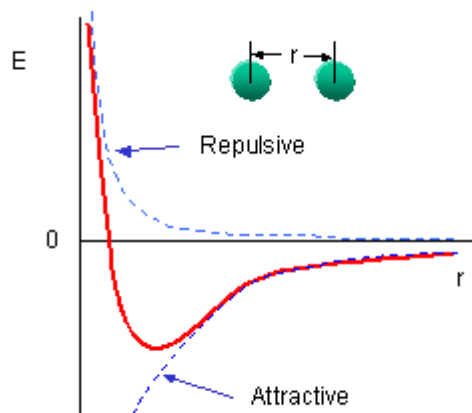


Figure 1.1. Van der Waals potential

This interaction is especially dominant within 3-4 Å surrounding the collision diameter of an atom. A typical picture of how Van der Waals potential varies with distance is shown in Figure 1.1. As two atoms come closer the attractive force smoothly increases. When they are too close repulsive force increases sharply.

The most famous function which models the Van der Waals interaction is the *Lennard-Jones 12-6* potential:

$$U_{vw}(r) = 4\varepsilon \left[ \left( \frac{\sigma}{r} \right)^{12} - \left( \frac{\sigma}{r} \right)^6 \right] \quad (7)$$

The Lennard-Jones 12-6 potential has two parameters, the collision diameter  $\sigma$ , at which the energy is zero and the well depth  $\varepsilon$ , where the net force is zero. The repulsive term varies as  $r^{-12}$  and the attractive term varies as  $r^{-6}$ .

### 1.1.2. Intramolecular Potentials

Atoms bonded to each other directly or linked to each other with maximum three bonds in series account for the intramolecular interactions. There are three main components of intramolecular interactions.

### 1.1.2.1. Bond Stretching

Bond stretching describes a bond between two atoms. They are functions of the interatomic distance only.

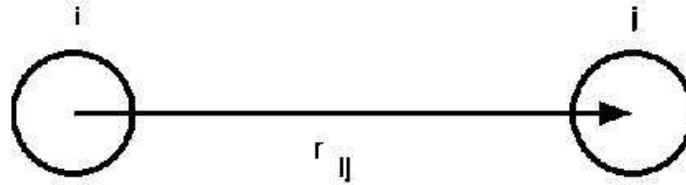


Figure 1.2. Bonding between two atoms

A useful way of modeling the bond is assuming that two atoms are connected with a spring. This lets us to use a Hooke's law formula in which the bond energy varies with the square of the displacement from the reference bond length,  $r_0$ :

$$U_{bond}(r) = k(r_{ij} - r_0)^2 \quad (8)$$

where  $r_{ij}$  is the distance between two atoms and  $k$  is the force constant.

### 1.1.2.2 Angle Bending

Angle bending is the interaction of two atoms which are bonded to a common atom. Again here, a spring type interaction between two atoms is a common way of modeling. This time the spring is assumed to act between two atoms bonded to a common atom. Energy varies with the square of the displacement from the reference angle,  $\theta_0$ :

$$U_{angle}(\theta) = k(\theta_{ijk} - \theta_0)^2 \quad (9)$$

where  $\theta_{ijk}$  the angle between two bond vectors and  $k$  is the force constant. Intermolecular potentials are not calculated between atoms bonded to each other or bonded to a common atom.

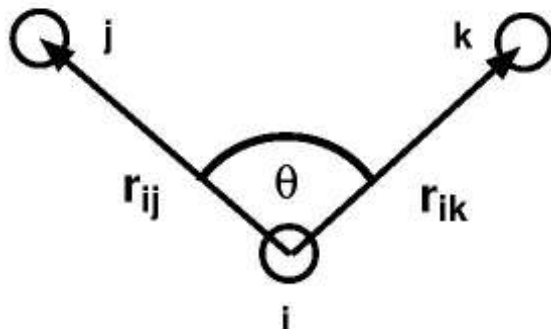


Figure 1.3. Valence angle between two bond vectors

### 1.1.2.3. Dihedral Angle

Dihedral angle potential describes the interaction arising from torsional forces in molecules. It requires the specification of four atomic positions. Figure 1.4 shows the dihedral angle between two planes where bond vectors lie. Dihedral angle potential is a barrier to rotation around chemical bonds; therefore, it plays an important role on the conformation of a molecule. Unlike bond stretching and angle bending the spring assumption is not a common method for modeling the dihedral angle potential. Often dihedral angle potential is calculated regardless of a reference angle value. A frequently used formula is the so-called the triple cosine function:

$$U_{dihedral} = k_1(1 + \cos(\phi)) + k_2(1 - \cos(2\phi)) + k_3(1 + \cos(3\phi)) \quad (10)$$

Dihedral angle potential is a barrier to rotation around chemical bonds; therefore, it plays an important role on the conformation of a molecule. For instance, fluctuation of

cyclohexane between its chair and boat conformation, or cis-trans conformation of dichloroethylene are all related with the dihedral angle potential.

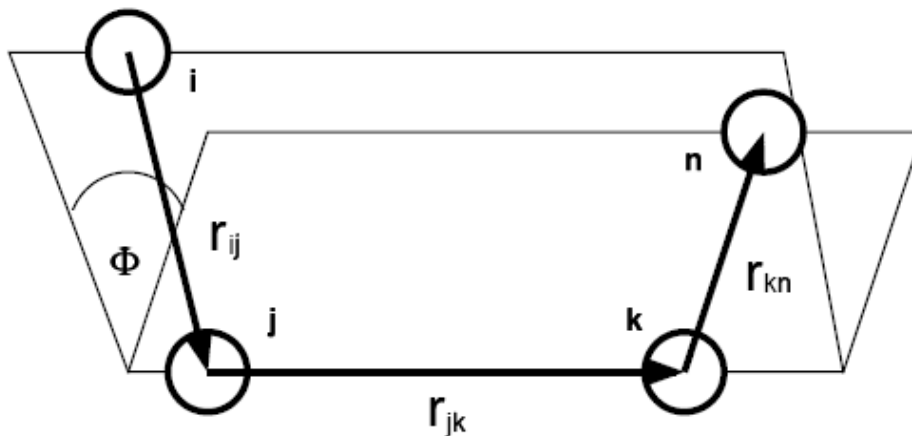


Figure 1.4. Dihedral angle between two planes

A unique property of the dihedral angle potential is that intermolecular interactions are also calculated with a scaled magnitude besides the intramolecular portion. But this only applies to the 1<sup>st</sup> and the 4<sup>th</sup> atom. In Figure 1.4 these atoms are marked by i and n.

Bond stretching and angle bending terms are difficult to distort from their reference values. A substantial amount of energy is required to cause deformations in bonds and angles. Most of the variation in structure of molecules and relative energies is due to the non-bonded and torsional contributions.

As a result a complete forcefield is formed from several terms and can be written as a sum of them

$$U_{total} = U_{el} + U_{VW} + U_{bond} + U_{angle} + U_{dihedral} \quad (11)$$

### 1.1.3. Forcefield Parameterization

A force field can contain a large number of parameters, such as  $\epsilon$  and  $\sigma$  in the Lennard-Jones potential and the force constants,  $k$ , in the intramolecular potentials, even if it is intended for calculations on only a small set of molecules. Parameterization of a force field is not a trivial task. A significant amount of effort is required to create a new force field entirely from scratch.

The first step is to select the data that are going to be used. Force fields may be used to determine a variety of structurally related properties or to reproduce thermodynamic properties. Unfortunately, experimental data may not exist or difficult to obtain for particular classes of molecules. Quantum mechanics calculations are thus increasingly used to provide the data for the parameterization of the force fields.

Once a functional form for the force field has been chosen and the data to be used in the parameterization identified there are two ways to obtain the parameters. The first option is parameterization by trial and error, in which the parameters are gradually refined to give better agreement and better fits to the data. The second option to parameterization is to use least-squares fitting to determine the set of parameters that gives the optimal fit to the data. The objective is to change the force field parameters to minimize the fitting error.<sup>1</sup>

## 1.2. Molecular Dynamics Simulations

We call *molecular dynamics* (MD) a computer simulation technique where successive generations of the system are generated by integrating the Newton's laws of motion. The second law of Newton says Force equals the rate of change of momentum.

$$F_i = m_i \frac{d^2 r_i}{dt^2} \quad (12)$$

This equation describes the motion of a particle with a mass of  $m$  on a certain coordinate with  $F$  being the force exerted on the particles. This law allows us to determine how the trajectory of the system varies by time.<sup>2</sup>

In a molecular dynamics simulation a series of calculations are repeated every step to determine how the system evolves with time. First, initial positions of the atoms are taken. Second, each atom is assigned a random velocity based on Maxwell-Boltzmann distribution for the temperature of interest using the relation

$$\sum_{i=1}^N \frac{1}{2} m_i v_i^2 = \frac{3}{2} N k_b T \quad (13)$$

So up to here we have the initial position and the velocity of the atoms. Third, the force applied on each atom is calculated based on the potentials in the forcefield.

$$F = -\frac{dU}{dr} \quad (14)$$

Now we know the force acting on an atom, so using Newton's equation we can calculate the velocity and position of an atom at a new time, which is the fourth and most important step in molecular dynamics calculations. At the fifth and final step the force is recalculated using the new position and velocity of the atoms. The rest of the simulation continues with repeating steps four and five.

The fourth step above requires a numerical integration for the evaluation of the velocity. Numerous algorithms were proposed for this integration. Most famous and perhaps most widely used is the Verlet algorithm. We start by writing two third-order Taylor expansions of for the positions  $r(t)$ , one of them is forward and the other one is backward in time.

$$\mathbf{r}(t + \Delta t) = \mathbf{r}(t) + \mathbf{v}(t)\Delta t + (1/2)\mathbf{a}(t)\Delta t^2 + (1/6)\mathbf{b}(t)\Delta t^3 + O(\Delta t^4)$$

$$\mathbf{r}(t - \Delta t) = \mathbf{r}(t) - \mathbf{v}(t)\Delta t + (1/2)\mathbf{a}(t)\Delta t^2 - (1/6)\mathbf{b}(t)\Delta t^3 + O(\Delta t^4)$$

Next we add these two expressions to obtain

$$\mathbf{r}(t + \Delta t) = 2\mathbf{r}(t) - \mathbf{r}(t - \Delta t) + \mathbf{a}(t)\Delta t^2 + O(\Delta t^4)$$

Since we are integrating Newton's equations,  $\mathbf{a}(t)$  can be obtained from force, which is the derivative of potential with respect to  $\mathbf{r}(t)$ , divided by mass:

$$\mathbf{a}(t) = -\frac{1}{m}\nabla U(\mathbf{r}(t))$$

This is the basic form of the Verlet algorithm. Positions and accelerations at time  $t$ , and the positions from the previous step,  $\mathbf{r}(t-\Delta t)$ , to calculate the new positions  $\mathbf{r}(t+\Delta t)$ . As can be seen truncation error of the algorithm is in the order of  $\Delta t^4$ . A practical problem with Verlet algorithm is that velocities are not directly generated. While velocities are not required for the time evolution they are important for computing system properties such as the kinetic energy. Therefore an improved implementation of the same algorithm was developed which is the so-called velocity Verlet scheme. In this version positions, velocities and accelerations at time  $(t+\Delta t)$  are computed from the same quantities at time  $t$  as follows.

$$\mathbf{r}(t + \Delta t) = \mathbf{r}(t) + \mathbf{v}(t)\Delta t + (1/2)\mathbf{a}(t)\Delta t^2$$

$$\mathbf{v}(t + \Delta t / 2) = \mathbf{v}(t) + (1/2)\mathbf{a}(t)\Delta t$$

$$\mathbf{a}(t + \Delta t) = -\frac{1}{m}\nabla U(\mathbf{r}(t + \Delta t))$$

$$\mathbf{v}(t + \Delta t) = \mathbf{v}(t + \Delta t / 2) + (1/2)\mathbf{a}(t + \Delta t)\Delta t$$

### 1.3 Monte Carlo Simulations

The idea of Monte Carlo simulations is to generate randomly a large set of configurations and to compute the average of some quantity of the system. Due to randomness to generate and accept or reject trial moves in the mechanism of this simulation method, it is named after the famous gambling location Monte Carlo in Europe. A Monte Carlo simulation is used in order to sample configurations according to a statistical mechanical ensemble. A system can be in a certain state with a certain probability. This is expressed as

$$\rho_i = \frac{\exp[-\beta U(\mathbf{r}_i)]}{\int_r \exp[-\beta U(\mathbf{r})] d\mathbf{r}} \quad (15)$$

where  $\rho_i$  is the probability that the system is in state  $i$ . This is the idea behind Monte Carlo simulation.

The main algorithmic challenge of designing a Monte Carlo molecular simulation lies in finding ways to adequately and efficiently sample the equilibrium distribution of the correct statistical mechanical ensemble. Metropolis et al.<sup>3</sup> were the first to show that you can sample such a distribution by treating the problem as if it were a Markov chain. A Markov chain is a collection of states where the probability of moving from one state to another depends only upon the state that the system is currently staying in, no matter how the system got into that current state. The trick is to select the probabilities of moving from one state to another in such a way that the system converges to a stationary distribution with the probabilities given in equation 15.

Let us consider a system of particles in a periodic box. A Monte Carlo move is an attempt to change the system from one state to another. In this system the only move that

is required to equilibrate the system is a translational move. The algorithm for a translational move is as follows.

- 1) Randomly choose a particle in the system.
- 2) Displace that particle in a random direction by a fraction of the maximum desired displacement.
- 3) Compute the potential energy change  $[U(r_{\text{new}}) - U(r_{\text{old}})]$  caused by moving this particle from its old location to the new location.
- 4) Accept or reject the move according to the acceptance probability

$$A_{old \rightarrow new} = \min[1, \exp(-\beta[U(r_{\text{new}}) - U(r_{\text{old}})])] \quad (16)$$

If the energy change is negative, which means that the system moved to a lower energy state, then the exponential term is greater than 1 and the move is accepted with probability 1. If the energy change is positive, then the move is accepted with probability  $\exp(-\beta[U(r_{\text{new}}) - U(r_{\text{old}})])$ . This is done by computing a random number  $Z$  that is uniformly distributed over the interval (0,1). If  $Z$  is less than  $\exp(-\beta[U(r_{\text{new}}) - U(r_{\text{old}})])$ , then the move is accepted and the new configuration of the system is counted in the averaging, otherwise the molecule is returned to its original location and the old configuration is counted again in the averaging. This is generally how a Monte Carlo simulation progresses.<sup>4</sup>

In theory, the Metropolis translation move is sufficient to sample a system. In practice, many other different kinds of moves are also utilized in order to reduce the amount of computer time required to get good convergence to the stationary distribution, and also to sample different ensembles. Particle insertion/deletion, molecule regrowth and volume exchange moves are also widely used. Regrowth move is useful when

translating long chains or big molecules. Instead of translating the center of mass of a molecule an atom of the molecule is randomly selected and rest of the molecule is constructed in a randomly chosen direction. This move is particularly useful for molecules in nanoporous materials. Particle insertion/deletion move is unique to the Grand Canonical Ensemble ( $\mu VT$ ) where the number of particles is not constant. Volume exchange move is used in Canonical Ensemble (NVT) or Isobaric-Isothermal Ensemble (NPT). There are two different types of volume exchange moves. The first type is used in the NPT ensemble where a simulation box exchanges volume with an infinitely large pressure bath to keep the pressure constant. The second type of the volume exchange move is used in the NVT ensemble. In this case there are two boxes and these boxes exchange volume with each other provided that the total volume of the boxes is kept constant. In a Monte Carlo simulation if there are two boxes performing any type of the two volume exchange moves and at the same time if these boxes are exchanging particle between each other then this ensemble is called Gibbs Ensemble. Monte Carlo simulations in Grand Canonical Ensemble and Gibbs Ensemble were used several times in this study and a basic understanding and a brief background about the features of these two simulation methods is crucial.

### **1.3.1. Grand Canonical Monte Carlo (GCMC)**

In the Grand Canonical Monte Carlo simulations chemical potential of the molecules ( $\mu$ ), temperature ( $T$ ), and volume ( $V$ ) of the system are fixed.<sup>5</sup> GCMC has many useful applications because it models a system that is in equilibrium with a bulk fluid at a specified chemical potential. Molecule insertions and deletions are used to achieve equilibrium with the bulk fluid. GCMC is used to obtain the adsorption isotherms

of compounds in nanoporous materials. The idea is to exchange particles between a large gas reservoir with a fixed chemical potential and the pores. Exchanging particles means to insert particles from the gas reservoir and delete particles from the pores. GCMC has the negative feature that it fails or becomes difficult to converge in case the insertions are towards highly dense fluids or solids. Because, the probability of an insertion being successful in highly dense systems is low.

### **1.3.2 Gibbs Ensemble Monte Carlo (GEMC)**

One of the very significant recent developments in molecular simulation was the development of the Gibbs Ensemble Monte Carlo (GEMC) method by Panagiotopoulos.<sup>6,7</sup> The GEMC method allows the calculation of phase equilibria for both pure fluids and mixtures. Furthermore, the critical properties predicted by a given forcefield could be calculated, and the forcefield tuned to reproduce the phase envelope and critical point accurately. The technique, illustrated in Figure 1.5, involves the direct simulation of two fluid phases in equilibrium, though not in physical contact. Two simulation cells, each corresponding to a fluid phase, are brought to phase equilibria by a combination of displacement, volume exchange and molecule exchange moves with acceptance criterion designed to ensure that the conditions of phase equilibrium are met.

If the goal is to know the densities, compositions and pressure of the two coexisting phases at equilibrium, then GEMC is a very efficient because no interface is present in the simulation. Instead, the two boxes in the simulation represent samples from the bulk regions of the coexisting phases. If the system of interest is a binary mixture then the simulation is performed in the NPT ensemble. Boxes exchange volume with an infinitely large pressure bath to keep the pressure fixed. They also exchange molecules

between each other. Eventually in separate boxes two phases occur with a certain composition. On the other hand, if we have a pure fluid total volume of the boxes is kept fixed; however, they are free to exchange volumes and molecules with each other.

The primary advantage of GEMC is that its use of two boxes with molecule exchange directly yields the correct equilibrium point for two phases in coexistence. The main drawback is that, just as with the insertion method for GCMC, GEMC fails at high densities.<sup>8</sup>

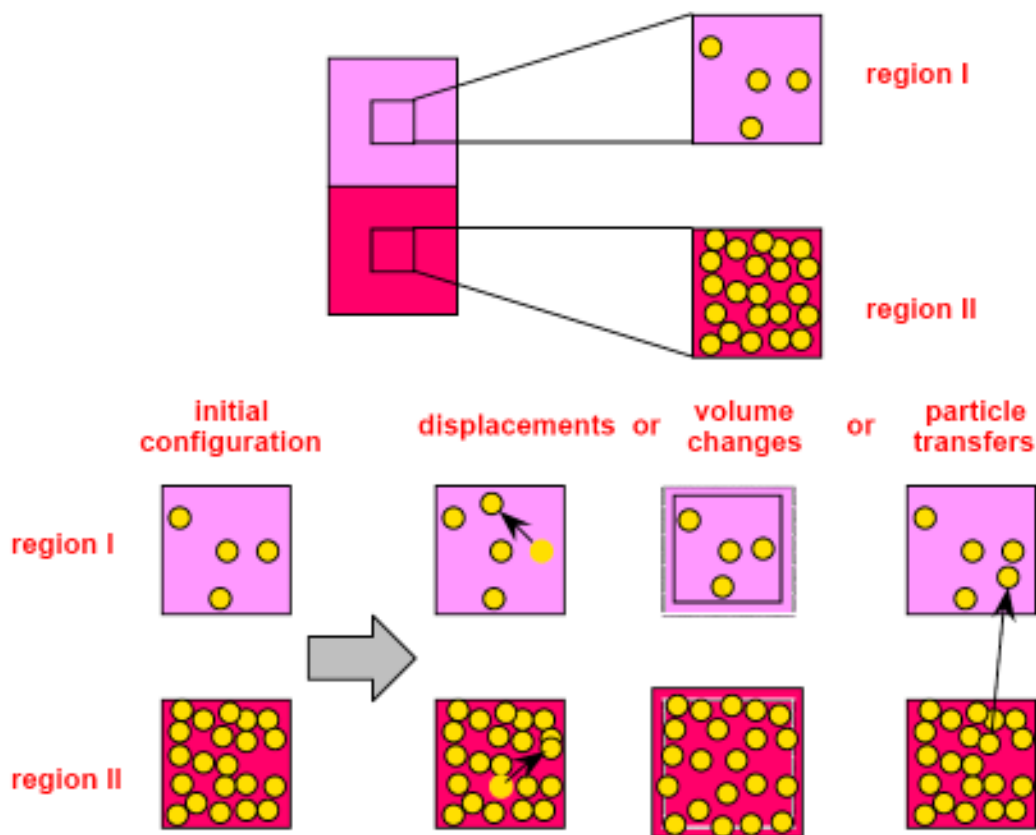


Figure 1.5. Schematic of GEMC [from reference 8]

### 1.3.3 Single Box Monte Carlo Simulations in NPT and NVT Ensembles.

In the previous section we explained how a Monte Carlo simulation with two boxes in NPT or NVT ensembles can be useful to study the phase equilibria of pure fluids

or binary mixtures. On the other hand, Monte Carlo simulations with a single box in these ensembles are also useful and were used in this study. The main use of a single box Monte Carlo simulation in the NPT ensemble is to evaluate a property of a fluid at a certain state point. In this study Monte Carlo simulations in the NPT ensemble were used to compute the chemical potential of a fluid certain pressure and temperature. The evaluated chemical potentials are used in GCMC simulations to obtain the isotherm of the fluid in an adsorbent over a range of pressure. The computation of chemical potential of a fluid in the NPT ensemble requires a technique called Widom's insertion method.<sup>9</sup> This method includes insertions of a test particle in to the simulation box equilibrated at the desired temperature and pressure with the Monte Carlo simulation in the NPT ensemble. The energy felt by the test particle during the insertion move is used to calculate the chemical potential of the fluid. This insertion move is different than the one mentioned in the GCMC simulations. Here the test particle is removed from the system after it is inserted and the energy felt by it is computed. For this reason some prefer to call the test particle as the ghost particle.

Single box Monte Carlo simulations in the NVT ensemble can be used to generate initial configuration for Monte Carlo and Molecular Dynamics simulations. In this study we used single box Monte Carlo simulations in the NVT ensemble to obtain the initial coordinates of cations and surface groups in zeolites which are going to be explained in detail in Chapters 2 and 3.

#### **1.4. Nanoporous Materials of Interest**

In this study we focused on four different types of zeolites; silicalite, mordenite, zeolite-beta, zeolite-Y, and activated carbon. These are nanoporous materials which have

found applications in areas of separation, catalysis and gas storage. Fundamentals and applications of these materials are beyond the scope of this work and readers are encouraged to look reference books for detailed information.<sup>10,11</sup> to get a better understanding of their porous structures we present pictures of the four zeolites from three different perspectives.

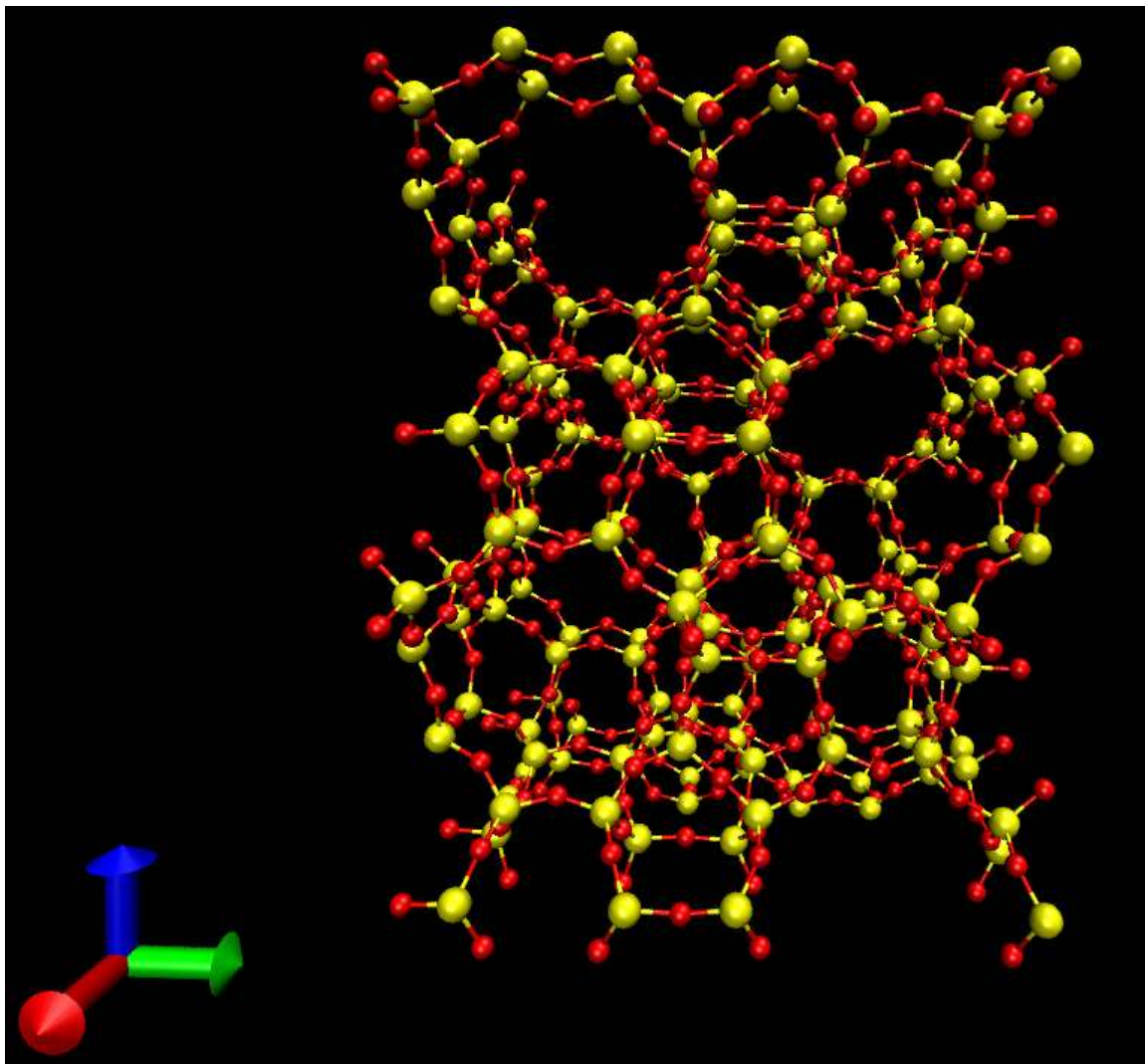


Figure 1.6. Silicalite. Y-Z plane

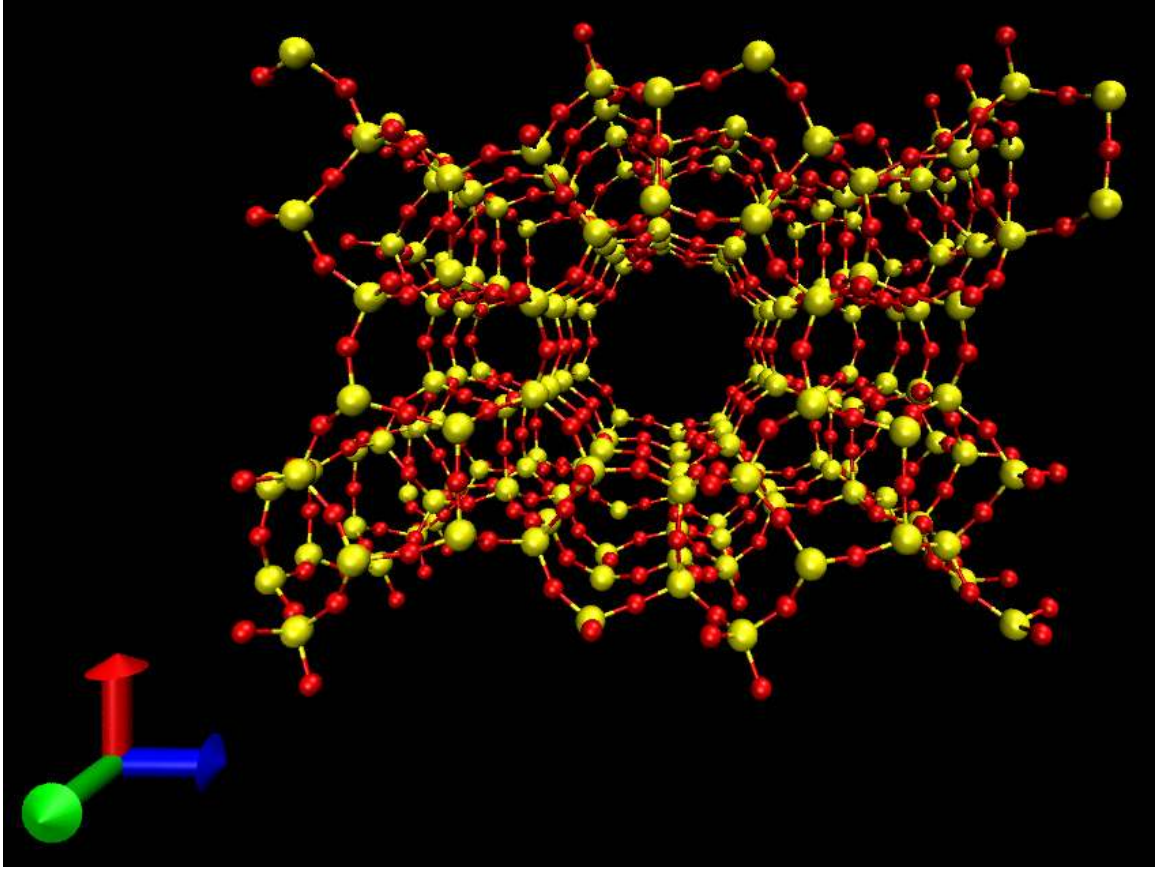


Figure 1.7. Silicalite. X-Z plane

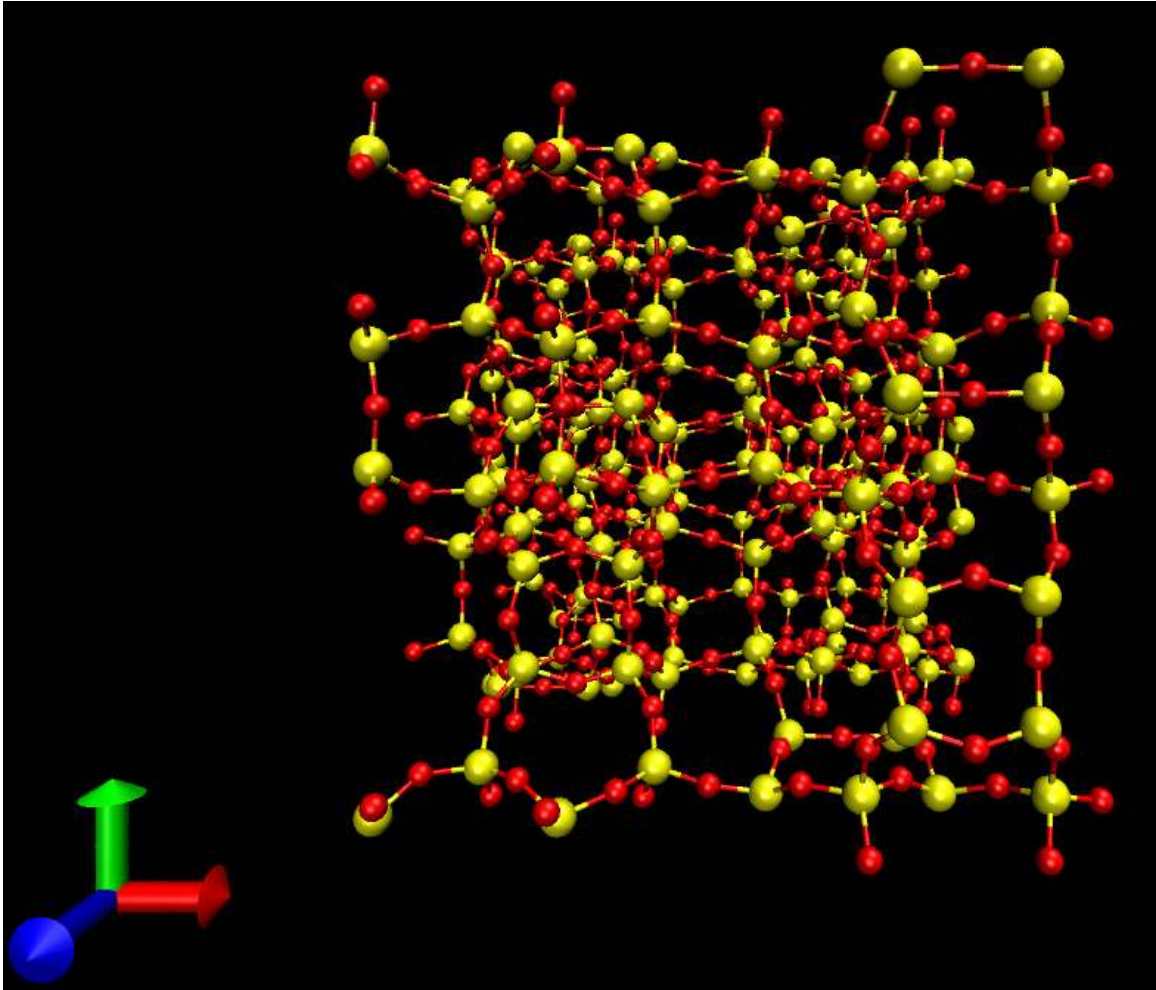


Figure 1.8. Silicalite. X-Y plane

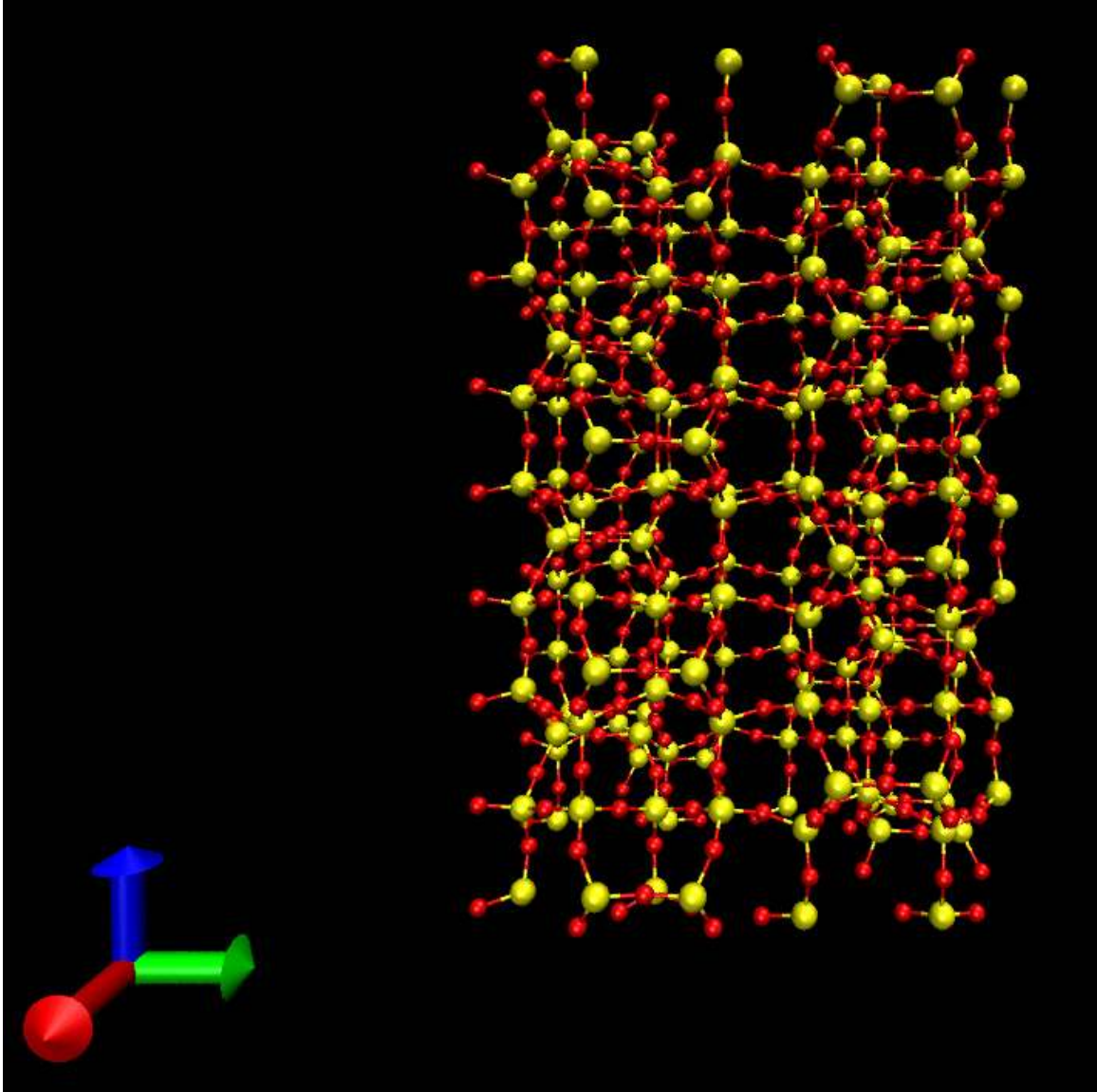


Figure 1.9. Mordenite. Y-Z plane

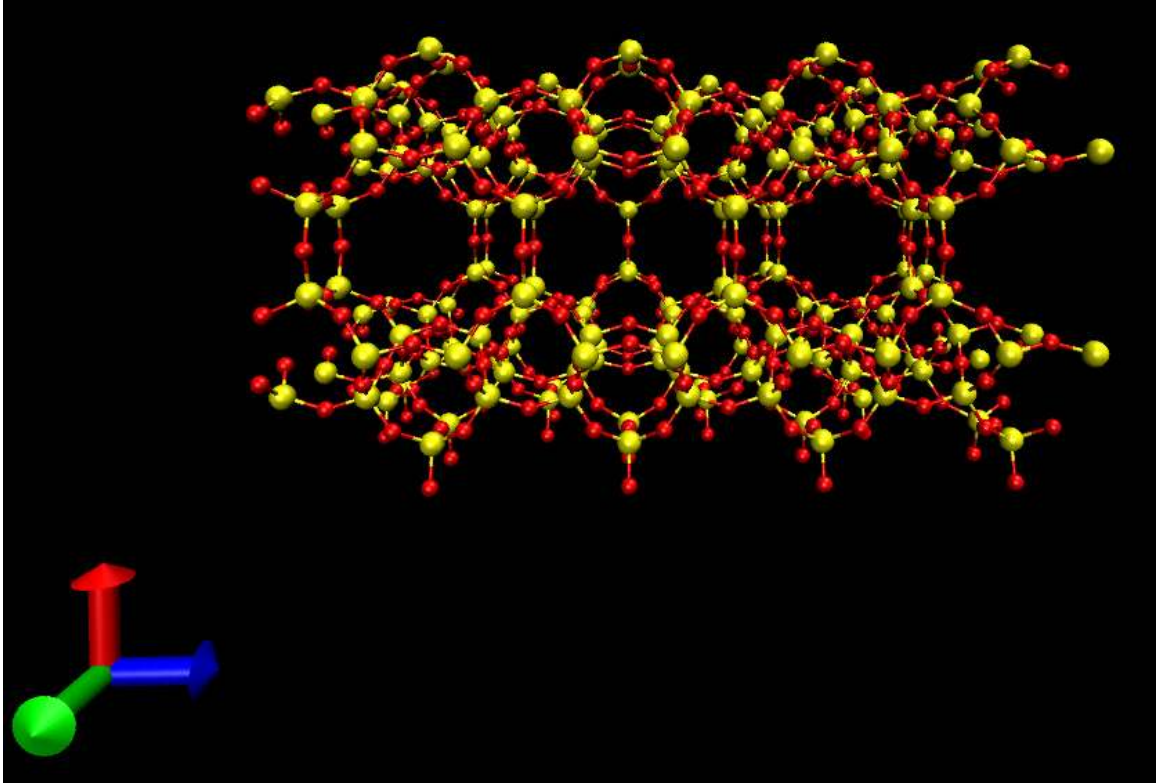


Figure 1.10. Mordenite. X-Z plane

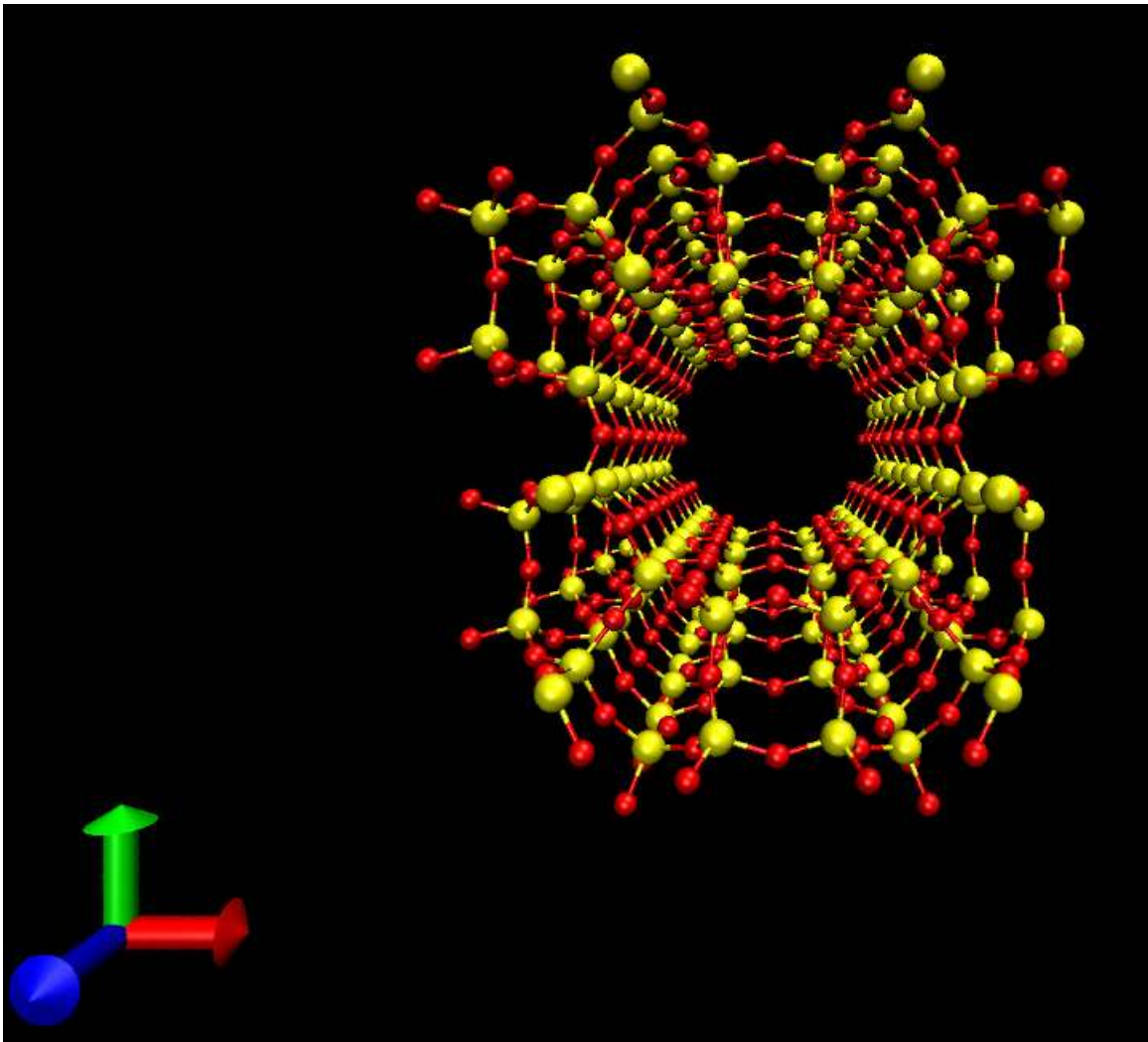


Figure 1.11. Mordenite. X-Y plane

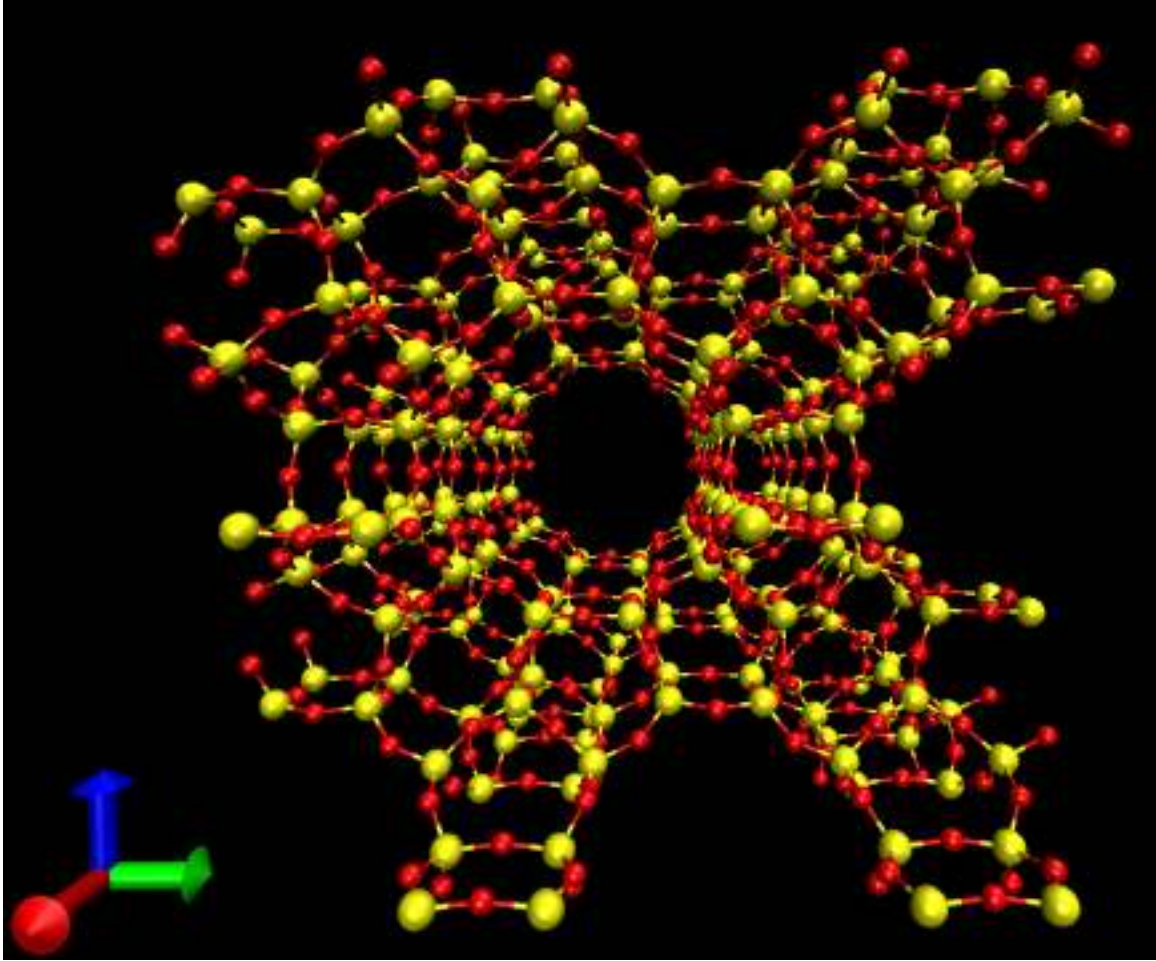


Figure 1.12. Zeolite-beta. Y-Z plane

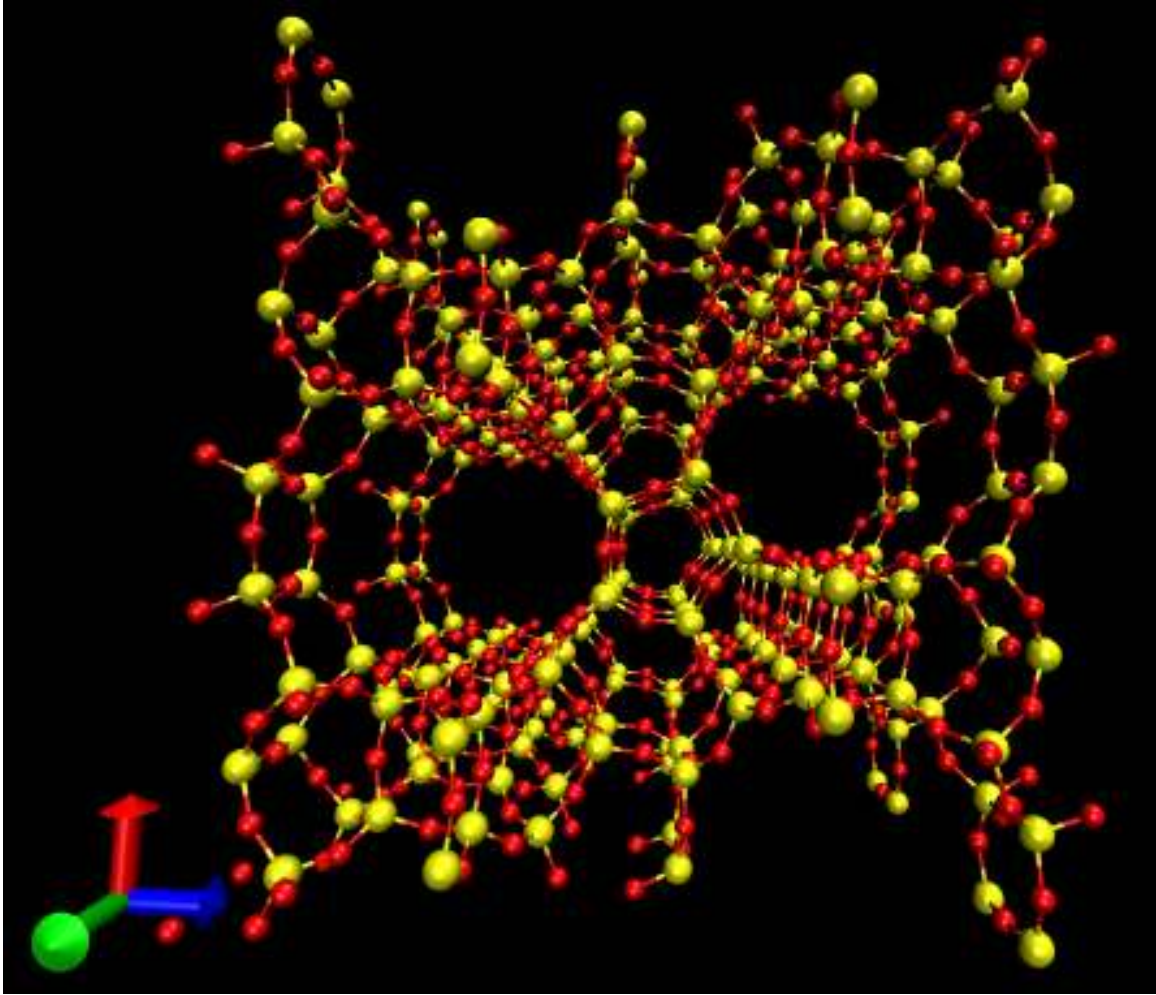


Figure 1.13. Zeolite-beta. X-Z plane

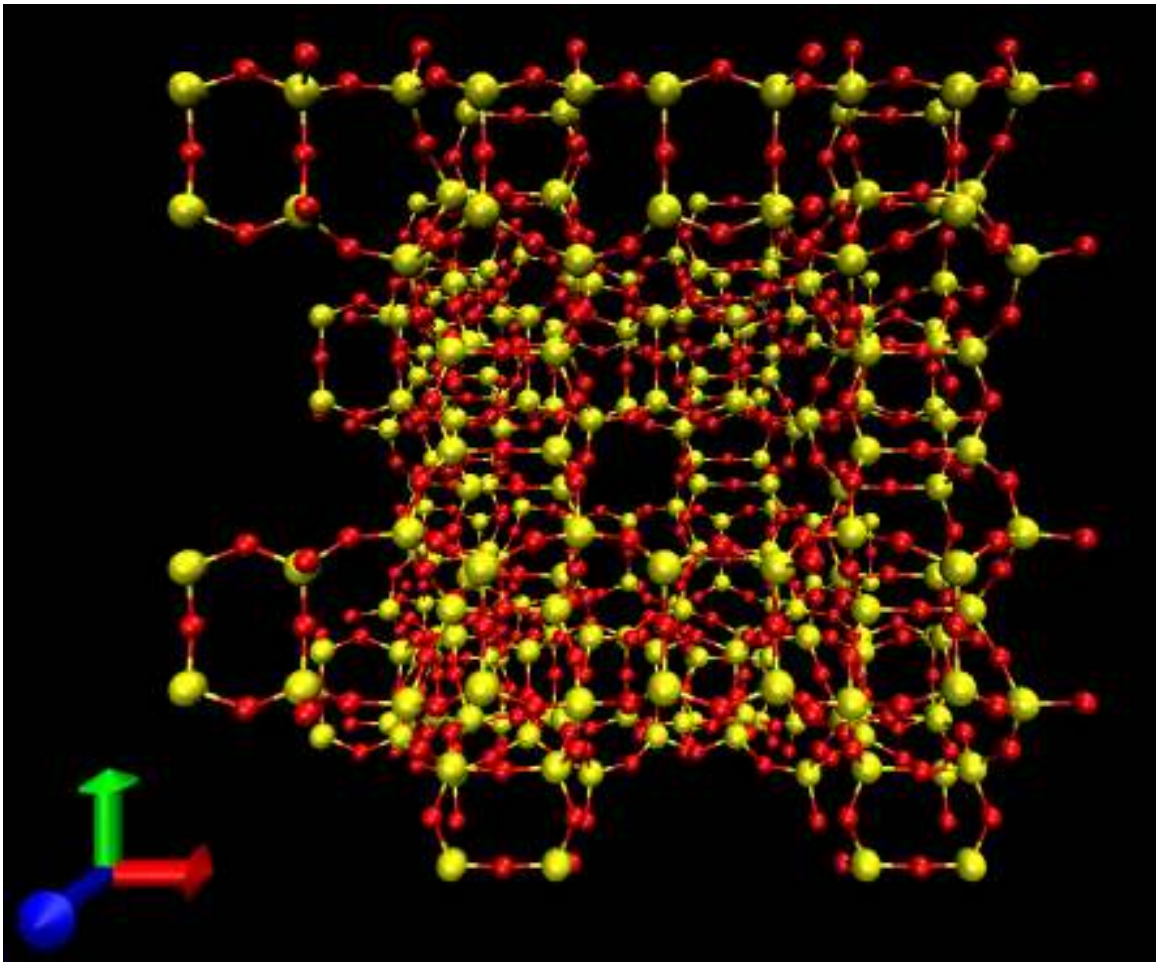


Figure 1.14. Zeolite-beta. X-Y plane

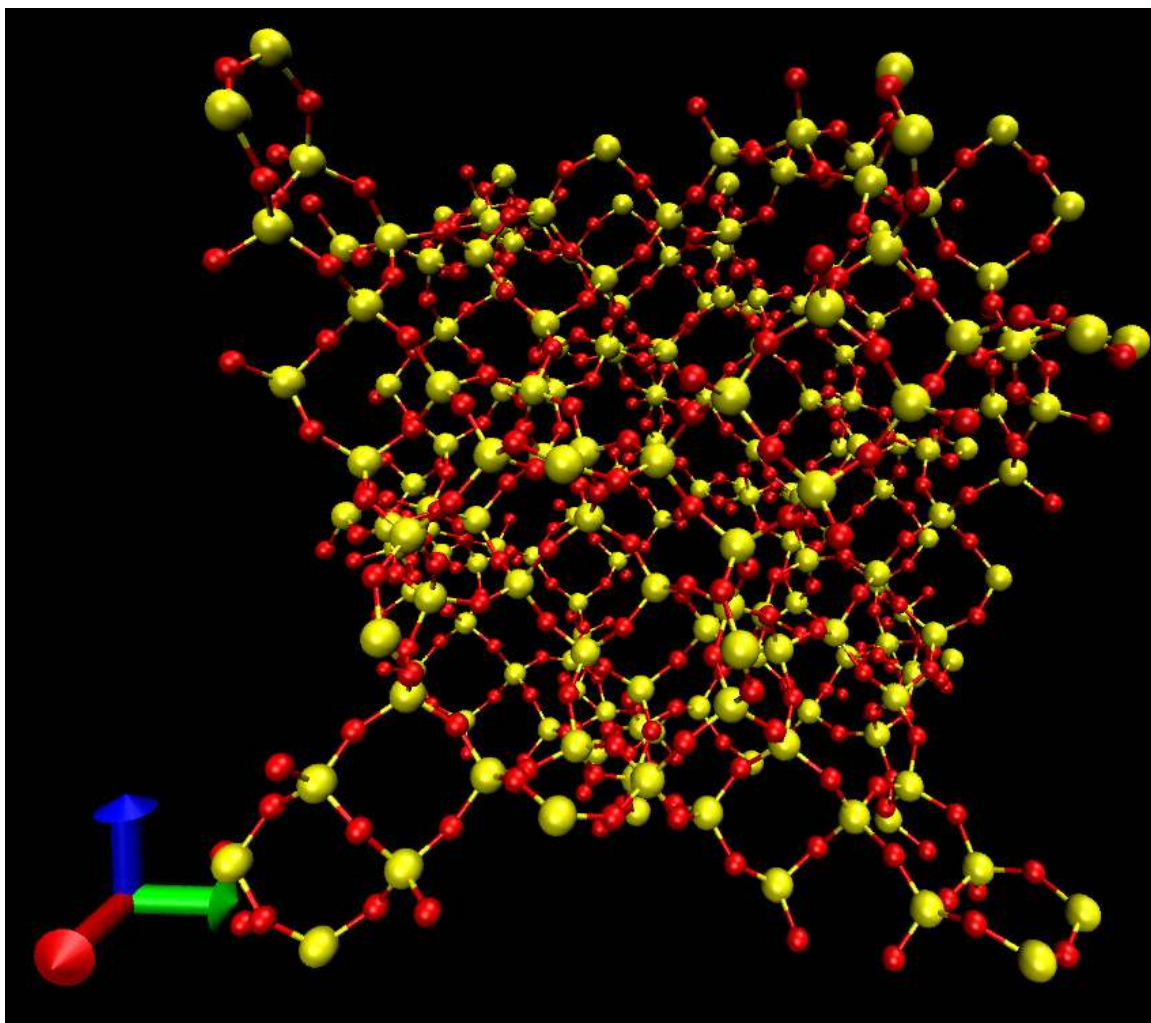


Figure 1.15. Zeolite-Y. Y-Z plane

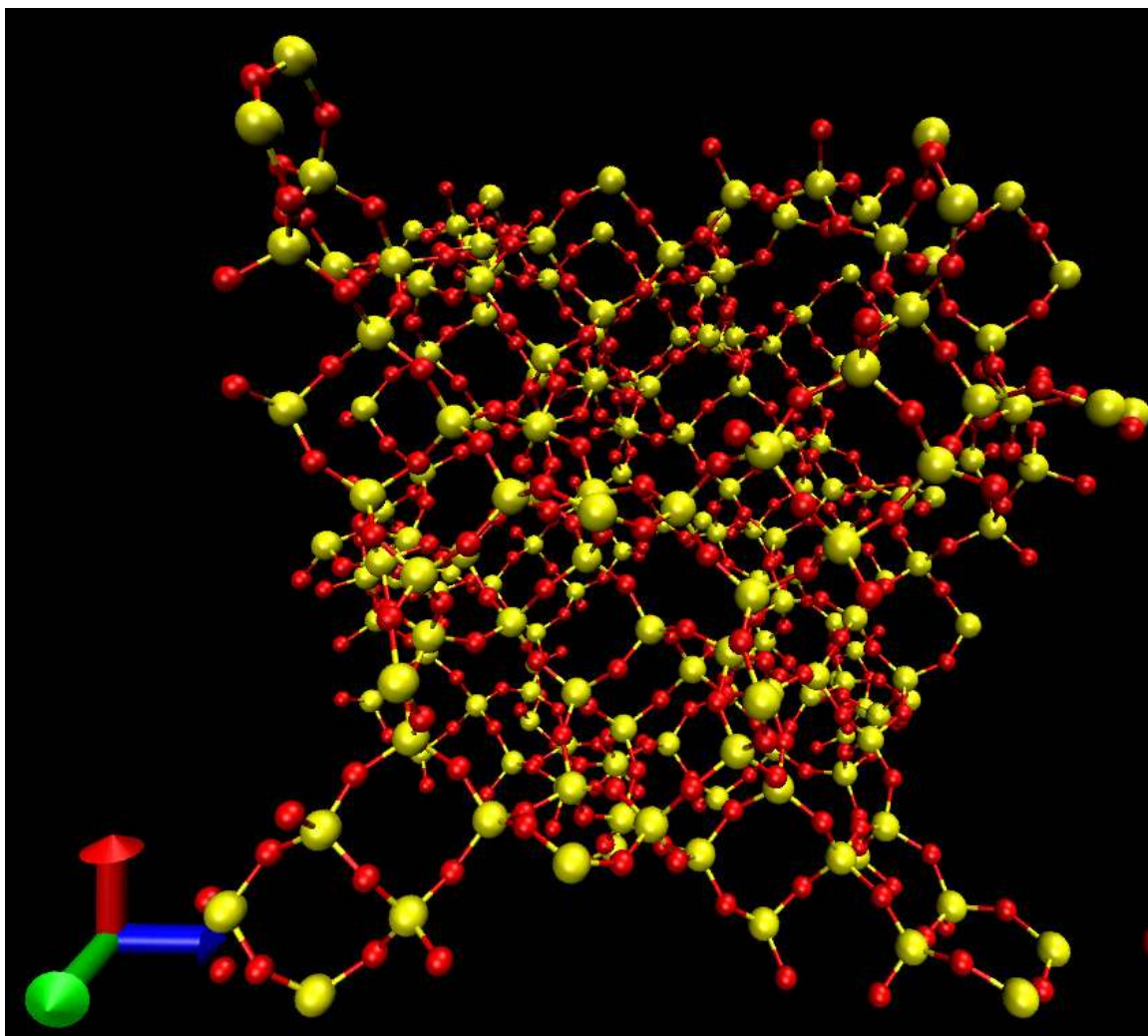


Figure 1.16. Zeolite-Y. X-Z plane

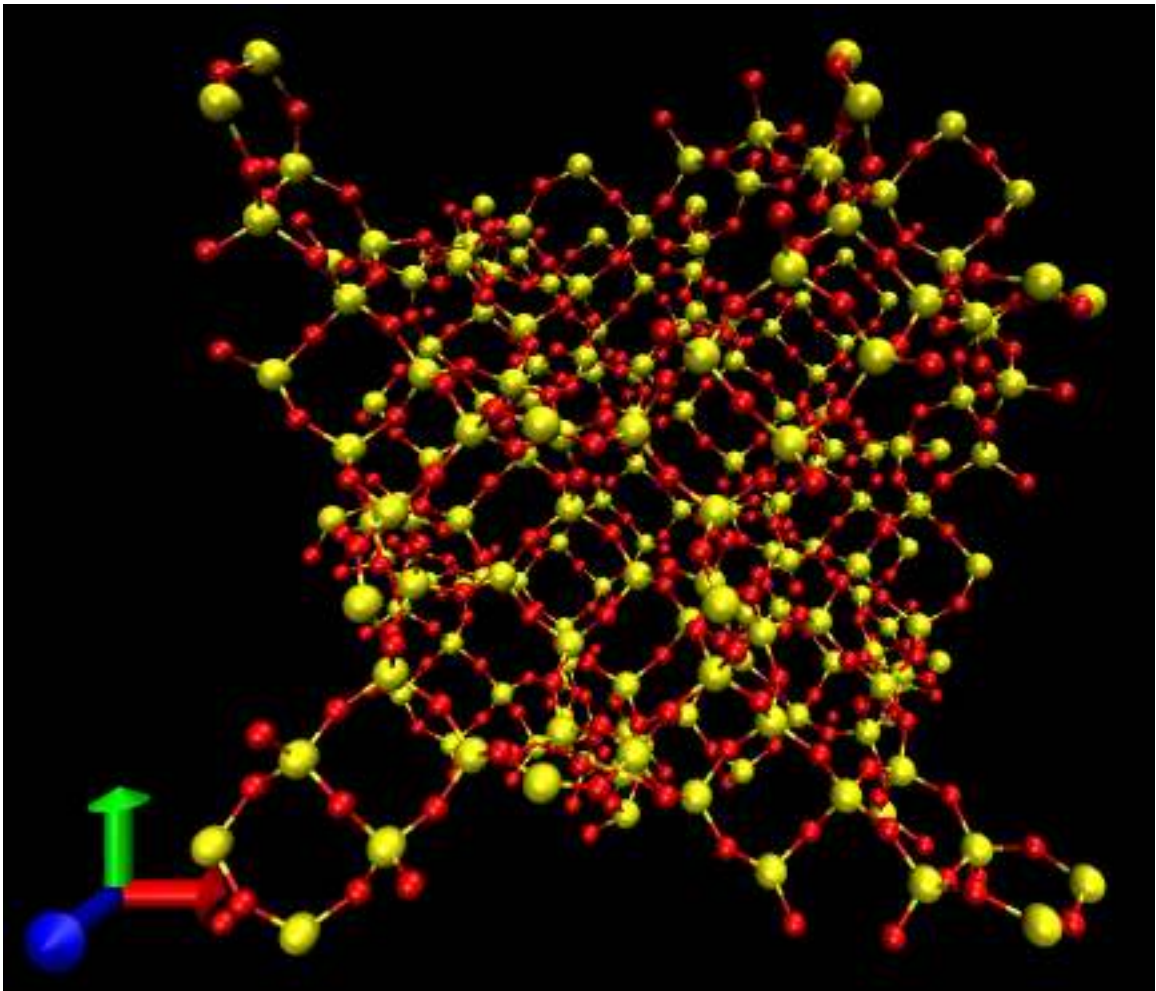


Figure 1.17. Zeolite-Y. X-Y plane

### **1.5. Objective**

The objective of this study is to utilize the tools of molecular simulation to investigate the adsorption of organics and water in different nanoporous materials. We aim to shed light on the factors affecting the adsorption process and reveal which adsorbent material is suitable for the adsorption of certain type of molecule. To achieve this goal, pure component and binary mixture adsorption isotherms, and affinities between the organic molecules and nanoporous materials will be computed. The structure of the fluids in the pores will be investigated. One challenge is the extremely low concentrations of the organics present in water which will test the limitations of the molecular simulation approach. It is our motivation that the information obtained from molecular simulations will reduce the exposure time of researchers to these contaminants in the laboratory.

## Bibliography

1. Leach, A., *Molecular Modelling: Principles and Applications*, 2nd Ed., 2001, Prentice Hall.
2. Ercolessi, F., *A Molecular Dynamics Primer*, <http://www.sissa.it/furio>
3. N. Metropolis; A.W. Rosenbluth; M.N. Rosenbluth; A.H. Teller; E. Teller; *J. Chem. Phys.* **1953**, 21, 1087.
4. Martin, M., *Monte Carlo Primer, Towhee User Manual*, <http://towhee.sourceforge.net>
5. Allen, M.P., and D.J. Tildesley. 1987. *Computer Simulation of Liquids*. Oxford: Oxford University Press
6. Panagiotopoulos, A.Z., *Molec. Phys.* **1987**, 62,701.
7. Panagiotopoulos, A.Z., *Molec. Phys.* **1987**, 61,813.
8. WTEC PANEL ON APPLICATIONS OF MOLECULAR AND MATERIALS MODELING, International Technology Research Institute, January 2002.
9. Widom, B., *J. Chem. Phys.* **1963**, 39, 2808.
10. Auerbach, S. M., Carrado, K. A., Dutta, P. K., Eds. *Handbook of Zeolite Science and Technology*; Marcel Dekker: New York, 2003.
11. Yang, R.T., *Adsorbents: Fundamentals and Applications*; John Wiley & Sons: Hoboken, New Jersey, 2003.

## **2. MOLECULAR SIMULATION of WATER ADSORPTION in SILICALITE: EFFECT of SILANOL GROUPS and DIFFERENT CATIONS.**

We report Grand Canonical Monte Carlo (GCMC) simulations of gas phase adsorption of water in silicalite to reveal the effects of defects in silicalite structure. Two types of defects were investigated; silanol nests, and  $H^+$ ,  $Li^+$ ,  $Na^+$ , and  $Cs^+$  cations which are associated with aluminum sites. The results indicate that hypothetical defect free silicalite is an extremely hydrophobic material and addition of even a single silanol nest causes a significant increase in the amount of water adsorbed. We also speculate that positions of silanol nests have an effect on the water adsorption. It was found that presence of all cations increased the water amount adsorbed in the order of  $Li^+ > Na^+ > Cs^+ > H^+$ .

### **2.1. Introduction**

Zeolites are microporous aluminosilicate materials traditionally used in catalysis and separation applications.<sup>1,2</sup> Silicalite is a pure silica MFI type of zeolite.<sup>3</sup> Silicalite is generally accepted as a hydrophobic material<sup>4</sup> and in several experimental studies silicalite was shown to preferentially adsorb organics from water.<sup>5-8</sup> This hydrophobicity is attributed to the  $\equiv Si-O-Si \equiv$  bonds, however, defects in the structure of silicalite allow certain amount of water to be adsorbed.<sup>9</sup> There are two common types of defects. First one is the extraframework cations, which count for non-neutrality of the silicalite framework due to presence of aluminum sites which substitute the missing silicon atoms.<sup>10</sup> The second type of defect is Si-OH group. During the synthesis of a zeolite, broken Si-O bonds are attacked by water molecules and Si-OH groups are formed instead of continuous Si-O-Si network. This may occur either on the surface of a zeolite where

Si-O-Si network is terminated and oxygen atom is can not be bonded to a Silicon atom or within the zeolite where a silicon atom is missing. In the latter case four Si-OH groups are formed per each missing silicon atom and this structure is called a silanol nest.<sup>11,12</sup> Hydrophobicity of silicalite has also led to a new application of using silicalite as a shock absorber, which is based on storage or dissipation of mechanical energy achieved by forced intrusion/extrusion of water into/from its hydrophobic pores at very high pressure.<sup>13</sup>

Although the behavior of water in silicalite is interesting, experimental and simulation studies of water adsorption in silicalite are not abundant in literature. While most of the experimental data regarding water adsorption in silicalite was obtained below saturation pressure<sup>5,14-18</sup>, there are a few studies which focused on the capillary filling effect observed at around very high pressure.<sup>13,19</sup> Molecular dynamics studies showed a low density structure for water molecules in silicalite with self diffusivity coefficients higher than its bulk value.<sup>20,21</sup> Grand Canonical Monte Carlo (GCMC) simulations were also made to obtain water adsorption isotherms over a broad range of pressure. These studies included simulations of siliceous silicalite<sup>22,23</sup> and the one with aluminum defect sites balanced with Na<sup>+</sup> cations.<sup>22</sup> To our knowledge in the only study which the effect of silanol nests on water adsorption in silicalite was investigated, water molecules with initially fixed positions were used to mimic silanol nests, while the siliceous silicalite was still present in the simulation.<sup>24</sup>

In this paper we investigated the adsorption of water in silicalite from the vapor phase and the effect of silanol nests and different cations using GCMC simulations. The results are presented in comparison with available experimental data and results from

simulations found in literature. The information and force field data presented in this paper is also important as they will be used in our future molecular simulation studies of adsorption of organics from water in silicalite.

## 2.2. Models and Methods

**2.2.1. Silicalite and Water Model.** Unitcell structure of orthorhombic (*Pnma*) silicalite was taken from the work of Artioli et al.<sup>25</sup> Two unit cells were used resulting in a simulation box with dimensions of  $a=20.0511 \text{ \AA}$ ,  $b=19.87570 \text{ \AA}$ ,  $c=26.73640 \text{ \AA}$ . Five different defects were considered. These were silanol nests and Aluminum sites with  $H^+$ ,  $Li^+$ ,  $Na^+$ ,  $Cs^+$  cations. In silicalite, there are several potential defect sites reported in literature, however, T12 site is the only one which all these reported. Therefore, T12 sites were used as the defect sites.<sup>26</sup> In the case of siliceous silicalite all the atoms were fixed. When we introduced a defect, the coordinates of the atoms of the defect sites were optimized and fixed before starting the GCMC adsorption. The water molecule was represented by the famous SPC-E water model<sup>27</sup> which is a rigid structure.

**2.2.2. Force Field.** The force field includes three types of interactions; silicalite-silicalite, silicalite-water and water-water. The first one is related to the optimization of coordinates of the defect sites. For the silanol groups and  $H^+$  we took the parameters from the class II force fields<sup>28,29</sup>. Parameters defining the interactions of  $Li^+$ ,  $Na^+$ ,  $Cs^+$  cations with silicalite were taken from the work of Beerdsen et.al.<sup>26</sup> Since this study is focused on the interaction of the water molecules with silicalite we will only list the parameters for silicalite-water and water-water interactions in Table 2.1.

For the silicalite-water and water-water interactions we used a pairwise-additive potential which is in the form of 12-6 Lennard-Jones (LJ) plus columbic potential to compute the site-site nonbonded interactions:

$$V_{ij} = 4\epsilon_{ij} \left[ \left( \frac{\sigma_{ij}}{r_{ij}} \right)^{12} - \left( \frac{\sigma_{ij}}{r_{ij}} \right)^6 \right] + \frac{q_i q_j}{4\epsilon_0 r_{ij}} \quad (1)$$

where  $i$  and  $j$  are atoms of water, silicalite lattice and defects, and  $r_{ij}$  is the distance between atoms  $i$  and  $j$ .  $\epsilon_{ij}$  and  $\sigma_{ij}$  are LJ well depth and diameter, respectively.  $q_i$  and  $q_j$  are the partial charges of the interacting sites.

**Table 2.1. Silicalite-Water Non-bonded Forcefield Parameters**

Lennard-Jones			Columbic	
Interacting Sites	$\sigma$ (Å)	$\epsilon$ (K)	Sites	q(e)
OZ <sub>1</sub> - OW	5.68	0.0265	Si	2.050
OZ <sub>2</sub> - OW	4.24	110.0	Al	1.75
OH - OW	3.1597	77.3679	Na <sup>+</sup> , Li <sup>+</sup> , Cs <sup>+</sup> , H <sup>+</sup>	1.0
HO - OW	4.065	4.837	<sup>a</sup> OZ <sub>Si-OZ-Si</sub> / OZ <sub>Si-</sub>	-1.025 / -1.200
Na <sup>+</sup> - OW	3.2469	10.4466	OZ-Al	-1.12
Cs <sup>+</sup> - OW	4.6108	1.7816	OH	0.6075
Li <sup>+</sup> - OW	2.5945	26.8249	HO	
H <sup>+</sup> - OW	1.7828	42.5453		

<sup>a</sup>OZ<sub>Si-OZ-Si</sub>: Oxygen of silicalite bridging two Si atoms, OZ<sub>Si-OZ-Al</sub>: Oxygen of silicalite bridging Si and Al atoms. OZ<sub>1</sub>: Oxygen of silicalite in the presence of silanol nests. OZ<sub>2</sub>: Oxygen of silicalite which includes the effect of silanol nests. OH: Oxygen of silanol. HO: Hydrogen of silanol.

The SPC-E model which governs the water-water interactions is a rigid water molecule with OW-HW bond is set to 1 Å and HW=OW-OW angle is set to 109.47°. The

LJ term is located on the oxygen atom ( $\sigma = 3.1656$ ,  $\epsilon = 78.1970$  K). Both oxygen and hydrogen atoms carry partial charges (OW = -0.8476, HW = 0.4238). On the other hand, force field parameters modeling the interaction of water molecules with the atoms of silicalite and defect sites were derived from several resources. As a common practice silicon atoms interacted with water molecules only through the columbic potential as they are well embedded in the framework having weak LJ interactions. The interaction of the oxygen atoms of silicalite and water molecule was investigated in two cases. In the first case oxygen atoms of the silicalite and the oxygen of the silanol groups were treated as different atoms and had different LJ parameters. In the second case oxygen atoms of the silicalite was parameterized such that it represented the effect of the silanol nests and explicit representation of silanol nests were not needed. This made our job easier to study the effects of cations on the water adsorption. LJ parameters of silanol groups and  $H^+$ , with water molecule were taken from a Molecular Dynamics (MD) study of quartz surfaces with water which used Charmm force field.<sup>30</sup> Water-Cation ( $Li^+$ ,  $Na^+$ ,  $Cs^+$ ) interactions were taken from a study where the parameterization was done by free energy perturbation simulations.<sup>31</sup>

Partial charges of silicon, oxygen, and aluminum atoms of silicalite were taken from the work of Jaramillo et.al.<sup>32</sup> All cations carried their ionic charge of +1 e (elementary charge).<sup>26</sup> Partial charges on the oxygen and hydrogen of the silanol group were calculated by scaling the regular silicalite oxygen atom charge and  $1/4^{th}$  of the silicon atom charge, respectively, according to the charges reported in the MD study of quartz surfaces with water.<sup>30</sup>

### **2.2.3. Chemical Potential of Water in the Gas Phase.**

The chemical potential of gas phase water was computed by Widom's insertion method<sup>33</sup> in a series of NPT Ensemble Monte Carlo<sup>34</sup> simulations. In this ensemble pressure, temperature and number of molecules are fixed. A simulation box containing 100 water molecules were setup at 298.15 K, which was the simulation temperature for all simulations in this paper, and chemical potential computed over a range of pressure between 0.1 kPa and 3.2 kPa. Translation and rotation moves of MTBE molecules and volume change move of the simulation box were sampled with probabilities 50%, 45% and 5%, respectively. At each pressure point the system were equilibrated for 10000 and a 10000 cycle production run followed the equilibration in which the chemical potential was measured by widom insertion method at every cycle. A cycle is equal to  $N$  Monte Carlo moves, where  $N$  is the number of molecules in the system. The statistical errors, which were computed by dividing the production run in to five blocks, for the measured chemical potentials were less than % 0.2 in all cases.

### **2.2.4. Optimization of Silicalite Structure with Defects.**

To make a silanol nest we deleted a silicon atom and placed four hydrogen atoms near to the four oxygen atoms which lost their bonds due to the deletion of a silicon atom. Up to four silanol nests per unit cell was constructed which is the maximum number of silanol nests reported.<sup>15</sup> In the case of a cation, a silicon atom was replaced by an aluminum atom and a cation was placed near the  $\text{TO}_4$  tetrahedra. We simulated two cations per unitcell which corresponds to a Si/Al ratio of 47. The final structures were obtained in 2-10 million step NVT ensemble Monte Carlo simulations by translating the defect atoms, while the positions of other atoms were kept fixed.

### **2.2.5. Simulation of the Adsorption Isotherms.**

Adsorption isotherms were computed in the Grand Canonical ( $\mu$ VT)<sup>34</sup> ensemble using Configurational Bias Monte Carlo (CB-GCMC)<sup>35-38</sup> simulations with MF-CPN<sup>39</sup> strategy. MF-CPN is a combined strategy for insertion and regrowth moves to increase their acceptance rates. Insertion/deletion, translation, rotation and regrowth moves were sampled with the probabilities of %30, %30, %30, %10. A cutoff distance of 9.5 Å was used with periodic boundary conditions applied in three dimensions. Columbic interactions were handled by the Ewald Sum method.<sup>40</sup> Each run lasted for 30 million steps in order to equilibrate the system, followed by 20 million steps for the data acquisition.

In all simulations Towhee Monte Carlo simulation code was used.<sup>41</sup>

## **2.3. Results and Discussion**

### **2.3.1. Effect of Silanol Nests.**

As stated in section 2.2.2 we investigated two cases. In the first case we modeled the silanol nests explicitly by using different LJ parameters and charges for oxygen atoms of silicalite and silanol nests. Since there is no real defect free silicalite it is impossible to find experimental data for siliceous silicalite. However, as the starting point we chose an earlier molecular simulation work by Fleys et.al.<sup>22</sup> where the adsorption of gas phase water was simulated in defect free silicalite. In Figure 2.1 adsorption isotherm obtained from GCMC simulations of Fleys et. al.<sup>22</sup> is compared from experimental adsorption isotherms of water. It can be clearly seen that simulation data underestimates the experimental data significantly, which was attributed to the lack of defects in the structure by the authors. Since COMPASS commercial force field was used in the study

of Fleys et. al.<sup>22</sup> force field parameters were not reported. Therefore, LJ parameters of silicalite oxygen were fitted to reproduce the results of Fleys et.al.<sup>22</sup>

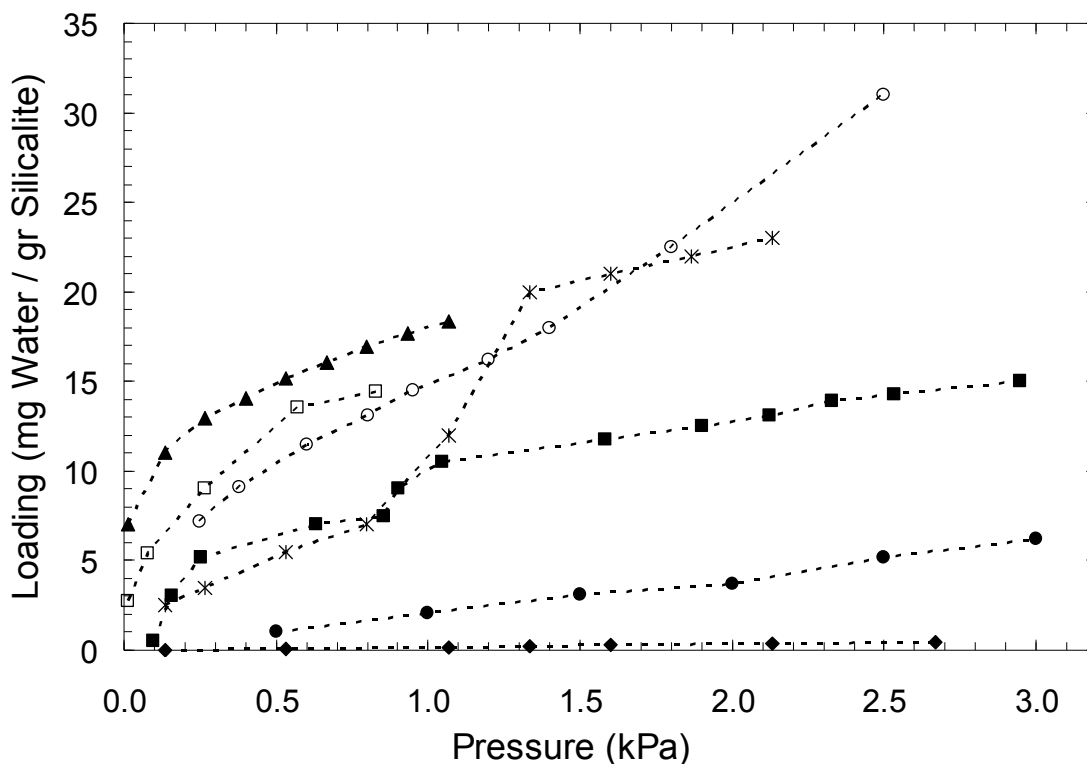


Figure 2.1. Gas phase water adsorption isotherms in silicalite: (◆) simulation<sup>22</sup> at 300 K, (□) experiment<sup>16</sup> at 303 K, (▲) experiment<sup>18</sup> at 303 K, (■) experiment<sup>16</sup> at 298.15 K, (○) experiment<sup>5</sup> at 298.15 K, (\*) experiment<sup>15</sup> at 298.15 K, (●) experiment<sup>17</sup> at 298.15 K.

In Figure 2.2 we report adsorption isotherms of water in silicalite obtained from our simulations with no silanol nest and up to 4 silanol nests per unit cell in comparison with the isotherm from the work of Fleys et.al.<sup>22</sup> It is quite interesting to see that even addition of a single silanol nest per unit cell boosts water adsorption significantly. On the

other hand, there is no linear increase in the adsorption amount with the addition of new silanol nests. Addition of the second silanol nest didn't make much of a difference. Contrary to this, when the third silanol nest is added a huge increase was observed, and surprisingly addition of the fourth silanol nest decreased the amount of water. While these results clearly show that silanol nests are strong points of attraction for water molecules, we can't establish a linear effect between them and we were unable to determine the reason for this, on the other hand, position of the silanol nests can be an important factor to affect the adsorbed water amount.

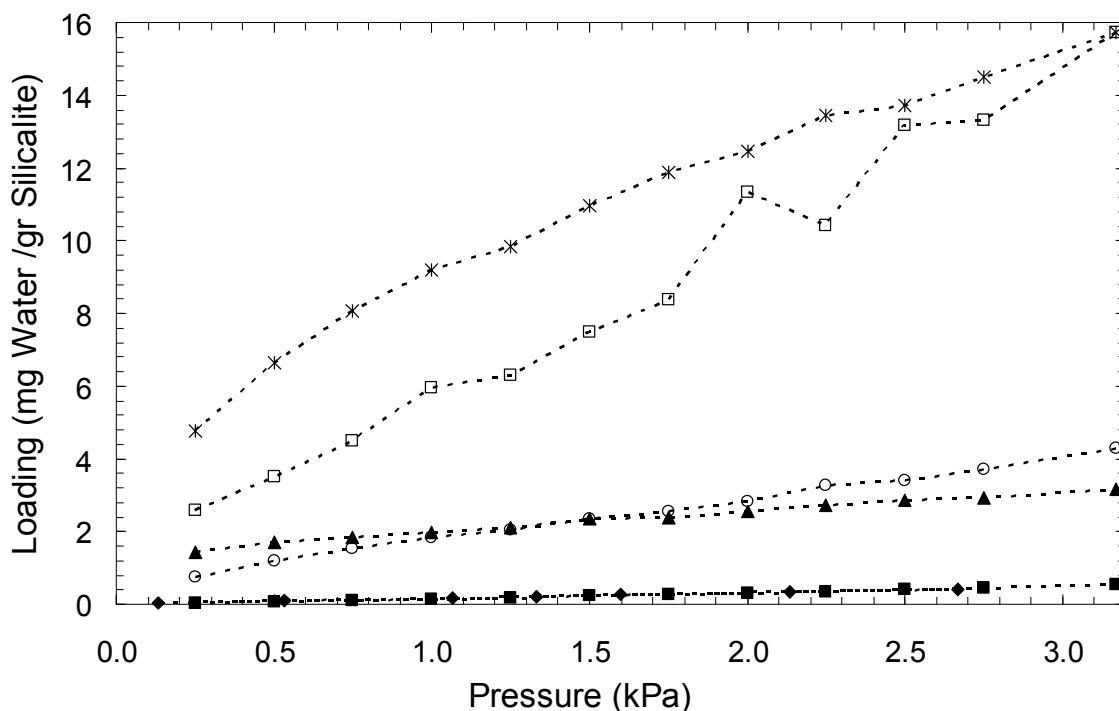


Figure 2.2. Gas phase water adsorption isotherms in silicalite: (◆) simulation<sup>22</sup> at 300 K - siliceous, (■) simulation<sup>this work</sup> at 298.15 K - siliceous, (▲) simulation<sup>this work</sup> at 298.15 K - 1 silanol nest per unit cell, (○) simulation<sup>this work</sup> at 298.15 K - 2 silanol nests per unit cell, (\*) simulation<sup>this work</sup> at 298.15 K - 3 silanol nests per unit cell, (□) simulation<sup>this work</sup> at 298.15 K - 4 silanol nests per unit cell.

Figure 2.3 shows the snapshot of a silanol nest. In Figure 2.4 we compared the adsorption isotherms of water in silicalite with 3 and 4 silanol nests per unit cell with the

experimental adsorption isotherms. It can be seen that with the addition of silanol nests a reasonable agreement was obtained with the experimental data. The agreement with experimental isotherm from Soulard et.al.'s <sup>14</sup> work is actually quite good. One should also note that although silicalite is not supposed to have any aluminum content, this is practically impossible and the presence of aluminum sites, even in very small amounts, will increase the amount of water adsorbed which partly explains the variation in the experimental data. It is also known that crystals size of the silicalite affects the amount of water adsorbed.<sup>15</sup>

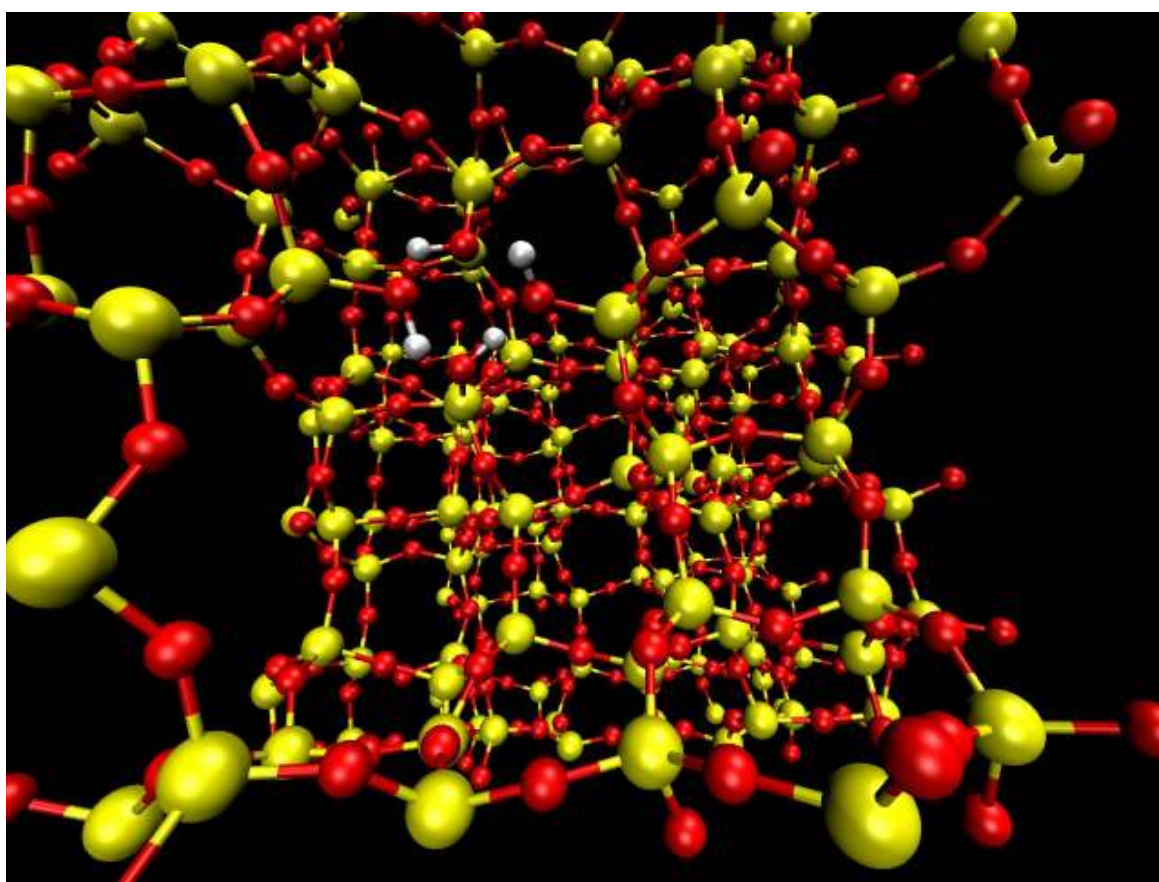


Figure 2.3. Snapshot of a silanol nest. (yellow) silicon atoms, (red) oxygen atoms, (white) hydrogen atoms.

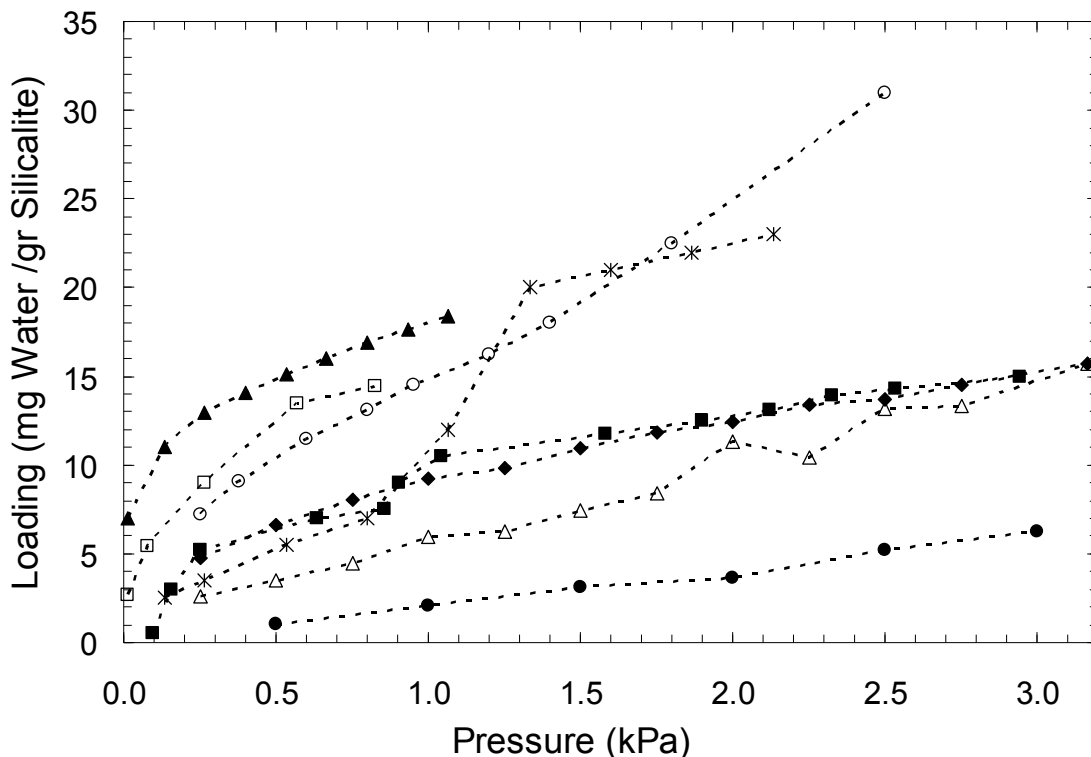


Figure 2.4. Gas phase water adsorption isotherms in silicalite: (◆) simulation <sup>this work</sup> at 298.15 K – 3 silanol nests per unit cell, (Δ) simulation <sup>this work</sup> at 298.15 K - 4 silanol nests per unit cell, (□) experiment<sup>16</sup> at 303 K, (▲) experiment<sup>18</sup> at 303 K, (■) experiment<sup>16</sup> at 298.15 K, (○) experiment<sup>5</sup> at 298.15 K, (\*) experiment<sup>15</sup> at 298.15 K, (●) experiment<sup>17</sup> at 298.15 K.

### 2.3.2. Effect of Cations.

After simulating the effects of silanol nests, we investigated the effects of cations on the adsorption of water in silicalite. In this second case silanol nests were not represented in the silicate structure, instead their effect on adsorption was represented by adjusting the LJ parameters of oxygen atom of the silicalite. This was achieved by fitting the oxygen parameters to reproduce the experimental adsorption isotherms. Obviously there is no solid agreement between the experimental data; therefore, we tried to fit an isotherm which will give an average representation of other experimental isotherms cited

here. In Figure 2.5 water adsorption isotherm obtained by the new LJ parameters of silicalite oxygen was compared with the experimental isotherms.

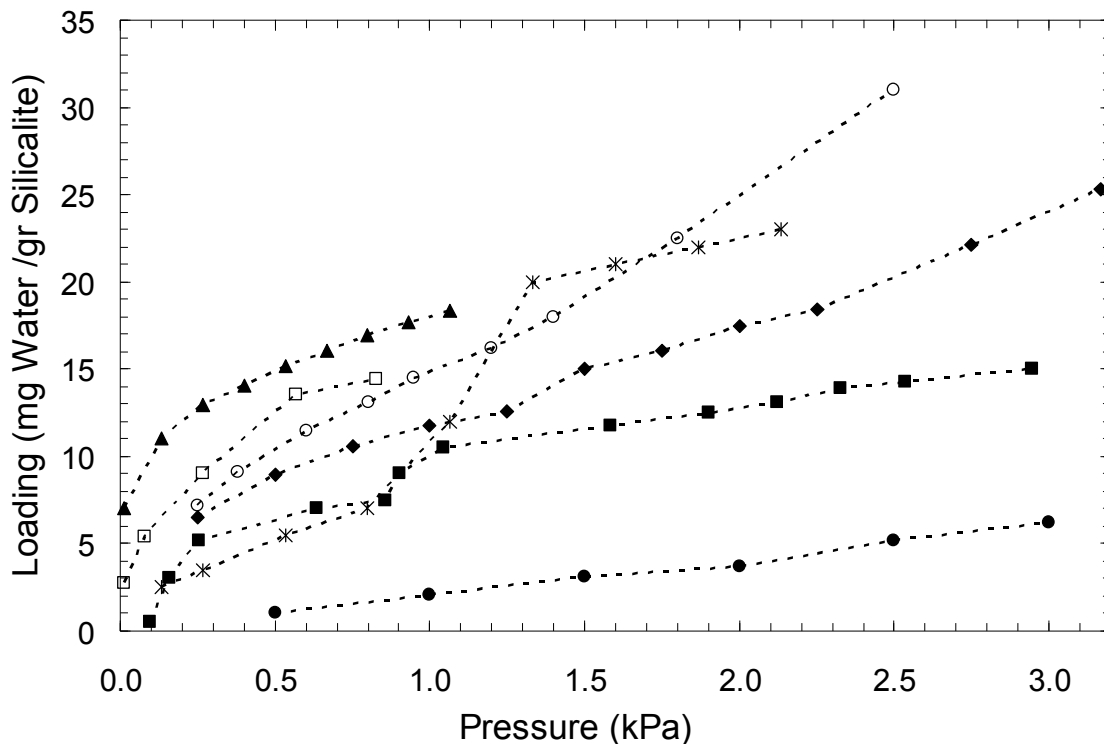


Figure 2.5. Gas phase water adsorption isotherms in silicalite: (◆) simulation <sup>this work</sup> at 298.15 K - siliceous, (□) experiment<sup>16</sup> at 303 K, (▲) experiment<sup>18</sup> at 303 K, (■) experiment<sup>16</sup> at 298.15 K, (○) experiment<sup>5</sup> at 298.15 K, (\*) experiment<sup>15</sup> at 298.15 K, (●) experiment<sup>17</sup> at 298.15 K.

In Figure 2.6 we present the water adsorption isotherms in silicalite with two cations per unit cell and with no cations which is siliceous. The amount of water adsorbed is in the order of  $\text{Li}^+ > \text{Na}^+ > \text{Cs}^+ > \text{H}^+$ . The first three cations are ordered in an increasing atomic radius, although the amount of water adsorbed in the presence of  $\text{Li}^+$  is only slightly more than it is in the presence of  $\text{Na}^+$ . On the other hand we did not observe the same trend for  $\text{H}^+$ . It should be noted that compared to other cations,  $\text{H}^+$  is located very close to the oxygen atoms of silicalite ( $r \approx 0.96\text{\AA}$ ) due to the formation of Bronsted acid sites. It appears that the model we used did not work successfully for  $\text{H}^+$  considering the

experimental findings that more amount of water is adsorbed in the presence of this cation compared to  $\text{Na}^+$  and  $\text{Cs}^+$  cations.<sup>15,42</sup>

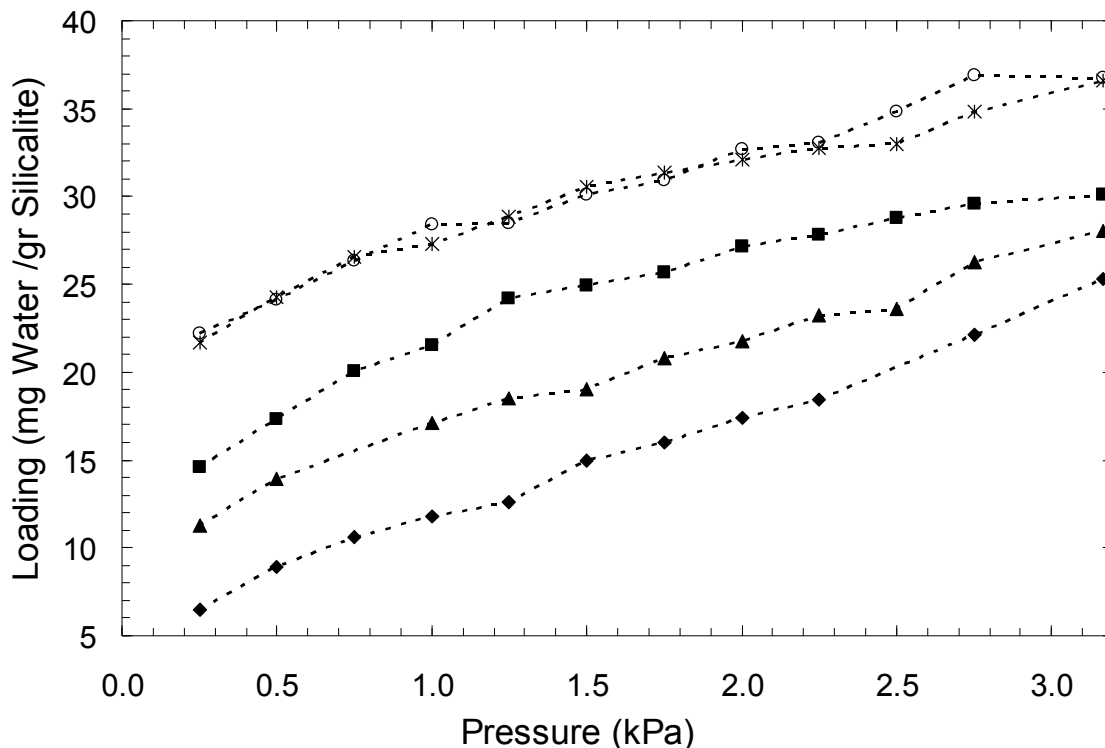


Figure 2.6. Gas phase water adsorption isotherms in silicalite: (◆) simulation<sup>this work</sup> at 298.15 K - siliceous, (■) simulation<sup>this work</sup> at 298.15 K - 2  $\text{Cs}^+$  per unit cell, (▲) simulation<sup>this work</sup> at 298.15 K - 2  $\text{H}^+$  per unit cell, (○) simulation<sup>this work</sup> at 298.15 K - 2  $\text{Li}^+$  per unit cell, (\*) simulation<sup>this work</sup> at 298.15 K - 2  $\text{Na}^+$  per unit cell.

#### 2.4. Conclusions

Adsorption of water in silicalite has become an interesting area of investigation due to potential applications of silicalite as an adsorbent to remove organics from water and as shock absorbers, both thanks to silicalite's hydrophobicity. We investigated the effects of defects. Silanol nests were found to have a big impact on the hydrophobicity of silicalite, triggering significant amount of water adsorption even with one silanol nest per unit cell. We also investigated the effect of four different cations,  $\text{H}^+$ ,  $\text{Li}^+$ ,  $\text{Na}^+$ , and  $\text{Cs}^+$ . All of their presence in silicalite increased the amount of water adsorbed. While  $\text{Li}^+$ ,  $\text{Na}^+$ , and  $\text{Cs}^+$  cations promoted water adsorption inversely related to their atomic radius,  $\text{H}^+$

did not obey this trend which we attribute to the quality of the force field or inability of LJ terms to model this phenomenon.

## Bibliography

1. Auerbach, S. M., Carrado, K. A., Dutta, P. K., Eds. Handbook of Zeolite Science and Technology; Marcel Dekker: New York, 2003.
2. Crystalline and organized porous solids (thematic issue). Patarin, J., Gies, H., Eds. *C. R. Chim.* **2005**, 8, 3-4.
3. Meier, W. M.; Olson, D. H.; Baerlocher, Ch. Atlas of zeolite structure types; Elsevier: New York, 1996.
4. Flanigen, E. M.; Bennett, J. M.; Grose, R. W.; Cohen, J. P.; Patton, R. L.; Kirchner, R. M.; Smith, J. V. *Nature* **1978**, 271, 512.
5. Arjan, G.; Thompson, R.W., *Microporous Mesoporous Mater.* **2002**, 55, 265-274.
6. Erdem-Senatalar, A.; Bergendahl, J.A.; Giaya, A.; Thompson, R.W.; *Environ. Eng. Sci.* **2004**, 21, 722.
7. Anderson, M.A.; *Environ. Sci. Technol.* **2000**, 34, 725.
8. Bowen, T.C.; Vane, L.M., *Langmuir* **2006**, 22, 3721.
9. Chen, N.Y., *J. Phys. Chem.* **1976**, 80, 60.
10. Sano, T.; Hasegawa, M.; Kawakami, Y.; Yanagishita, H. *J. Membr. Sci.* **1995**, 107, 193.
11. Fricke, R. ; Kosslick, H.; Lischke, G.; Richter, M., *Chem. Rev.* **2000**, 100, 2303.

12. Zecchina, A.; Bordiga, S.; Spoto, G.; Scarano, D.; Petrini, G.; Leofanti, G., Padovan, M., Arean, C.O., *J. Chem. Soc. Faraday Trans.* **1992**, 88, 2959.
13. Eroshenko, V.; Regis, R.C.; Soulard, M., Patarin, J., *J. Am. Chem. Soc.* **2001**, 123, 8129.
14. Soulard, M.; Patarin, J.; Eroshenko, V.; Regis, R.-C. In Proceedings of the 14th International Zeolite Conference, Cape Town; Van Steen, E., et al., Eds.; **2004**, 1830-1837.
15. Olson, D. H.; Haag, W. O.; Borghard, W. S. *Microporous Mesoporous Mater.* **2000**, 35-36, 435.
16. Bolis, V.; Busco, C.; Ugliengo, P., *J. Phys. Chem. B* **2006**, 110, 14849.
17. Oumi, Y.; Miyajima, A.; Miyamoto, J.; Sano, T. *Stud. Surf. Sci. Catal.* **2002**, 142, 1595.
18. Kuznetsov, B. V.; Rakhmanova, T. A. *Russ. J. Phys. Chem.* **2001**, 75, 933-938.
19. Desbiens, N.; Demachy, I.; Fuchs, A. H.; Kirsch-Rodeschini, H.; Soulard, M.; Patarin, J. *Angew. Chem., Int. Ed.* **2005**, 44, 5310-5313.
20. Fleys, M.; Thompson, R.W., *J. Phys. Chem. B* **2004**, 108, 12197.
21. Demontis, P.; Stara, G.; Suffritti, G.B., *J. Phys. Chem. B* **2003**, 107, 4426.
22. Fleys, M.; Thompson, R.W., *J. Chem. Theory Comput.* **2005**, 1, 453.
23. Desbiens, N.; Boutin, A.; Demachy, I., **2005**, 109, 24071.

24. Artioli, G.; Lamberti, C.; Marra, G.L.; *Acta. Cryst. B* **2000**, 56, 2.
25. Knappe, D.R.U.; Campos, A.A.R.; *Water Sci. and Tech. : Water Supply* **2005**, 5, 83.
26. Beerdsen, E.; Dubbeldam, D.; Smit, B.; Vlugt, T.J.H.; Calero, S.; *J. Phys. Chem. B* **2003**, 107, 12088.
27. Berendsen, H.J.C.; Grigera, J.R.; Straatsma, T.P.; *J. Phys. Chem.* **1987**, 91, 6269.
28. Sun, H.; Rigby, D., *Spectrochimica Acta Prt A* **1997**, 53, 1301.
29. Hill, J.R.; Sauer, J., *J. Phys. Chem.* **1995**, 99, 9536.
30. Lopes, P.E.M.; Murashov, V.; Tazi, M.; Demchuk, E.; MacKerell Jr., A.D., *J. Phys. Chem. B* **2006**, 110, 2782.
31. Aqvist, J., *J. Phys. Chem.* **1990**, 94, 8021.
32. Jaramillo, E.; Grey, C. P.; Auerbach, S. M. *J. Phys. Chem. B* **2001**, 105, 12319.
33. Widom, B., *J. Chem. Phys.* **1963**, 39, 2808.
34. Frenkel, D.; Smit, B., *Understanding Molecular Simulation from Algorithms to Applications*; 2<sup>nd</sup> ed., Academic Press: SanDiego, **2002**.
35. Siepmann, J.I., *Mol. Phys.* **1990**, 70, 1145.
36. Siepmann, J.I.; Frenkel, D., *Mol. Phys.* **1992**, 75, 59.
37. Frenkel, D.; Mooji, G.C.A.M.; Smit, B., *J. Phys.: Condens. Matter*, **1992**, 3053.

38. Laso, M.; de Pablo, J.J.; Suter, U.W., J. Chem. Phys. **1992**, 97, 2817.
39. Martin, M.G.; Frischknecht, A.L., Mol. Phys. **2006**, 104, 2439.
40. Ewald, P.P., Ann. Phys. **1921**, 64, 253.
41. <http://towhee.sourceforge.net>
42. Hunger, B.; Heuchel, M.; Matysik, S.; Beck, K.; Einicke, W.D., Thermochemica Acta **1995**, 269-270, 599.

### **3. MOLECULAR SIMULATION of THE ADSORPTION of MTBE in SILICALITE, MORDENITE, and ZEOLITE BETA**

The use of methyl tertiary butyl ether (MTBE) as a gasoline additive has resulted in serious environmental problems following spills and leaks, primarily due to MTBE's high solubility in water. Remediation technologies have involved air stripping, advanced oxidation, and sorption on granular activated carbons (GAC). Hydrophobic zeolites, such as silicalite, dealuminated Y, mordenite, and beta, have been of interest in recent studies for the removal of MTBE from water. Some of these materials have shown better performance than GAC particularly in the  $\mu\text{g/L}$  range. We made Monte Carlo and Molecular Dynamics simulations of the adsorption of pure MTBE in silicalite, mordenite, and zeolite beta with different  $\text{Na}^+$  loadings at room temperature to reveal the factors affecting the adsorption process. The results show that although the three zeolites studied here have similar pore volumes, the pore structure of zeolite beta causes a significant difference on the predicted amount of MTBE adsorbed. It was found that the position of the  $\text{Na}^+$  cations has an important effect at lower pressures. Within the range of  $[\text{Na}^+]$  studied, the amount of  $\text{Na}^+$  was not found to be critical on the adsorption capacity of any of the zeolites studied, except at very low pressures in silicalite and zeolite beta.

#### **3.1. Introduction**

Methyl tertiary butyl ether (MTBE) has been used as a fuel additive at low levels since 1979 to increase the oxygenate content of the gasoline which reduces harmful tailpipe emissions. Starting in the early 1990s MTBE concentrations reached up to 15% in motor gasoline by volume.<sup>1</sup> Although it is being used as an agent to control air pollution, inevitable releases of MTBE into the environment have caused contamination

of drinking water resources. There is evidence that MTBE is a possible human carcinogen,<sup>2</sup> and it also spoils the taste and imparts a foul odor in drinking water. These consequences led EPA to issue an advisory on MTBE for drinking water, and set the concentration limit to 20 µg/L for odor and 40 µg/L for taste concerns.<sup>3</sup>

MTBE's high aqueous solubility, low Henry's law constant, small molecular size and its relative resistance to biodegradation makes it a persistent and highly mobile contaminant in the environment.<sup>4</sup> Another problem caused by its high aqueous solubility and low volatility is the relatively difficult of removal of MTBE from water with treatment processes such as air stripping and activated carbon adsorption. Additionally, undesirable metabolites, tertiary-butyl alcohol (TBA) or bromate, are the byproducts of biodegradation and chemical oxidation of MTBE.<sup>5-8</sup> An overview of the physical and chemical characteristics of MTBE and its use and production numbers are given in literature.<sup>9-15</sup>

In the past few years there have been many studies on the adsorption of MTBE from water in different zeolites as alternative adsorbents to activated carbon.<sup>16-19</sup> Erdem-Şenatar et al.<sup>16</sup> performed experiments with silicalite, mordenite, zeolite beta and zeolite Y with high Si/Al ratios. They reported their results in comparison with MTBE adsorption from water in Centaur<sup>®</sup> Activated Carbon from Calgon Corporation and showed that zeolites with small channel diameters, silicalite and mordenite, outperformed activated carbon at very low concentrations. Knappe et al.<sup>17</sup> studied the same type of zeolites studied by Erdem-Şenatar et al. with different types and loadings of cations, H<sup>+</sup>, Na<sup>+</sup>, NH<sub>4</sub><sup>+</sup> and compared their results with results of MTBE adsorption in different types of activated carbons. They came to a similar conclusion on the effectiveness of the

adsorption of MTBE from water in silicalite and mordenite. In both studies especially silicalite showed outstanding performance compared to the activated carbon adsorbents. Anderson<sup>18</sup> reported MTBE adsorption from water in high-silica mordenite, silicalite, and zeolite Y in comparison to Barneby-Cheney and Fischer activated carbons. Both mordenite and silicalite showed higher adsorption capacities than activated carbons, however, Anderson concluded that mordenite performed better than silicalite. Li et al.<sup>19</sup> experimented with three different types of zeolite beta, notably H<sup>+</sup>-beta, dealuminated beta, and all-silica beta. They compared their results with the performance of mordenite reported by Anderson and concluded that all-silica zeolite beta performed better.

In this study we present the results of Monte Carlo and molecular dynamics simulations of pure MTBE adsorption in silicalite, mordenite, and zeolite beta with different loadings of Na<sup>+</sup> cations.

### 3.2. Theoretical Models and Calculations

We used a pairwise-additive potential which is in the form of 12-6 Lennard-Jones (LJ) plus columbic potential to compute the site-site nonbonded interactions:

$$V_{ij} = 4\varepsilon_{ij} \left[ \left( \frac{\sigma_{ij}}{r_{ij}} \right)^{12} - \left( \frac{\sigma_{ij}}{r_{ij}} \right)^6 \right] + \frac{q_i q_j}{4\varepsilon_0 r_{ij}} \quad (1)$$

where  $i$  and  $j$  are atoms of MTBE or zeolite lattice, and  $r_{ij}$  is the distance between atoms  $i$  and  $j$ .  $\varepsilon_{ij}$  and  $\sigma_{ij}$  are LJ well-depth and diameter, respectively.  $q_i$  and  $q_j$  are the partial charges of the interacting sites.

Modeling the interacting sites was divided into three groups; MTBE-MTBE, Zeolite-Zeolite and Zeolite-MTBE. The first two were taken from the literature and the last was derived using the Lorentz-Berthelot mixing rules.<sup>39</sup>

$$\varepsilon_{ij} = \sqrt{\varepsilon_{ii}\varepsilon_{jj}} \quad \sigma_{ij} = \frac{\sigma_{ii} + \sigma_{jj}}{2} \quad (2)$$

MTBE interactions were modeled using the Trappe-UA forcefield<sup>20-23</sup> in which the methyl sites were represented by a united atom, bonds were kept rigid, and angle bending and torsion terms were treated as flexible. MTBE modeled with the Trappe-UA forcefield showed very good agreement with the experimental vapor liquid equilibrium and critical point data.<sup>23</sup> This was an important criterion for the selection of the Trappe-UA parameters, since fluids may undergo a phase transition when they are confined in nanoporous materials.<sup>24</sup> Interaction of the zeolite framework atoms and out of framework Na<sup>+</sup> cations was modeled using the parameters of Jaramillo et al.<sup>25</sup> and Auerbach et al.<sup>48</sup>.

We will only list Zeolite-MTBE interaction parameters here; for MTBE-MTBE, Zeolite-Zeolite interaction parameters and how they were derived reader should consult,<sup>20-23,25,48</sup> respectively.

Zeolite-MTBE interactions were derived from the works of Beerdsen et al.<sup>26</sup> and Dubbeldam et al.<sup>27</sup> where adsorption of hydrocarbons in silicalite was studied. The results produced with their parameters gave excellent agreement with the experimental data of hydrocarbon adsorption of zeolites. Interaction parameters between the methyl united atoms and the carbon atom of MTBE and oxygen atoms of zeolite were already reported in these references. We used the Lorentz-Berthelot rules to compute the interaction parameters between the oxygen of MTBE and oxygen of zeolite framework. For Na<sup>+</sup>, LJ parameters were only available for its interaction with the methyl united atoms of MTBE. Again, Lorentz-Berthelot rules were used to derive Na<sup>+</sup>-Carbon of MTBE and Na<sup>+</sup>-Oxygen of MTBE parameters. Silicon and aluminum atoms interact with other atoms only through the columbic potential. Table 3.1 lists all the zeolite-MTBE interaction

parameters. For other forcefield parameters see Appendix 1. Unit cell structures of silicalite, mordenite and zeolite beta were taken from the works of Artioli et al.<sup>28</sup>, Gramlich<sup>29</sup> and Newsam et al.<sup>30</sup>, respectively.

**Table 3.1. Zeolite-MTBE nonbonded force field parameters**

Lennard-Jones			Columbic	
Interacting Sites	$\sigma$ (Å)	$\epsilon$ (K)	Sites	q(e)
OZ-O	4.56	10.0	Si	2.050
OZ-C	3.005	69.671	Al	1.75
OZ- CH <sub>3</sub>	3.48	93.0	Na	1.0
Na-O	4.065	4.837	<sup>a</sup> OZ <sub>Si-OZ-Si</sub> / OZ <sub>Si-OZ-Al</sub>	-1.025 / -1.200
Na-C	2.565	50.735	<sup>b</sup> CH <sub>3-CH3-O</sub> / CH <sub>3-CH3-C</sub>	0.25 / 0.0
Na- CH <sub>3</sub>	2.96	67.7	C	0.25
			O	-0.5

<sup>a</sup>OZ<sub>Si-OZ-Si</sub>: Oxygen of zeolite bridging two Si atoms, OZ<sub>Si-OZ-Al</sub>: Oxygen of zeolite bridging Si and Al atoms. <sup>b</sup>CH<sub>3-CH3-O</sub>: Methyl group bonded to oxygen atom of MTBE, CH<sub>3-CH3-C</sub>: Methyl group bonded to carbon atom of MTBE

The locations of aluminum sites were determined differently for each type of zeolite. For silicalite, there are several preferred aluminum sites reported in literature,<sup>31-36</sup> however, the T12 site is the only one which all these references reported in common. Therefore, the T12 site was chosen as the location of aluminum atoms in silicalite. For mordenite, we took the unit cell structure which reported preferred aluminum sites.<sup>29</sup> All these reported aluminum sites are close to each other and located in the same channel. We randomly chose one of these reported aluminum sites. For zeolite beta, we chose the aluminum sites randomly. In the cases of silicalite and mordenite there was evidence for the preferred aluminum sites from the literature, therefore, aluminum site selection for

these structures were not totally random. When we had to choose more than one aluminum site for silicalite and mordenite from the ones reported in literature we picked them so that they were apart from each other as much as possible. On the other hand, aluminum site selection in zeolite beta was totally random; however, again we tried to keep these sites as far apart as possible from each other in the case of multiple aluminum sites with one exception. Since aluminum site selection in zeolite beta was more random compared to two others, we wanted to investigate the effect of the distribution of aluminum sites on the adsorption of MTBE in zeolite beta. For this purpose we created an alternative structure where two aluminum atoms are separated by only one O-Si-O bridge (Al-O-Si-O-Al) which was contrary to what we had done until now for choosing the aluminum sites. In all structures described above we adhered to Lowenstein's<sup>47</sup> rule which precludes Al-O-Al bridges.

For Monte Carlo and molecular dynamics simulations we used the Towhee<sup>37</sup> and DL\_POLY<sup>38</sup> simulation packages, respectively. Periodic boundary conditions were applied in all directions. An Ewald sum was used to calculate the electrostatic interactions. For simulations in silicalite, two unit cells, and in mordenite four unit cells were used, and in zeolite beta four unit cells were used. Final simulation box dimensions for silicalite were  $a=20.0511 \text{ \AA}$ ,  $b=19.87570 \text{ \AA}$ ,  $c=26.73640 \text{ \AA}$ , for mordenite  $a=18.011 \text{ \AA}$ ,  $b=20.53 \text{ \AA}$ ,  $c=30.112 \text{ \AA}$ , and for zeolite beta  $a=25.32278 \text{ \AA}$ ,  $b=25.32278 \text{ \AA}$ ,  $c=26.40612 \text{ \AA}$ . Cutoff distances for each simulation were set less than half of the shortest box side to obey the minimum image convention,<sup>39</sup> which are  $9.5 \text{ \AA}$ ,  $9.0 \text{ \AA}$ , and  $12.0 \text{ \AA}$  for silicalite, mordenite, and zeolite beta, respectively. For liquid phase MTBE the simulation cutoff distance was  $12.0 \text{ \AA}$ . All simulations reported in this study were

performed at 298.15 K. During the molecular dynamics simulations temperature was kept constant by applying a Nose-Hoover<sup>40</sup> thermostat.

We started our simulations by taking Na<sup>+</sup> cations to their equilibrium positions. For this we made NVT Monte Carlo simulations where the number of molecules, volume, and temperature were kept constant, and the Na<sup>+</sup> cations were placed near the aluminum sites. For each zeolite simulation box we placed 1 to 4 Na<sup>+</sup> cations per system (not per unit cell). These loadings correspond to Si/Al ratios of 391, 195, 130, and 97 for silicalite and mordenite, and 255, 127, 84, and 63 for zeolite beta. Then, for 10 million steps, Na<sup>+</sup> cations were displaced randomly and zeolite structures were kept fixed. Final positions of the Na<sup>+</sup> cations were fixed and used for future Monte Carlo simulations.

Adsorption isotherms of MTBE for siliceous and Na<sup>+</sup>-loaded structures were obtained at 14 points over a pressure range from 10<sup>-5</sup> kPa to 5 kPa by Grand Canonical Monte Carlo (GCMC)<sup>41,42</sup> simulations where temperature, volume, and chemical potential were fixed. Prior to these simulations, chemical potentials at each pressure point were computed by the Widom Insertion Method<sup>43</sup> in a series of NPT Gibbs Ensemble Monte Carlo (GEMC) simulations.<sup>44-46</sup> In this ensemble, pressure, temperature, and the number of fluid molecules were fixed. A simulation box containing 100 MTBE molecules was set up. Translation and rotation moves of the MTBE molecules and the volume change of the simulation box were sampled with probabilities of 50%, 45% and 5%, respectively. At each pressure point the system was equilibrated for 20,000 cycles and a 20,000-cycle production run followed the equilibration run in which the chemical potential was measured by the Widom Insertion Method every five cycles. A cycle is equal to  $N$  Monte Carlo moves, where  $N$  is the number of molecules in the system.

The chemical potentials obtained at each pressure point were used to set up the simulations in the grand canonical ensemble to obtain the adsorption isotherms of MTBE in silicalite, mordenite, and beta zeolites. In these GCMC simulations insertion/deletion, regrowth, intramolecular atom translation, translation, and rotation of MTBE molecules were sampled with probabilities of 30%, 5%, 5%, 30%, and 30%, respectively. No biasing was applied for insertions. Each simulation started with a 10 million step equilibration run, which was followed by a 10 million step production run. Statistical uncertainties were calculated by dividing the production run into ten blocks. During the GCMC simulations zeolite structures and cation positions were kept fixed.

After the Monte Carlo simulations, molecular dynamics (MD) simulations of MTBE in silicalite, mordenite, and zeolite beta were carried out. These simulations were made with the maximum number of MTBE molecules adsorbed in the siliceous structures, 8, 9, and 31 for silicalite, mordenite, and zeolite beta, respectively. Additionally, we made a simulation of 69 MTBE molecules at its liquid density of 298.15 K. Radial distribution functions (RDF) of MTBE oxygen atoms in the liquid state and in the three zeolites were computed. In all MD simulations a time step of 0.5 fs was used. Systems were first equilibrated for 1 million steps, followed by a production run of 1 million steps. In MD simulations zeolite structures were flexible.

### **3.3. Results and Discussion**

A comparison of MTBE adsorption in all-silica silicalite, mordenite, and zeolite beta is given in Figure 3.1. At very low pressures silicalite and zeolite beta adsorb more MTBE than mordenite does. As the pressure increases the adsorbed MTBE amount in mordenite slightly exceeds that in silicalite. Zeolite beta, on the hand, is predicted to

adsorb significantly more MTBE compared to silicalite and mordenite. Silicalite reaches its saturation limit at a relatively low pressure, while mordenite reaches a slightly higher saturation limit at a slightly higher pressure. Although a saturation plateau was not observed for zeolite beta within the simulation pressure range it is not difficult to see that the adsorption isotherm is converging to a limiting value. Here, the most interesting outcome is zeolite beta's predicted adsorption capacity compared to silicalite and mordenite, since these three zeolites have similar pore volumes (Table 3.2). However, amount of MTBE adsorbed by zeolite beta is almost three times greater than that adsorbed by silicalite or mordenite. Snapshots of the simulations revealed that the reason behind this significant difference was that while not all the pores in silicalite and mordenite were accessible to MTBE molecules, zeolite beta pores are all large enough to accommodate MTBE molecules, thus enhancing its capacity.

**Table 3.2. Pore volumes (cm<sup>3</sup>/gr) of silicalite, mordenite and zeolite beta.**

Silicalite	Mordenite	Zeolite beta
0.21 <sup>a</sup>	0.18-0.20 <sup>a</sup>	0.23 <sup>a</sup> , 0.26 <sup>b</sup>

<sup>a</sup> Reference 16, <sup>b</sup> Reference 19

Adsorption of MTBE in silicalite, mordenite, and zeolite beta with increasing number of Na<sup>+</sup> cations and their comparison with all siliceous structures are shown in Figure 3.2-3.4, respectively. In silicalite all adsorption isotherms converged to a common limiting value at higher pressures, regardless of the Na<sup>+</sup> content. At very low pressures, however, increasing the Na<sup>+</sup> content increased the silicalite adsorption capacity significantly; a similar conclusion can be drawn for zeolite beta. The increased capacity with increasing Na<sup>+</sup> levels is attributed to the orientation of the ether oxygen's affinity for

the cation sites; alignment of the ether oxygen and  $\text{Na}^+$  ions was apparent in the visual images of the simulation results.

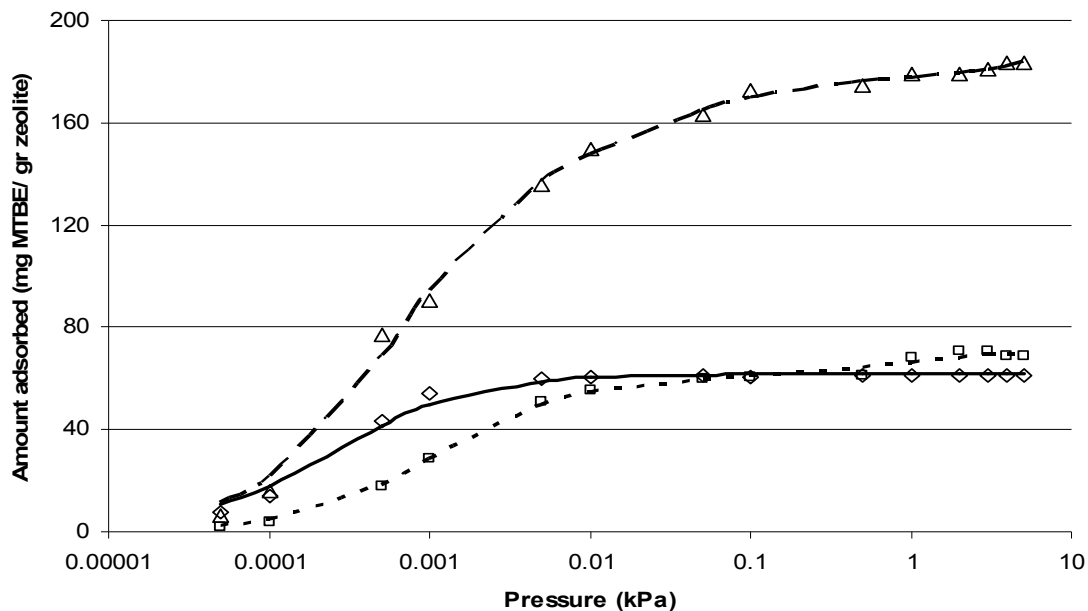


Figure 3.1. Comparison of MTBE adsorption in siliceous zeolites: ( $\diamond$ ) silicalite, ( $\square$ ) mordenite and ( $\Delta$ ) beta. Lines represent fitted curves.

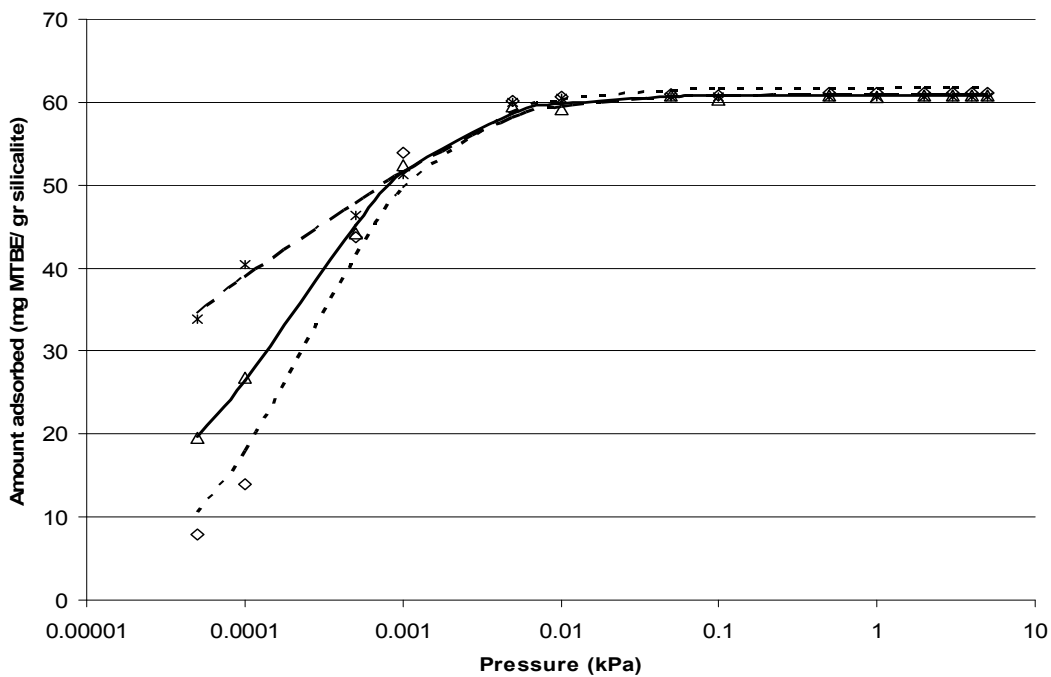


Figure 3.2. Effect of increasing  $\text{Na}^+$  content on MTBE adsorption in silicalite: ( $\diamond$ ) siliceous, ( $\Delta$ ) Si/Al=195 and ( $*$ ) Si/Al=97. Lines represent the fitted curves.

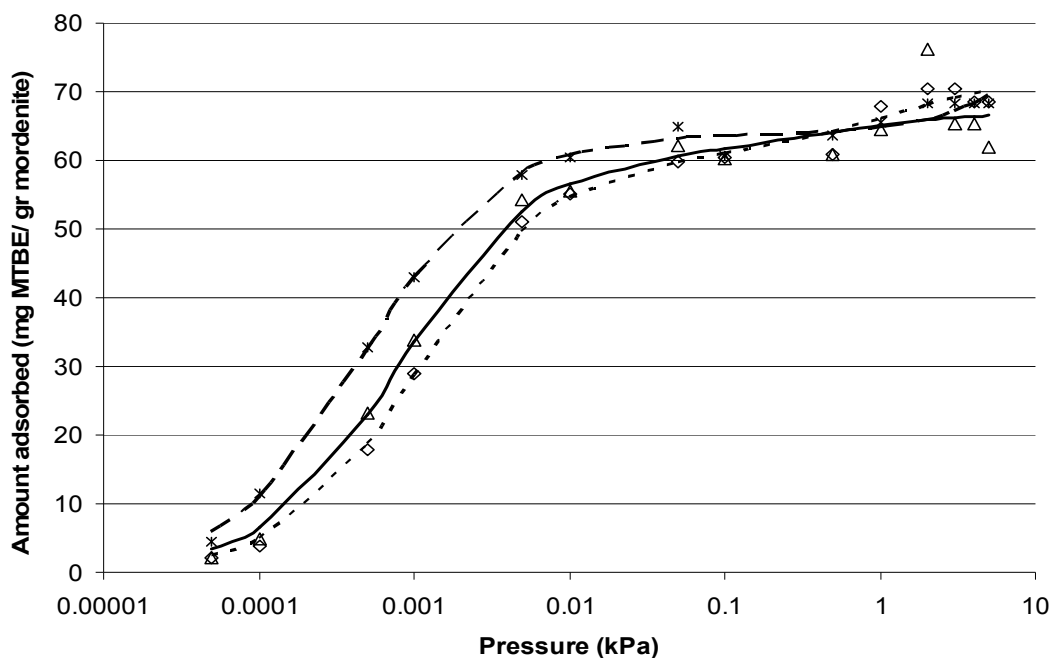


Figure 3.3. Effect of increasing  $\text{Na}^+$  content on MTBE adsorption in mordenite: (◇) siliceous, (Δ) Si/Al=195 and (\*) Si/Al=97. Lines represent the fitted curves.

However, for mordenite the picture is a little different. Although the adsorption isotherms converged to a similar limiting value as in the case of silicalite and zeolite beta, at lower pressures increasing the  $\text{Na}^+$  content did not increase the amount of MTBE adsorbed. This result stemmed from the location of  $\text{Na}^+$  cations in the structure. In silicalite and zeolite beta the cations are located in pores which are accessible to MTBE molecules, whereas in mordenite the cations are in the pores which can not be accessed by MTBE molecules. Therefore, clustering of MTBE molecules around  $\text{Na}^+$  cations was not observed in mordenite. However, in silicalite and zeolite beta, MTBE molecules near  $\text{Na}^+$  cations oriented in such a way that their oxygen atoms look towards to the  $\text{Na}^+$  cations. This orientation can be seen in Figure 3.5, in which the MTBE oxygen's association with the  $\text{Na}^+$  cations in silicalite is observed.

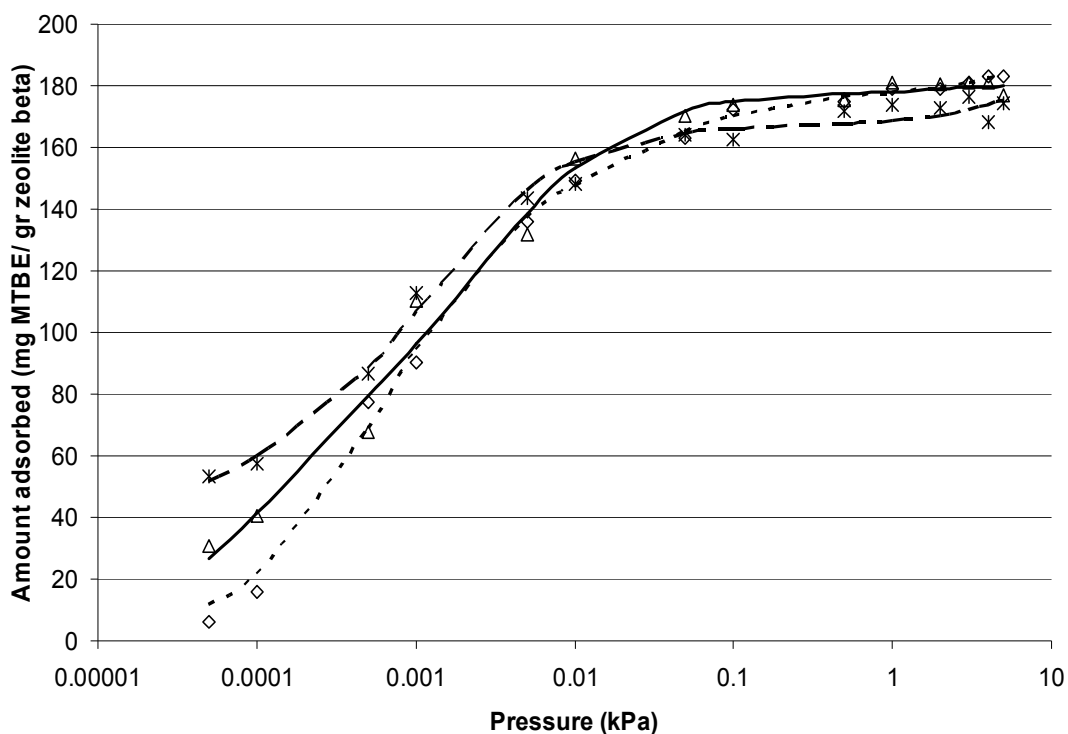


Figure 3.4. Effect of increasing  $\text{Na}^+$  content on MTBE adsorption in zeolite beta: (◇) siliceous, (Δ) Si/Al=127 and (\*) Si/Al=63. Lines represent the fitted curves.

In Figure 3.6, adsorption of MTBE in two zeolite beta structures with same Si/Al ratio, but different aluminum site distributions, were compared. There is not much difference between the amounts of MTBE adsorbed at higher pressures. However, the low pressure region deserves some comment. In the case where aluminum sites were chosen to be far from each other, the amount of MTBE adsorbed is greater than the case where aluminum atoms are only separated by an O-Si-O bridge. This could be due to the fact that MTBE molecule is too big such that once an MTBE molecule is adsorbed by a  $\text{Na}^+$  cation it occupies the space that the adjacent  $\text{Na}^+$  needs to adsorb another MTBE molecule. This situation obviously presents an obstacle to the adsorption of new MTBE

molecules. On the other hand, when aluminum sites are apart from each other adsorbed MTBE molecules present no physical barrier to each other.

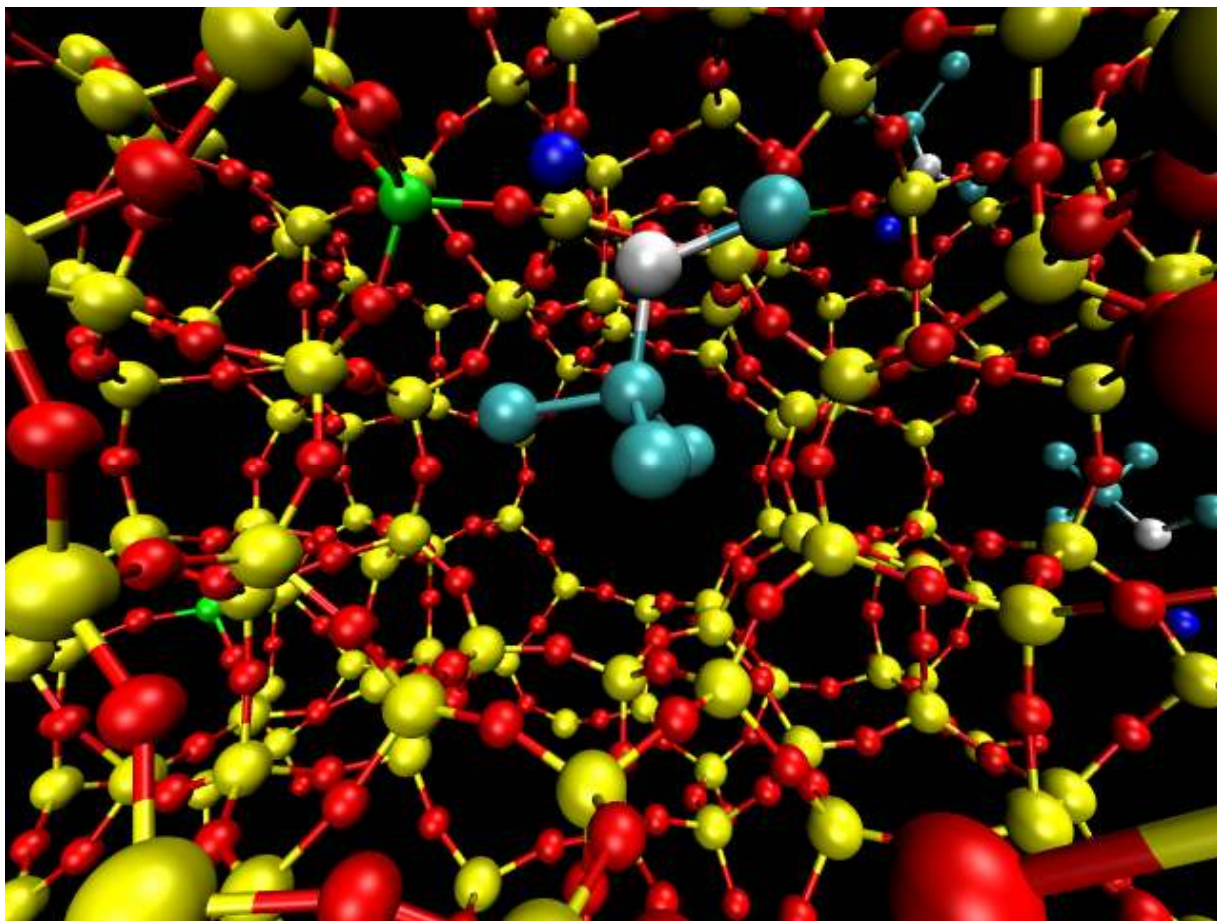


Figure 3.5. Orientation of MTBE molecule near  $\text{Na}^+$  cation in silicalite (Si/Al=97). MTBE oxygen atom (white), carbon (cyan), zeolite oxygen (red), silicon (yellow), aluminium (green),  $\text{Na}^+$  (blue).

Figure 3.7 shows the radial distribution functions (RDFs) of oxygen atoms of MTBE in all-silica silicalite, mordenite, and zeolite beta in comparison with the RDF of liquid MTBE. The structure of MTBE molecules in zeolite beta is very close to that in the liquid state, due to its large and accessible pore structure. The RDF of MTBE in mordenite shows a somewhat denser structure than in its liquid state as peaks are present in shorter distances due to the fact that MTBE molecules are packed in only one channel.

In silicalite on the other hand, the liquid structure is completely disrupted since MTBE molecules are only adsorbed in the intersections of the straight and zig-zag pores. For this reason they remain relatively far away from each other. The intersection cavities along the same straight channel are the ones that are closest to each other. The distance between the centers of these adjacent cavities is approximately 8.7 Å, which is the separation distance at which we observe the first significant peak in Figure 3.7 for MTBE in silicalite.

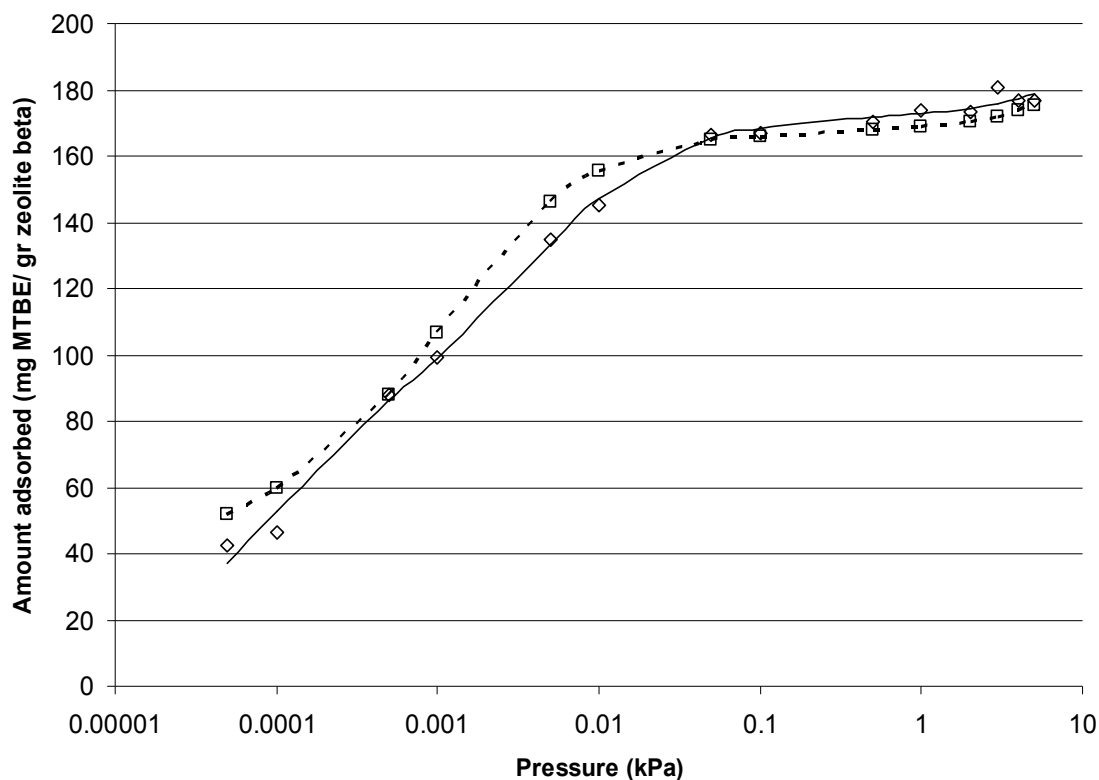


Figure 3.6. Effect of aluminium site distribution on the adsorption of MTBE in zeolite beta (Si/Al=63): ( $\diamond$ ) aluminium sites were kept as far as possible from each other, ( $\square$ ) aluminum sites are only separated by an O-Si-O bridge.

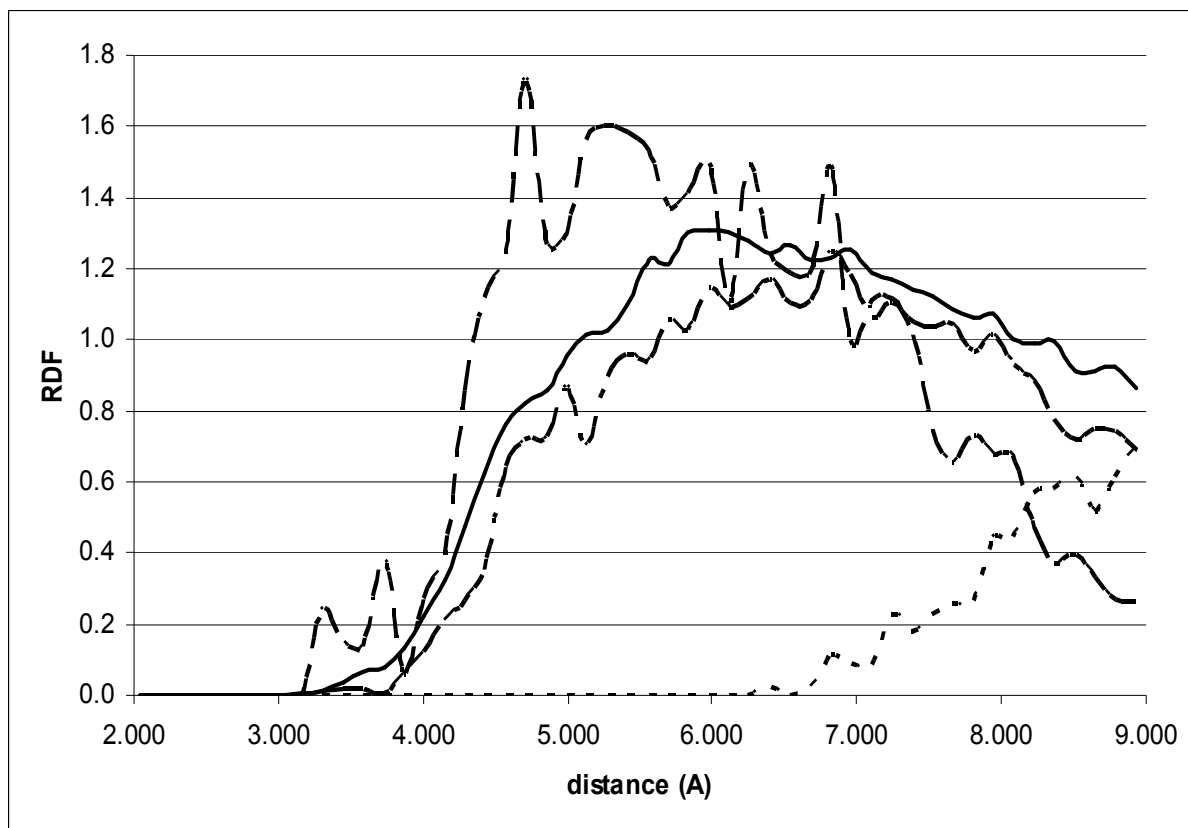


Figure 3.7. Comparison of RDF of oxygen atoms of liquid MTBE (—) and RDFs of oxygen atoms of MTBE adsorbed in siliceous silicalite (- - -), mordenite (- -) and zeolite beta (- · -).

The high density profile of MTBE at high pressures in mordenite caused inconsistency in the results as can be seen in Figure 3.3. The adsorption data do not converge to a certain value as in silicalite, but instead fluctuate. The relation between high density and inconsistency of data points at high densities was due to the high statistical error in molecule insertion. Most of the insertion attempts were energetically high, because as the density increases it becomes increasingly difficult to find an empty space to insert a new molecule. These high energy insertion attempts contributed something almost zero to the average insertion weight. A non-zero value was added to the average weight when a good conformation was found, which was rare. Eventually,

averaging was done on something that was mostly zero, but rarely a relatively large non-zero number, which makes the statistics quite poor. If the insertions were biased, smoother isotherms could have been obtained due to the increased number of successful insertions. In all simulations the acceptance ratio of insertion moves was not larger than 0.15%.

### **3.4. Conclusions**

Monte Carlo and molecular dynamics simulations of MTBE adsorption in silicalite, mordenite, and zeolite beta with different  $\text{Na}^+$  cation loadings were carried out. The results reveal the importance of the pore structure on the adsorption of MTBE. Although these three zeolites have similar pore volumes, zeolite beta, with its pore structure which is mostly accessible to MTBE molecules, is predicted to adsorb significantly more MTBE than silicalite and mordenite. The  $\text{Na}^+$  cation loading, up to four cations does not have a significant effect on the adsorption capacity of the zeolites studied here, however, for silicalite and zeolite beta increasing the  $\text{Na}^+$  content increases the amount adsorbed at very low pressures. On the other hand, the location of  $\text{Na}^+$  cations in mordenite precludes an effect, since the cations are in pores which are not accessible to MTBE molecules. It was found that MTBE is in a less dense state in silicalite, whereas in mordenite and zeolite beta it has a structure close to its liquid state.

## Bibliography

43. <http://www.epa.gov/epa>
44. Office of Environmental Health Hazard Assessment; *Public Health Goal for Methyl Tertiary Butyl Ether (MTBE) in Drinking Water*; OEHHA, California EPA, 1999.
45. Environmental Protection Agency; *2002 Edition of the Drinking and Health Advisories*; Washington, DC U.S, 2002.
46. Squillace, P.J.; Pankow, J.F.; Korte, N.E.; Zogorski, J.S. *Environ. Toxicol. Chem.* **1997**, 16, 1836.
47. Leitner, N.K.V.; Papailhou A.L.; Croue J.P.; Peyrot J.; Dore M. *Ozone Science and Engineering* **1994**, 16, 41.
48. Liang, S.; Palencia L.S.; Yates R.S.; Davis M.K., Brunol J.M.; Wolfe R.L. *J. Am. Water Works Assoc.* **1994**, 91, 104.
49. Mormile, M.R.; Liu S.; Suflita J.M. *Environ. Sci. Technol.* **1994**, 1727-1732.
50. Acero, J.L.; Haderlein S.B.; Schmidt T.C.; Suter, M.J.F.; von Gunten U. *Environ. Sci. Technol.* **2001**, 35, 4252.
51. Howard, P. H.; Sage, G. W.; Jarvis, W. F.; Gray, D. A. *Handbook of Environmental Fate and Exposure Data for Organic Chemicals, Volume 2*. Lewis, Chelsea (Mich.), 1991.

52. Lyman, W. J.; Reehl, W. F.; Rosenblatt, D. H *Handbook of Chemical Property Estimation Methods: Environmental Behavior of Organic Chemicals*; American Chemical Society, Washington DC, 1990.
53. Stocking, A. J.; Suffet, I. H.; McGuire, M. J.; Kavanaugh, M. C. *J. Am. Water Works Assoc.* **2001**, 93, 95.
54. Robbins, G. A.; Wang, S.; Stuart, J. D. *Anal. Chem.* **1993**, 65, 3113.
55. Tesseraux, I.; Koss, G. *Bundesgesundheitsblatt* **1999**, 4, 332.
56. Squillace, P. J.; Pankow, J. F.; Kortés, N. E.; Zogorski, J. S. *Environmental Behavior and Fate of Methyl tert-Butyl Ether (MTBE)*, US Department of the Interior, US Geological Survey, National Water Quality Assessment Program (NAWQA), USGS Series Fact Sheet, USGS Library Call Number (200)F327 No. 96\_203, 1996.
57. Williams, P. R. D.; Benton, L.; Warmerdam, J.; Sheehan, P. J. *Environ. Sci. Technol.* **2002**, 36, 4721.
58. Erdem-Şenatalar, A.; Bergendahl, J.A.; Giaya, A.; Thompson, R.W. *Environ. Eng. Sci.* **2004**, 21, 722.
59. Knappe, D.R.U.; Campos, A.A.R. *Water Sci. and Tech. : Water Supply* **2005**, 5, 83.
60. Anderson, M.A. *Environ. Sci. Technol.* **2000**, 34, 725.
61. Shiguang, L.; Tuan, V.A; Noble, R.D.; Falconer, J.L. *Environ. Sci. Technol.* **2003**, 37, 4007.
62. Martin, M.G.; Siepmann, J.I. *J. Phys. Chem. B* **1998**, 102, 2569.

63. Martin, M.G.; Siepmann, J.I. *J. Phys. Chem. B* **1999**, 103, 4508.
64. Chen, B.; Potoff, J.J.; Siepmann, J.I. *J. Phys. Chem. B* **2001** 105, 3093.
65. Stubbs, J.M.; Potoff, J.J.; Siepmann, J.I. *J. Phys. Chem. B* **2004** 108, 17596.
66. Giaya, A.; Thompson, R. W. *J. Chem. Phys.* **2002** 117, 3464.
67. Jaramillo, E.; Auerbach, S. M. *J. Phys. Chem. B* **1999**, 103, 9589.
68. Beerdsen, E.; Dubbeldam, D.; Smit, B.; Vlugt, T.J.H.; Calero, S. *J. Phys. Chem. B* **2003**, 107, 12088.
69. Dubbeldam, D.; Calero, S.; Vlugt, T. J. H.; Krishna, R.; Maesen, T. L. M.; Smit, B. *J. Phys. Chem. B* **2004**, 108, 12301.
70. Artioli, G.; Lamberti, C.; Marra, G.L. *Acta. Cryst. B* **2000**, 56, 2.
71. Gramlich, V. Ph.D. Thesis, ETH, Zürich, Switzerland, , (1971).
72. Newsam, J.M.; Treacy, M.M.J.; Koetsier, W.T.; de Gruyter, C.B.; *Proc. R. Soc. Lond. A* **1998**, 420, 375.
73. Fripiat, J. G.; Berger-Andre, F.; Andre, J.-M.; Derouane, E. G. *Zeolites* **1983**, 3, 306.
74. Lonsinger, S. R.; Chakraborty, A. K.; Theodorou, D. N.; Bell, A.T. *Catal. Lett.* **1991**, 11, 209.
75. Olson, D. H.; Khosrovani, N.; Peters, A. W.; Toby, B. H. *J. Phys.Chem. B* **2000**, 104, 4844.

76. Redondo, A.; Hay, P. G. *J. Phys. Chem.* **1993**, 97, 11754.
77. de Vos Burchart, E.; van Bekkum, H.; van der Graaf, B. *Collect.Czech. Chem. Commun.* **1992**, 57, 681.
78. Alvarado-Swaisgood, A. E.; Barr, M. K.; Hay, P. J.; Redondo, A. *J. Phys. Chem.* 1991, 95, 10031.
79. <http://towhee.sourceforge.net>
80. Smith, W.; Forester, T. *J. Molec. Graphics* **1996**, 14, 136.
81. Allen, M.P.; Tildesley, D.J., *Computer Simulation of Liquids*; Clarendon Press: Oxford, 1989.
82. Hoover, W.G. *Phys. Rev. A* **1985**, 31 1695.
83. Nicholson, D.; Parsonage, N. G. *Computer Simulation and the Statistical Mechanics of Adsorption*; Academic Press: New York, 1982.
84. Frenkel, D.; Smit, B. *Understanding Molecular Simulations. From Algorithms to Applications, 2nd ed.*; Academic Press: London. 2002.
85. Widom, B. *J. Chem. Phys.* **1963**, 39, 2802.
86. Panagiotopoulos, A. Z. *Molec. Phys.* **1987**, 61, 813.
87. Panagiotopoulos, A. Z.; Quirke, N.; Stapleton, M.; and Tildesley, D. J. *Molec. Phys.* **1988**, 63, 527.
88. Smit, B.; Desmedt, P.H.; and Frenkel, D. *Molec. Phys.* **1989**, 68, 931.

47. Lowenstein, W. *Am. Mineral.* **1954**, 39, 92.

48. Auerbach, S. M.; Henson, N. J.; Cheetham, A. K.; Metiu, H. I. *J.Phys. Chem.* **1995**, 99, 10600.

#### **4. SIMULATING the VAPOUR-LIQUID EQUILIBRIA of 1,4-DIOXANE**

1,4-Dioxane, a cyclic ether, is an emerging contaminant which is difficult to remove from water with conventional water treatment methods and resistant to biodegradation. Once a reliable force field is developed for 1,4-Dioxane, molecular simulation techniques can be useful to study alternative adsorbents for its removal. For this purpose, we carried out Monte Carlo simulations in a constant volume Gibbs Ensemble to generate a force field which is capable of predicting the vapour-liquid coexistence curve and critical data of 1,4-Dioxane. Results are given in comparison with experimental data and results from simulations with other force fields. Liquid densities and critical temperature are predicted in excellent agreement with experimental data using the new force field. At high temperatures, predicted vapour densities are in good agreement with experimental data, however, at lower temperatures the predicted vapour densities deviate about an order of magnitude from the experimental values. The critical density is slightly underestimated with our new force field. However, overall, the results of simulations with the new parameters give much better agreement with experimental data compared to the results obtained using other force fields.

##### **4.1. Introduction**

1,4-Dioxane is a cyclic ether and listed as one of the emerging contaminants by US Environmental Protection Agency (EPA). By emerging, it is meant that it has not until recently been seen as a chemical of concern for the EPA's remedial action programs.<sup>1</sup> Even short exposure to high levels of 1,4-Dioxane has caused vertigo and irritation of the eyes, nose, throat, lungs, and skin in humans.<sup>2,3</sup> Rats and mice exposed to 1,4-Dioxane in their drinking water developed liver carcinomas and adenomas and nasal

cavity squamous cell carcinomas.<sup>4</sup> As a result the, EPA has classified 1,4-dioxane as a Group B2, probable human carcinogen.<sup>5</sup>

1,4-Dioxane is a large production chemical, used as a stabilizer for chlorinated solvents, and during the manufacture of polyester and various polyethoxylated compounds it is formed as a by-product. Improper disposal of industrial wastes and accidental solvent spills have resulted in the contamination of groundwater with 1,4-Dioxane.<sup>6</sup> Carbon adsorption and air stripping do not remove 1,4-Dioxane efficiently from water due to the fact that 1,4-Dioxane is infinitely soluble in water and has a low vapour pressure. The boiling point of 1,4-Dioxane (bp = 101°C) makes distillation extremely costly [7]. Due to its high resistance to biotransformation conventional biological processes fail as effective means of treatment.<sup>8,9</sup> Advanced oxidation technologies, utilizing hydrogen peroxide, ozone, and/or UV photo oxidation, are the only processes proven to reduce 1,4-dioxane in substantial amounts, however, they are not cost effective.<sup>10,11</sup>

We are interested in simulating the adsorption of 1,4-Dioxane in nanoporous materials, since other remediation technologies appear to be ineffective. However, in order to do that, reliable parameters are required. To our knowledge a force field has not been developed specifically for 1,4-Dioxane or cyclic ethers although 1,4-Dioxane and tetrahydrofuran are industrially important solvents. There are a few molecular simulation studies in the literature about 1,4-Dioxane, but they are all liquid 1,4-Dioxane simulations.<sup>12,15</sup> When simulating fluids in nanoporous materials it is important to have a force field which is capable of predicting the phase equilibria and critical data of the fluid of interest, since fluids may undergo a phase transition when they are confined in

nanoporous materials.<sup>16</sup> In this study, we present our work on developing a force field for 1,4-Dioxane which is capable of estimating its phase equilibria and critical point data. We also present the results of Configurational Bias Monte Carlo (CBMC) simulations using this new force field in comparison with available experimental data and the results of simulations performed with other force fields.

#### 4.2. Model and Simulation Details

We used a pairwise-additive potential in the form of 12-6 Lennard-Jones (LJ) plus columbic potential to compute the site-site nonbonded interactions:

$$V_{ij} = 4\varepsilon_{ij} \left[ \left( \frac{\sigma_{ij}}{r_{ij}} \right)^{12} - \left( \frac{\sigma_{ij}}{r_{ij}} \right)^6 \right] + \frac{q_i q_j}{4\varepsilon_0 r_{ij}}$$

where  $i$  and  $j$  are methylene and oxygen sites of 1,4-dioxane, and  $r_{ij}$  is the distance between sites  $i$  and  $j$ .  $\varepsilon_{ij}$  and  $\sigma_{ij}$  are LJ well depth and diameter, respectively.  $q_i$  and  $q_j$  are the partial charges of the interacting sites. To maintain the bonds and bending angles flexible a simple harmonic potential was used for both terms

$$V_{bond} = k_r (r - r_0)$$

$$V_{bend} = k_\theta (\theta - \theta_0)$$

where  $r$ ,  $r_0$ ,  $k_r$  are the measured bond length, the equilibrium bond length, and the bond force constant, respectively; and  $\theta$ ,  $\theta_0$ ,  $k_\theta$  are the measured bending angle, the equilibrium bending angle, and the bending force constant, respectively. A cosine series was employed for torsional interactions of sites separated by three bonds

$$V_{tors} = c_0 + c_1 [1 + \cos(\phi)] + c_2 [1 - \cos(2\phi)] + c_3 [1 + \cos(3\phi)]$$

where  $\phi$  and  $c_i$  are the dihedral angle and the  $i_{\text{th}}$  coefficient, respectively. 1-4 nonbonded interactions within the same molecule were scaled by a factor of 0.5 in addition to the torsional potential.

To compare our force field with others we performed simulations using the non-bonded parameters developed for ethers in OPLS-UA,<sup>17</sup> and Trappe-UA<sup>18,21</sup> force fields, and using the non-bonded parameters from the works of Geerlings et al.<sup>14</sup> and Krienke et al.<sup>15</sup> where they simulated 1,4-Dioxane in its liquid state (see Table 4.1). All force fields mentioned here model the methylene group as a united atom. In the new force field partial charges for oxygen and methylene sites were taken from OPLS-UA force field. These partial charges are also used by the Trappe-UA force field and very close to the values derived from the quantum mechanical calculations.<sup>15</sup> Lorentz-Berthelot (LB) mixing rules, given by

$$\varepsilon_{ij} = \sqrt{\varepsilon_{ii}\varepsilon_{jj}} \text{ and } \sigma_{ij} = \frac{\sigma_{ii} + \sigma_{jj}}{2}$$

were used to calculate the nonbonded pair interactions in our new force field, as is the case in the work of Krienke et al.<sup>15</sup> and in the Trappe-UA force field. OPLS-UA force field, on the other hand, uses geometric mixing rules.

$$\varepsilon_{ij} = \sqrt{\varepsilon_{ii}\varepsilon_{jj}} \text{ and } \sigma_{ij} = \sqrt{\sigma_{ii}\sigma_{jj}}$$

The mixing rule used by Geerlings et al.<sup>14</sup> is a complex one which is a function of the polarizability of the interacting sites. They mentioned setting the polarizabilities of oxygen and methylene to the polarizabilities of water and methane, respectively; however, they neither reported the resulting values nor cited any reference for the polarizabilities. The only thing they reported was that they used the LJ parameters of OPLS-UA force

field and after the mixing rule was applied the resulting values between unlike sites were slightly different from those obtained from geometric mixing rules. Therefore, we decided to use geometric mixing rules for the LJ parameters of Geerlings et al.<sup>14</sup>.

**Table 4.1. Non-bonded force field parameters used in this study.**

	New Force Field		Trappe-UA <sup>a</sup>		OPLS-UA <sup>b</sup>		Geerlings <sup>c</sup>		Krienke <sup>d</sup>	
	O	CH <sub>2</sub>	O	CH <sub>2</sub>	O	CH <sub>2</sub>	O	CH <sub>2</sub>	O	CH <sub>2</sub>
$\sigma$ (Å)	2.80	3.85	2.80	3.95	3.07	3.905	3.07	3.905	3.0	3.80
$\epsilon / k_B$ (K)	98.0	51.3	55.0	46.0	85.55	59.38	85.55	59.38	85.5	59.4
$q$ ( $e$ )	-0.5	0.25	-0.5	0.25	-0.5	0.25	-0.35	0.175	-0.46	0.25

<sup>a</sup>Ref 18-21, <sup>b</sup>Ref 17, <sup>c</sup>Ref 14, <sup>d</sup>Ref 15.

We used a single set of intramolecular potential in all our simulations regardless of the source of non-bonded terms, since each of these force fields we found in literature treat intramolecular terms differently (see Table 4.2). The bonding parameters used for ether oxygen and carbon atoms in the Amber<sup>22</sup> force field were used to maintain flexible bonds in our simulations. Angle bending and CH<sub>2</sub>-CH<sub>2</sub>-O-CH<sub>2</sub> torsion parameters were taken from the OPLS-UA force field. O-CH<sub>2</sub>-CH<sub>2</sub>-O torsion parameters were taken from the Amber force field.

All simulations were performed using the *Towhee*<sup>23</sup> Monte Carlo code and in the constant volume version of the Gibbs ensemble.<sup>24-26</sup> A total number of 180 molecules were used in two boxes in which two phases were formed eventually. Periodic boundary conditions were applied in all directions. The Ewald sum method was employed to calculate the electrostatic interactions. A cut-off distance of 10 Å was used. Simulations

were performed within a range of temperatures from 298.15 K to 525 K. Simulations were run for 20,000 cycles to equilibrate the system, followed by a 20,000-cycle production run. A cycle is equal to  $N$  Monte Carlo moves, where  $N$  is the number of molecules in the system. Statistical uncertainties were calculated by dividing the production run into 20 blocks.

**Table 4.2. Parameters for intramolecular terms.**

Bonding		
	CH <sub>2</sub> -CH <sub>2</sub>	O-CH <sub>2</sub>
$k_{\text{bond}}/k_B$ (K)	155997.15	161029.32
$r_0$ (Å)	1.54	1.41
Angle Bending		
	CH <sub>2</sub> -CH <sub>2</sub> -O	CH <sub>2</sub> -O-CH <sub>2</sub>
$k_{\text{bend}}/k_B$ (K)	25150	30200
$\theta_0$ (°)	112.0	112.0
Torsion		
	O-CH <sub>2</sub> -CH <sub>2</sub> -O	CH <sub>2</sub> -CH <sub>2</sub> -O-CH <sub>2</sub>
$c_0/k_B$ (K)	503.24	0.0
$c_1/k_B$ (K)	0.0	725.35
$c_2/k_B$ (K)	-251.62	-163.75
$c_3/k_B$ (K)	1006.47	558.20

Cyclic molecules are quite difficult to grow using standard CBMC methods, because the probability of closing a ring structure during the growth process is almost zero. Additional biasing is required during the growth procedure in order to encourage the growth to form reasonable ring closures. Therefore, in addition to the standard

Coupled-Decoupled CBMC<sup>19</sup> method that *Towhee* employs, a Fixed Endpoint CBMC<sup>27,28</sup> method also was used.

Some analytical biasing functions are used in this method. These functions transform the distance between growth atoms and target ring atoms consistently, into a bias function which depends loosely on dihedral, bending, and vibrational energies.

We optimized the LJ parameters of oxygen and methylene for our new force field by systematically modifying them to predict the vapour-liquid coexistence curve (VLCC) and the critical data of 1,4-Dioxane satisfactorily. We started this optimization procedure by taking oxygen LJ parameters of Trappe-UA and methylene LJ parameters of Fox et al.<sup>38</sup> The critical temperatures ( $T_c$ ) and densities ( $\rho_c$ ) were calculated using the saturated density scaling law<sup>29,30</sup> and the law of rectilinear diameters with a scaling exponent of  $\beta = 0.3047$ .<sup>31</sup> After the LJ parameters were optimized we investigated the finite size effects by carrying out the simulations with 300 molecules.

The Monte Carlo moves consisted of volume changes of boxes between each other, swap moves between two boxes, regrowths of the molecules, intramolecular single atom translation, translation of the centre-of-mass, and rotation about the centre-of-mass with corresponding probabilities of 3%, 25%, 5%, 7%, 30%, 30%, respectively. All simulations were performed on *64-bit AMD Opteron, 2.4 GhZ* cpus. A typical simulation involving 180 molecules took 5 hours per 10,000 cycles.

### 4.3. Results and Discussion

The VLCC, critical temperature, and density of 1,4-dioxane are given in Figure 4.1, along with the results of our simulations using our new force field, as well as the predictions using the parameters from Trappe-UA and OPLS-UA force fields, and from

the works of Geerlings et al.,<sup>14</sup> and Krienke et al.<sup>14</sup> Our new force field gives excellent agreement with experimental liquid densities while the liquid densities calculated using the parameters from other force fields showed different degrees of deviation. Liquid densities predicted by using the OPLS-UA force field underestimate the experimental data in the low temperature region, but then overestimate as the temperature increases. The parameters of Geerlings et al.<sup>14</sup> yielded similar behaviour at lower temperatures by underestimating the liquid densities; however, at higher temperatures predictions were more successful. Results obtained using the parameters of Krienke et al.<sup>15</sup> overestimate the experimental liquid densities. In the case of the Trappe-UA force field, results deviated significantly from the experimental data by underestimating them. The Trappe-UA force field is specifically parameterized for estimating phase equilibria and the results of ordinary ether molecules simulated by Trappe-UA reproduces experimental data quite successfully.<sup>21</sup> However, it is interesting to see that when a cyclic ether is modelled with the same parameters the differences can be rather large.

The critical temperature estimated with our new force field is also in excellent agreement with the experimental critical temperature data (see Table 4.3). On the other hand, the critical temperature estimated using the parameters of OPLS-UA, Geerlings et al.,<sup>14</sup> and Krienke et al.<sup>15</sup> overestimate, and Trappe-UA force field underestimate the critical temperature. The critical density is slightly underestimated with our force field, but still gives good agreement with experimental data, particularly with the value given in<sup>32</sup> (see Table 4.2). When compared to the critical density estimated using parameters from other sources our force field gives better agreement with the experimental critical density.

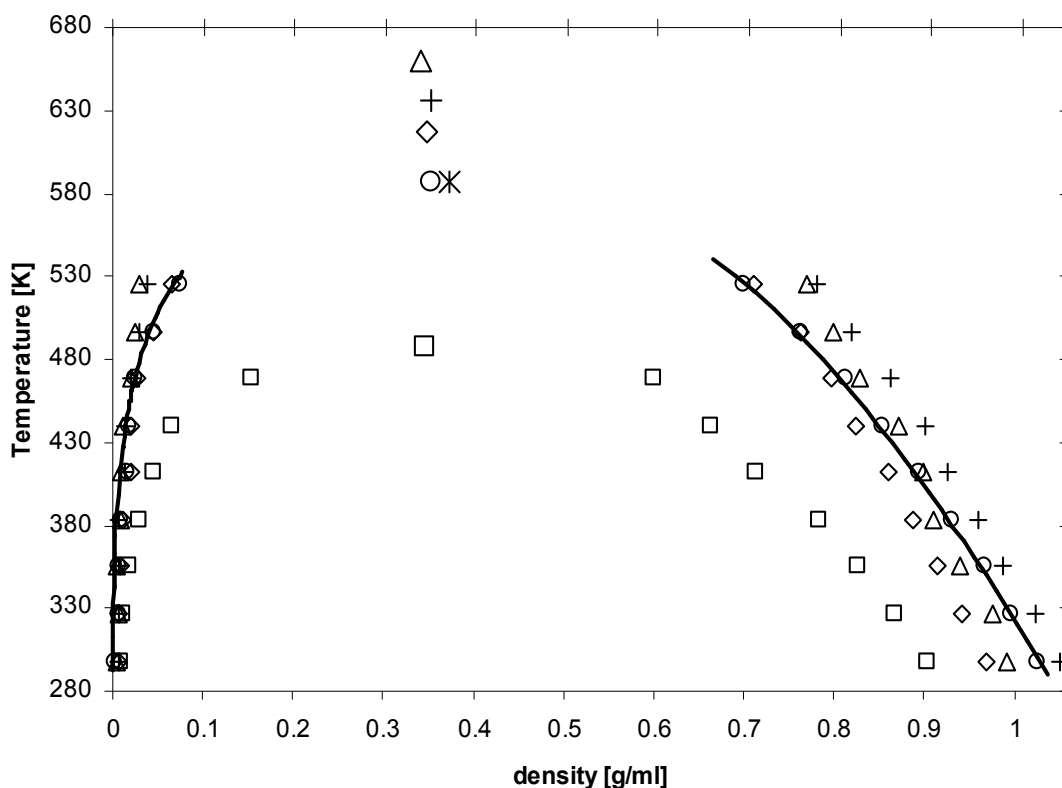


Figure 4.1. Vapour-liquid coexistence curve for 1,4-dioxane. New force field ( $\circ$ ), Trappe-UA ( $\square$ ), OPLS-UA ( $\Delta$ ), Geerlings ( $\diamond$ )<sup>14</sup>, Krienke (+)<sup>15</sup>, Experimental critical data (\*). Solid lines represent the experimental liquid densities<sup>31</sup> and vapour densities calculated from the experimental vapour pressure<sup>33</sup> using Pitzer's<sup>34</sup> method.

**Table 4.3. Comparison of the critical density and temperature obtained from experiments and simulations with the new force field. The subscripts denote the statistical uncertainties in the last digit(s) where available.**

	$T_c$ (K)		$\rho_c$ (g/ml)	
simulation	experimental	simulation	experimental	
587 <sub>23</sub>	585.15 <sup>a</sup> , 588 <sup>b</sup> , 588.15 <sup>c</sup> , 587.3 <sup>d</sup> , 587 <sup>e</sup>	0.354 <sub>24</sub>	0.360329 <sup>f</sup> , 0.37018 <sup>g</sup>	

<sup>a,f</sup>Ref 32; <sup>b</sup>Ref 35; <sup>c</sup>Ref 36; <sup>d</sup>Ref 37; <sup>e,g</sup>Ref 31

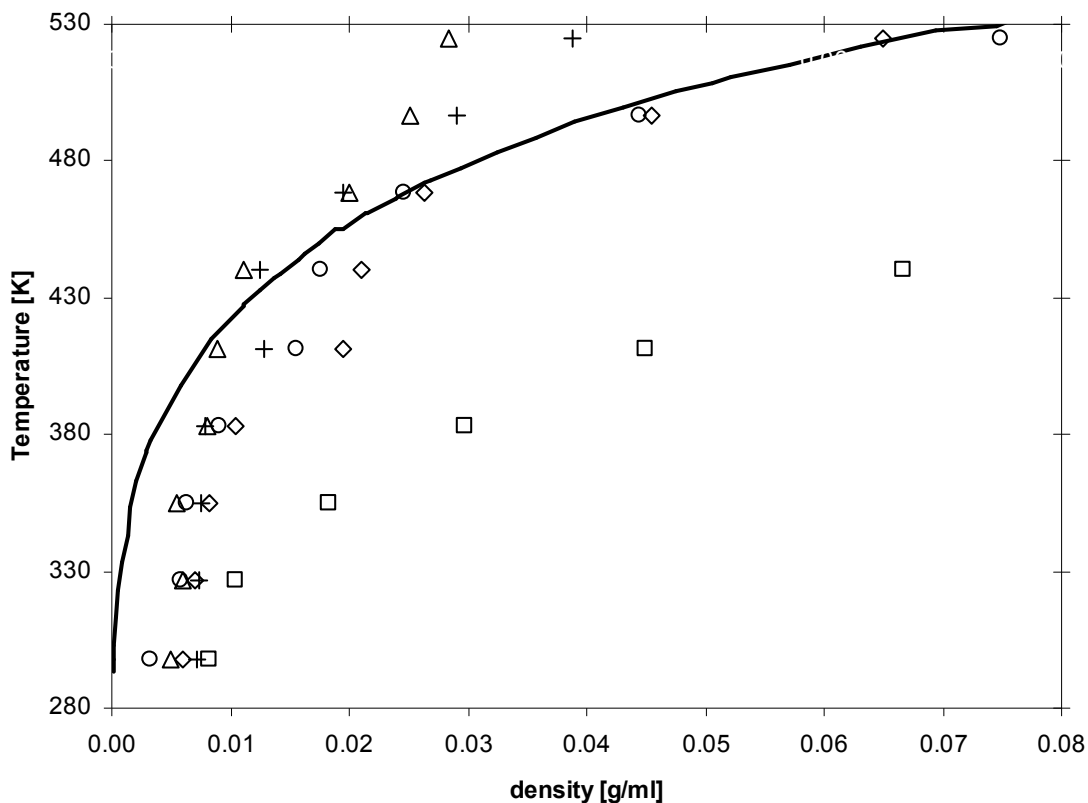


Figure 4.2. A magnified view of the vapour densities. New force field ( $\circ$ ), Trappe-UA ( $\square$ ), OPLS-UA ( $\Delta$ ), Geerlings ( $\diamond$ )<sup>14</sup>, Krienke ( $+$ )<sup>15</sup>. Solid line represent the vapour densities calculated from the experimental vapour pressures<sup>33</sup> using Pitzer's<sup>34</sup> method.

To our knowledge experimental vapour densities of 1,4-dioxane are not available in the literature, so we estimated them using experimental vapour pressures<sup>33</sup> and the method of Pitzer et al.<sup>34</sup> A magnified view of the vapour densities section of Figure 4.1 is given in Figure 4.2. The predicted vapour densities using the Trappe-UA force field underestimate the vapour densities computed from experimental vapour pressure. When the parameters of OPLS-UA force field and Krineke et al.<sup>15</sup> were used, the experimental values were underestimated at lower temperatures, and as the temperature increases the true values are overestimated. Vapour densities predicted using the new force field, and the parameters of Geerlings et al.<sup>14</sup> are in good agreement above 430 K, but below this

temperature deviation from the experimental values is around an order of magnitude. This deviation at lower temperatures results in slight underestimation of the critical density. However, compared to other force fields, the new force field gives the best agreement for vapour densities. A similar phenomenon was also observed in several cyclic alkanes, especially in cyclohexane, cyclopentane,<sup>40</sup> and linear alkanes.<sup>18</sup>

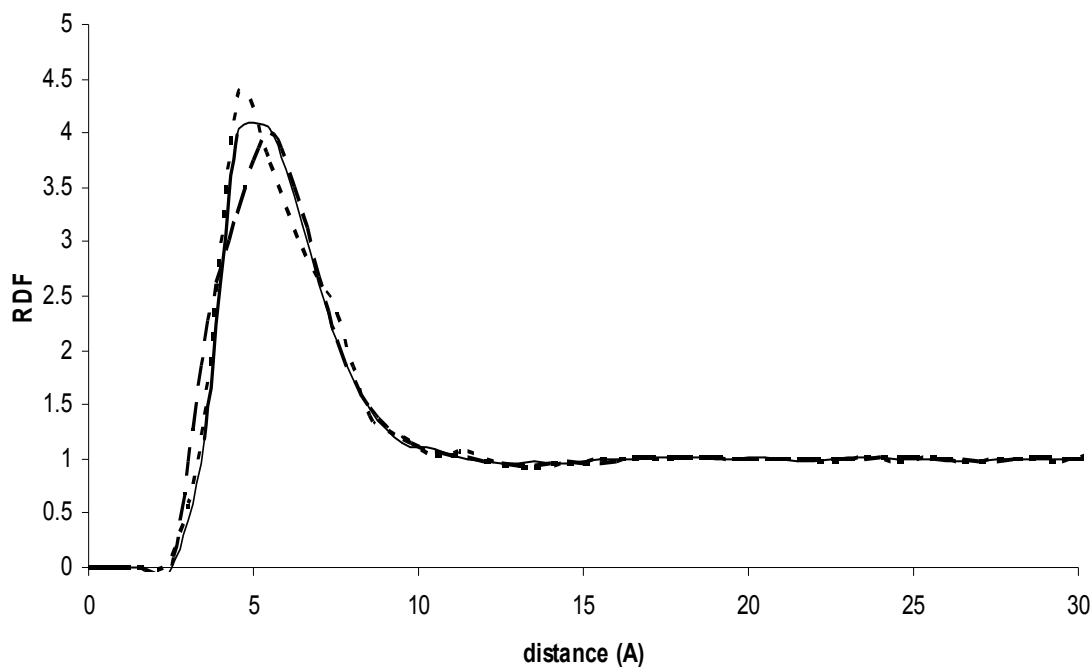


Figure 4.3. Radial distribution functions of O-O (- - -), CH<sub>2</sub>-O (— — —), CH<sub>2</sub>-CH<sub>2</sub> (————) pairs of 1,4-Dioxane molecule in the vapour phase at 298.15 K.

To study the low temperature vapour phase configuration in detail and bring an explanation to the high predicted vapour densities we computed the radial distribution functions of O-O, CH<sub>2</sub>-O, CH<sub>2</sub>-CH<sub>2</sub> pairs of 1,4-Dioxane in the vapour phase at 298.15 K (see Figure 4.3). In all three cases there is a peak around 5 Å, which indicates the possibility of dimers in the vapour phase. When we visually examined the vapour phase configuration snapshots from the simulation we also observed that some 1,4-Dioxane

molecules were close to each other, although most molecules were far away from each other. These dimers present may be a factor in the resulting high vapour densities at lower temperatures. The deviation of predicted vapour densities from the experimental data can be due to other reasons, including the inadequate representation of cyclic molecules with the united-atom approach and the use of Lennard-Jones function.<sup>41</sup>

We calculated the compressibility factors of 1,4-dioxane at nine different temperatures with the new force field (see Table 4.4). Up to about 400 K 1,4-dioxane behaves very much like an ideal gas, but then gradually deviates from this behaviour. After this point, the compressibility factors we computed were in good agreement with the values derived from experimental vapour pressures.

**Table 4.4. Compressibility factors calculated from experimental vapour pressure data and those computed from simulations with new force field. The subscripts denote the statistical uncertainties in the last digit(s) where available.**

Temperature (K)	Experimental	Simulation
298.15	0.994	0.944 <sub>22</sub>
326.51	0.986	0.917 <sub>29</sub>
354.86	0.974	0.929 <sub>51</sub>
383.22	0.950	0.924 <sub>66</sub>
411.58	0.928	0.882 <sub>95</sub>
439.93	0.894	0.897 <sub>78</sub>
468.29	0.854	0.863 <sub>56</sub>
496.64	0.785	0.798 <sub>69</sub>
525.0	0.703	0.716 <sub>57</sub>

To investigate the finite size effects we computed liquid and vapour densities by carrying out the simulations with 300 molecules. The agreement between the densities computed with 180 molecules and 300 molecules is quite convincing (see Figures 4.4 and 4.5), especially the liquid densities give a perfect match. These results provide strong evidence that liquid and vapour densities of 1,4-Dioxane computed using our force field parameters are not sensitive to the number of molecules, at least beyond 180.

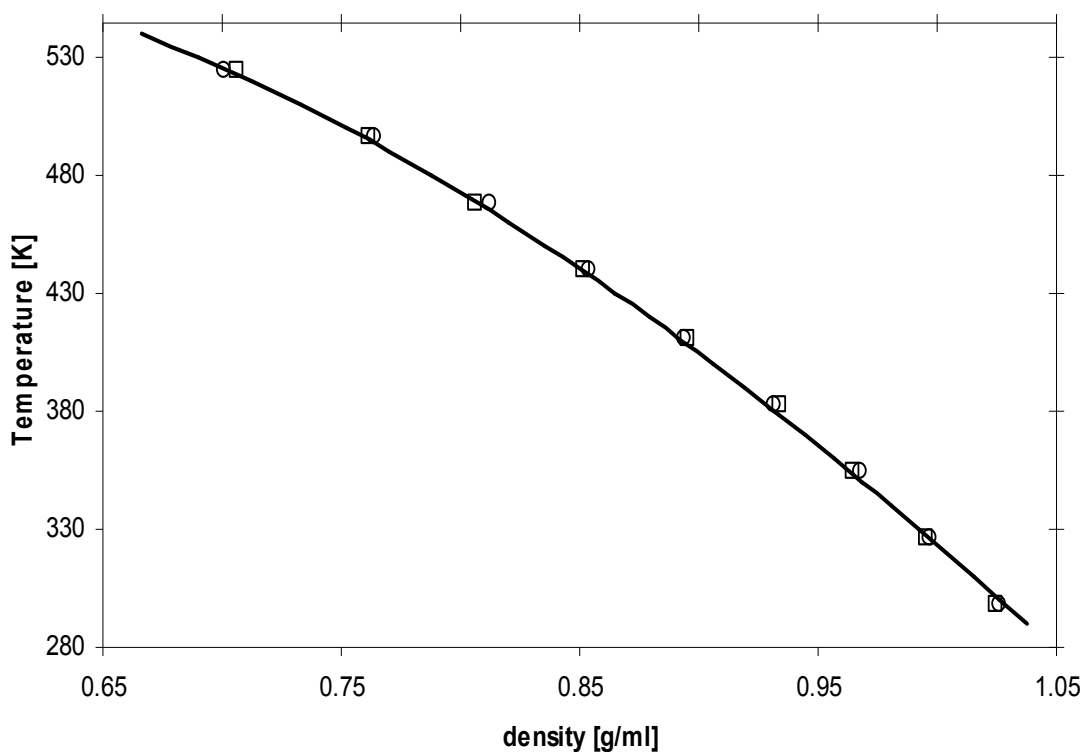


Figure 4.4. Liquid densities of 1,4-Dioxane. New force field 180 molecules (○), New force field 300 molecules (□). Solid line represent the experimental liquid densities.<sup>31</sup>

Finally, we computed the heat of vaporization of 1,4-Dioxane at room temperature and at its boiling temperature by using the vapour pressure approach which is fully described elsewhere.<sup>42</sup> The heat of vaporization of 1,4-Dioxane at room temperature and at its boiling point was computed to be 37.19<sub>73</sub> kJ/mol and 32.65<sub>93</sub>

kJ/mol, respectively. These values are close to the reported experimental values, which are 38.4 kJ/mol and 34.2 kJ/mol<sup>43</sup> at the room temperature and at 1,4-Dioxane's boiling point, respectively.

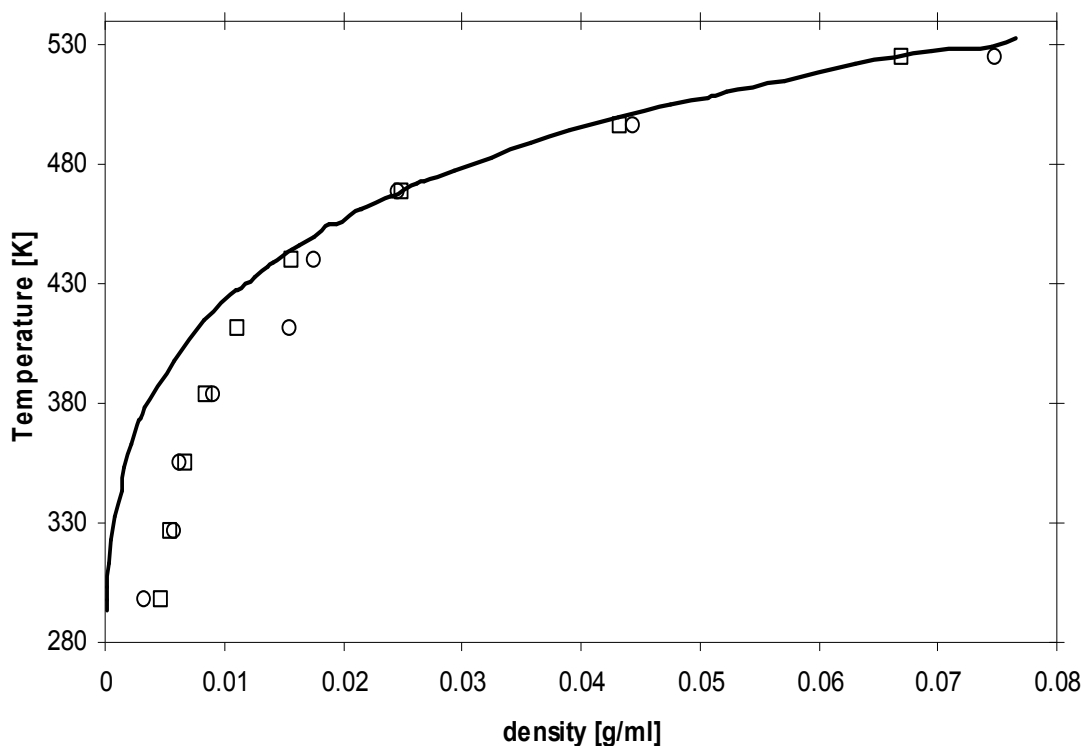


Figure 4.5. Vapour densities of 1,4-Dioxane. New force field 180 molecules ( $\circ$ ), New force field 300 molecules ( $\square$ ). Solid lines represent the vapour densities calculated from the experimental vapour pressures<sup>33</sup> using Pitzer's<sup>34</sup> method.

#### 4.4. Conclusions

We have developed a new force field for 1,4-dioxane, an important industrial solvent which has emerged as a potentially significant threat to human health. Predictions of experimental critical point data and phase behaviour with our new force field outperformed predictions from simulations with other force field parameters available in literature. Liquid densities and the critical temperature were estimated in almost perfect agreement with corresponding experimental data. The critical density was only slightly

underestimated with our new force field. At high temperatures, vapour densities also were predicted satisfactorily, however, at lower temperatures where 1,4-Dioxane behaves like an ideal gas, deviations up to an order of magnitude were observed. Computed heats of vaporization at room temperature and at its boiling point are close to the experimental values.

The primary objective of this section was to develop reliable atom-atom interaction parameters to use in the simulation of the adsorption of 1,4-Dioxane in different adsorbent materials. We validated our new parameters by predicting the experimental phase behaviour, critical temperature, and the critical density. The successful results give us confidence to use the new parameters in our further studies.

## Bibliography

1. US Environmental Protection Agency, Measurement and Monitoring Technologies for the 21st Century, 17th Quarterly Literature Search. October 17, 2005.
2. E.J. Calabrese, E.M. Kenyon. *Air Toxics and Risk Assessment*, Lewis Publishers, Chelsea, MI, 1991.
3. S. Budavari (11th ed.). *The Merck Index, An Encyclopedia of Chemicals, Drugs, and Biologicals*, Ed. Merck and Co. Inc., Rahway, NJ.,1989.
4. National Cancer Institute (NCI). *Bioassay of 1,4-Dioxane for Possible Carcinogenicity*, CAS No. 123-91-1. NCI Carcinogenesis Technical Report Series No. 80. NCI-CG-TR80. National Institutes of Health, Bethesda, MD.,1978.
5. U.S. Environmental Protection Agency. *Integrated Risk Information System (IRIS) on 1,4-Dioxane*, National Center for Environmental Assessment, Office of Research and Development, Washington, DC., 1999.
6. Zenker, M.J.; Borden, R.C.; Barlaz. M.A., *Env. Eng. Sci.* **1990**, 20, 423.
7. Suha, J.H.; Mohsenib. M., *Water Research*, **2004**, 38, 2596.
8. Adams, C.D.; Scanlan, P.A.; Secrist, N.D., *Env. Sci. and Tech.* **1994**, 28, 1812.
9. Kelley, S.L.; Aitchison, E.W.; Deshpande, M.; Schnoor, J.L.; Alvarez. P.J.J., *Water Research* **2001**, 35, 3791.

10. J.C Alonso, J.C. Johnson, P.J. Linton. 1,4-Dioxane—History, regulatory issues, and the potential remedial impacts, 16th Annual International Conference on Contaminated Soils, Sediments, and Water, Amherst, MA, 2000.
11. T.K.G. Mohr. *Solvent Stabilizers: White Paper*, Santa Clara Valley Water District, San Jose, CA. (2001).
12. Luhmer, M.; Stien, M.L.; Reisse, J., *Heterocycles*, **1994**, 37,1041.
13. Luhmer, M.; Reisse, J., *J. Chem. Phys.* **1933**, 98, 1566.
14. Geerlings, J.D.; Varma, C.A.G.O.; van Hemert., M.C. *J. Phys. Chem. B* **2000**, 104, 56.
15. H. Krienke, G. Ahn-Ercan, J.Barthel, Alkali metal halide solutions in 1,4-dioxane–water mixtures. A Monte Carlo simulation study, *J. Mol. Liq.*, **109**, 115 (2004).
16. Giaya, A.; Thompson. R.W., *J. Chem. Phys.*, **2002**, 117, 3464.
17. Briggs, J.M; Matsui, T.; Jorgensen, W.L., *J.Comp. Chem* **1990**, 11, 958.
18. Martin, M.G.; Siepmann, J.I., *J.Phys. Chem. B* **1998**, 102, 2569.
19. Martin, M.G.; Siepmann, J.I., *J.Phys. Chem. B* **1999**, 103, 4508.
20. Chen, B.; Potoff, J.J.; Siepmann. J.I., *J.Phys. Chem. B* **2001**, 105, 3093.
21. Stubbs, J.M.; Potoff, J.J.; Siepmann, J.I., *J.Phys. Chem. B* **2004**, 108, 17596.

22. Cornell, W.D.; Cieplak, P.; Bayly, C.I.; Gould, I.R.; Merz Jr., K.M.; Ferguson, D.M.; Spellmeyer, D.C. ; Fox, T.; Caldwell, J.W.; Kollman, P.A., *J. Am. Chem. Soc.*, **1995**, 117, 5179.
23. <http://towhee.sourceforge.net>
24. Panagiotopoulos, A. Z., *Mol. Phys.*, **1987**, 61, 813.
25. Panagiotopoulos, A. Z.; Quirke, N.; Stapleton, M.; Tildesley, D.J., *Mol. Phys.*, **1998**, 63, 527.
26. Smit, B.; Desmedt, P.H.; Frenkel. D., *Mol. Phys.*, **1989**, 68, 931.
27. Martin, M.G.; Thompson, A.P., *Fluid Phase Equilibria*, **2004**, 217, 105.
28. Martin, M.G.; Frischknecht, A.L., *Mol. Phys.* submitted.
29. J.S. Rowlinson, B. Widom. *Molecular Theory of Capillarity*, Oxford University Press New York, 1989.
30. J.S. Rowlinson, F.L. Swinton (3<sup>rd</sup> Ed.). *Liquids and Liquid Mixtures*, Butterworth London, 1982.
31. C.L. Yaws. *Yaws' Handbook of Thermodynamic and Physical Properties of Chemical Compounds*, Knovel, 2003.
32. Hojendahl., K *Mat.-Fys. Medd. - K. Dan. Vidensk. Selsk.* **1946**, 24, 1.
33. Vinson, C.G.; Martin., Jr, J.J., *J. Chem. Eng. Data*, **1963**, 8, 74.

34. Pitzer, K.S.; Kippman, D.Z.; Curl, R.F.; Huggins, Jr., C. M.; Petersen, D. E., *J. the Am. Chem. Soc.* **1995**, 77, 3433.
35. Kobe, K.A.; Ravicz, A.E.; Vohra, S.P., *Ind. & Eng. Chem.* **1956**, 1, 50.
36. Glaser, F.; Ruland, H., *Chem. Ing. Techn.*, **1957**, 29, 772.
37. Cristou, G.; Young, C.L.; Svejda, P., *Fluid Phase Equilibria*, **1991**, 67, 45.
38. Fox, J.P.; Rooy, V.; Bates, S.P., *Mic. Mes. Ma.*, **2004**, 69, 9.
39. M.P.Allen, D.J. Tildesley, *Computer Simulation of Liquids*; Clarendon Press, Oxford, 1989.
40. Lee, J.S.; Wick, C.D.; Stubbs, J.M.; Siepmann, J.I, *Mol. Phys.*, **2005**, 103, 99.
41. Chen, B.; Martin, M.G.; Siepmann, J.I., *J. Phys. Chem. B*, **1998**, 102, 2578.
42. Martin, M.G.; Biddu, M.J., *Fluid Phase Equilibria*, **2005**, 236, 53.
43. J.A Dean (Ed), *Lange's Handbook of Chemistry*, McGraw-Hill, (1999)

## **5. MOLECULAR SIMULATION of LIQUID PHASE ADSORPTION of MTBE and 1,4-DIOXANE from WATER**

### **5.1. Introduction**

Until now we have studied the adsorption of a single component from the gas phase with Monte Carlo simulations. Nevertheless, the scope of this study also covers the adsorption of binary systems as we are dealing with contaminants in water. In this case Grand Canonical Monte Carlo simulations can again be useful. The first task is to compute the chemical potential of the species in liquid phase. Direct measurement of the chemical potential of a species in liquid phase with Widom's insertion method<sup>1</sup> is difficult due to the difficulty of inserting a molecule in to a dense phase. However, this problem can be overcome by computing the chemical potential of the species in the gas phase in equilibrium with the liquid phase since the chemical potential of the species in both phases would be equal in the case of a thermodynamic equilibrium. This approach is illustrated in Figure 5.1. Consider a system where a binary mixture is in thermodynamic equilibrium with its sorbed phase in a porous material and its gaseous phase. The gaseous phase would be also in thermodynamic equilibrium with the sorbed phase, resulting in a three phase equilibrium where the chemical potential of the species are equal to each other regardless of what phase they are in. Starting from this principle, at a certain temperature using an Equation of State (EOS), one can compute the fugacity of the species in the gas phase for a known concentration of binary mixture in the liquid phase. Once the fugacity of the species in the gas phase is known chemical potential of the species can be computed using Widom's method. After that adsorption isotherms can be obtained with GCMC simulations in a similar way to the single component adsorption.

This approach was successfully applied by Chempath et.al.<sup>2,3</sup> for the adsorption of binary liquid mixtures of alkanes<sup>2</sup> and binary liquid mixtures of aromatics<sup>3</sup> in silicalite.

In this section we report adsorption isotherms of MTBE and 1,4-Dioxane from water at room temperature obtained with GCMC simulations. The concentrations of MTBE and 1,4-Dioxane in water were varied between 10 $\mu$ g/L to 1mg/L.

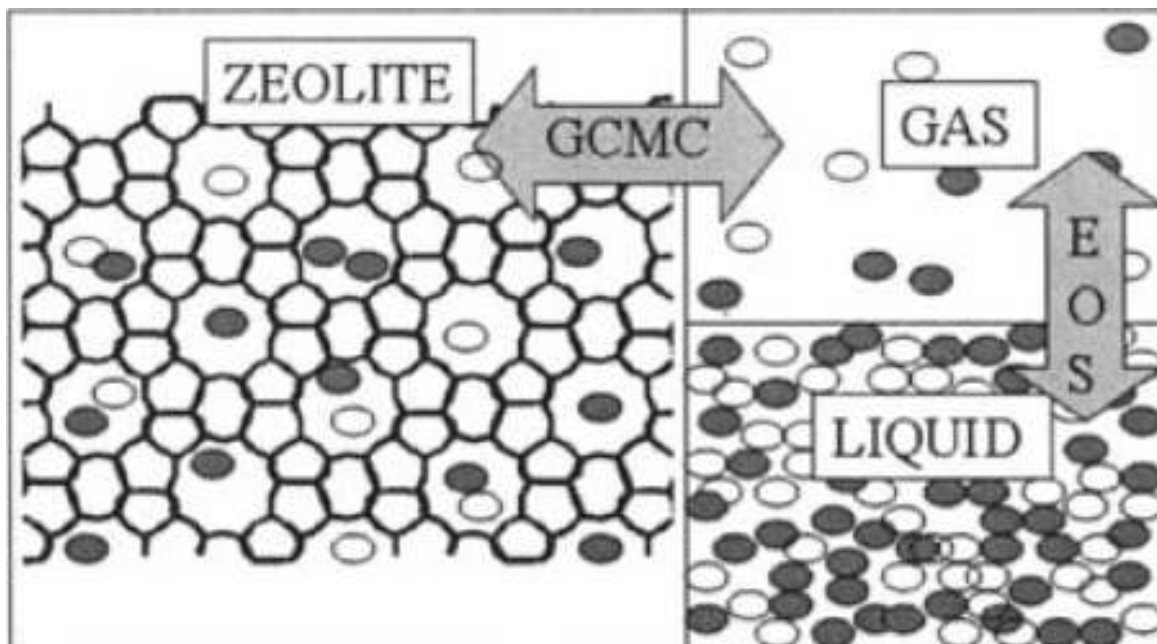


Figure 5.1. Binary-mixture three phase equilibrium. Equilibrium between liquid and gas can be calculated with an EOS model. GCMC simulations can calculate equilibrium between gas and zeolite. (from reference 3)

## 5.2. Models and Methods

### 5.2.1. Silicalite, Water, MTBE and 1,4-Dioxane Models.

Unitcell structure of orthorhombic (*Pnma*) silicalite was taken from the work of Artioli et al.<sup>4</sup> Two unit cells were used resulting in a simulation box with dimensions of  $a=20.0511 \text{ \AA}$ ,  $b=19.87570 \text{ \AA}$ ,  $c=26.73640 \text{ \AA}$ . No defects were considered and positions of all silicalite atoms were fixed. The water molecule was represented by the famous SPC-E water model<sup>5</sup> which is a rigid structure. MTBE was modeled using the TraPPE-UA<sup>6,20-22</sup>

force field as it was explained in detail in Chapter 3. The model developed in Chapter 4 was used to represent the 1,4-Dioxane molecule<sup>7</sup>.

### 5.2.2. Force Field.

We used a pairwise-additive potential which is in the form of 12-6 Lennard-Jones (LJ) plus columbic potential to compute the site-site nonbonded interactions:

$$V_{ij} = 4\varepsilon_{ij} \left[ \left( \frac{\sigma_{ij}}{r_{ij}} \right)^{12} - \left( \frac{\sigma_{ij}}{r_{ij}} \right)^6 \right] + \frac{q_i q_j}{4\varepsilon_0 r_{ij}} \quad (1)$$

where  $i$  and  $j$  are atoms of water, silicalite lattice and defects, and  $r_{ij}$  is the distance between atoms  $i$  and  $j$ .  $\varepsilon_{ij}$  and  $\sigma_{ij}$  are LJ well depth and diameter, respectively.  $q_i$  and  $q_j$  are the partial charges of the interacting sites.

The force field covers two types of interactions; the interactions between sorbate molecules, and the interactions between silicalite and sorbate molecules. The first one was derived by using the Lorentz-Berthelot mixing rules between the atoms of water, MTBE and 1,4-Dioxane. MTBE-MTBE, 1,4-Dioxane-1,4-Dioxane and water-water interaction parameters were already given in Chapters 3,4, and 2, respectively.

For the interactions between water molecule and silicalite atoms we used the parameters derived in Chapter 2 here the silanol effects were included in the oxygen atom of silicalite. To derive the interaction parameters between the atoms of silicalite, and atoms of MTBE and 1,4-Dioxane, single component experimental gas phase adsorption isotherms were used.<sup>8</sup> To do this we used the same partial charges for silicon and oxygen atoms of silicalite that were used in the previous chapters which were taken from the work of Jaramillo et.al.<sup>9</sup> and adjusted the LJ parameters of the oxygen atom of the silicalite to fit the available experimental adsorption isotherms in a series of GCMC simulations. As

we explained previously silicon atom of silicalite interacted with the atoms of sorbate molecules only through the electrostatic potential. Here we only list the interaction parameters between silicalite atoms and the atoms of sorbate molecules in Table 5.1.

**Table 5.1. Force field parameters**

Lennard-Jones			Columbic	
Interacting Sites	$\sigma$ (Å)	$\epsilon$ (K)	Sites	q(e)
OZ – OW	4.24	110.0	Si	2.050
OZ – C	4.26	8.66	OZ	-1.025
OZ – O	2.76	90.83	C	0.25
OZ – CH <sub>3</sub>	3.235	121.24	O	-0.5
C - OW	4.4828	6.2529	CH <sub>3</sub>	0.0
O - OW	2.9828	65.581	CH <sub>2c</sub>	0.25
CH <sub>3</sub> - OW	3.4578	87.54	Oc	-0.5
OZ – CH <sub>2c</sub>	3.245	69.4421	OW	-0.8476
OZ - Oc	2.72	95.9792	HW	0.4238
CH <sub>2c</sub> – OW	3.5078	63.3364		
Oc – OW	2.9828	87.5403		

OZ: Oxygen of silicalite, OW: Oxygen of water, HW: Hydrogen of water, C: Carbon of MTBE, O: Oxygen of MTBE, CH<sub>3</sub>: Methyl united atom of MTBE, CH<sub>2c</sub>: Methylene united atom of 1,4-Dioxane, Oc: Oxygen of 1,4-Dioxane

### 5.2.3. Fugacities of the Species in the Gas Phase.

We used the commercial ASPEN software to calculate the fugacities of the species in gas phase. As stated before we considered two systems, MTBE-Water and 1,4-Dioxane-Water. Van-Laar EOS was used for the first one and NRTL EOS for the second one. The selection of the EOS used was based on the availability of EOS parameters for

the molecules of interest in the database of the software. Within the range of previously specified concentrations of MTBE and 1,4-Dioxane in liquid water, the fugacities of the each species were computed for the gas phase which is in equilibrium with the liquid phase.

#### **5.2.4. Chemical Potential of Species in the Gas Phase.**

The chemical potentials of species in the gas phase were computed by Widom's insertion method in a series of NPT Ensemble Monte Carlo<sup>10</sup> simulations. In this ensemble pressure, temperature and number of molecules are fixed. A simulation box containing 100 molecules were setup for the molecule we wanted to compute its chemical potential. Temperature and pressure were set to 298.15 K and to the fugacity of the molecule of interest calculated from the EOS, respectively, in the case of binary mixtures. These simulations were also performed to compute the chemical potential of MTBE and 1,4-Dioxane at the temperature and pressure of the experimental data we used to fit the MTBE–Silicalite and 1,4-Dioxane-Silicalite interaction parameters. Translation and rotation moves of MTBE, 1,4-Dioxane and water molecules and volume change move of the simulation box were sampled with probabilities 50%, 45% and 5%, respectively. At each state point the system were equilibrated for 10000 and a 10000 cycle production run followed the equilibration in which the chemical potential was measured by widom insertion method at every cycle. A cycle is equal to  $N$  Monte Carlo moves, where  $N$  is the number of molecules in the system. The statistical errors, which were computed by dividing the production run in to five blocks, for the measured chemical potentials were less than % 1 in all cases.

### 5.2.5. Simulation of the Adsorption Isotherms.

Adsorption isotherms were computed in the Grand Canonical ( $\mu$ VT)<sup>10</sup> ensemble using Configurational Bias Monte Carlo (CB-GCMC)<sup>11-14</sup> simulations with MF-CPN<sup>15</sup> strategy. MF-CPN is a combined strategy for insertion and regrowth moves to increase their acceptance rates. Insertion/deletion, translation, rotation and regrowth moves were sampled on the sorbate molecules with the probabilities of %30, %30, %30, %10. In the case of binary systems these probabilities were applied equivalently to each molecule. A cutoff distance of 9.5 Å was used with periodic boundary conditions applied in three dimensions. Columbic interactions were handled by the Ewald Sum method.<sup>16</sup> Each run lasted for 5 million steps in order to equilibrate the system, followed by 5 million steps for the data acquisition.

In all simulations Towhee Monte Carlo simulation code was used.<sup>17</sup>

## 5.3. Results and Discussion

### 5.3.1. Adsorption of MTBE and 1,4-Dioxane from the Gas Phase.

In Figures 5.2, 5.3, and 5.4 adsorption isotherms of MTBE in silicalite obtained from GCMC simulations at 425.15 K, 448.15 K and 473.15 K, respectively, are compared with isotherms from experiments<sup>24</sup>. The agreement is reasonable considering that we only varied the LJ parameters of silicalite oxygen to obtain the fit. The resulting LJ parameters were  $\sigma = 2.72$  Å and  $\epsilon = 150$  K. In Figure 5.5 adsorption isotherm of MTBE in silicalite at 298.15 K is shown, which is obtained by using the LJ parameters fitted to the experimental data. It is not surprising to see that with decreasing temperature amount of MTBE adsorbed increased.

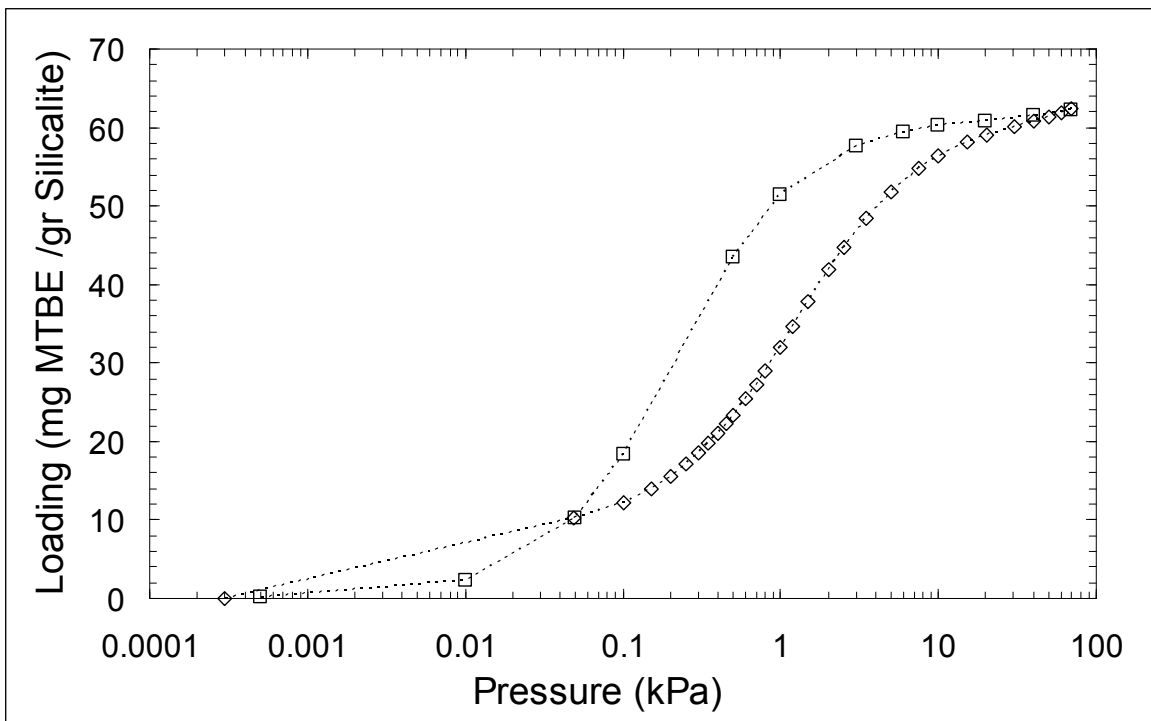


Figure 5.2. Gas phase pure MTBE adsorption isotherms in silicalite: ( $\diamond$ ) experiment<sup>23</sup> at 425.15 K, ( $\square$ ) simulation at 425.15 K.

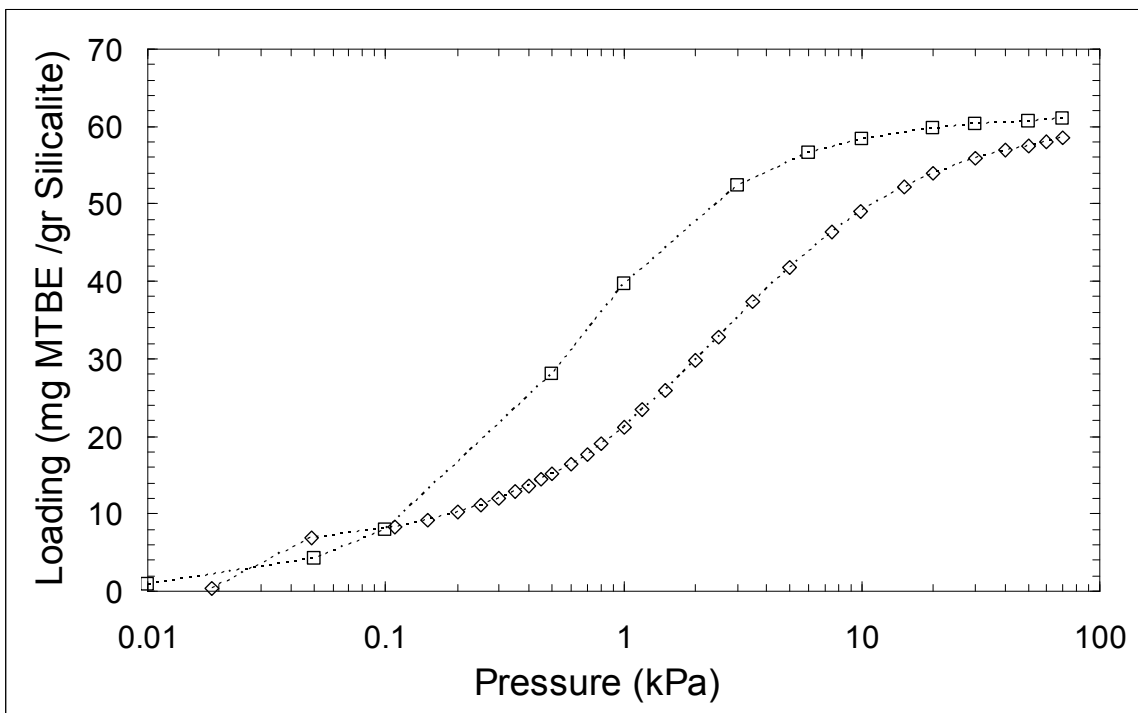


Figure 5.3. Gas phase pure MTBE adsorption isotherms in silicalite: ( $\diamond$ ) experiment<sup>23</sup> at 448.15 K, ( $\square$ ) simulation 448.15 K.

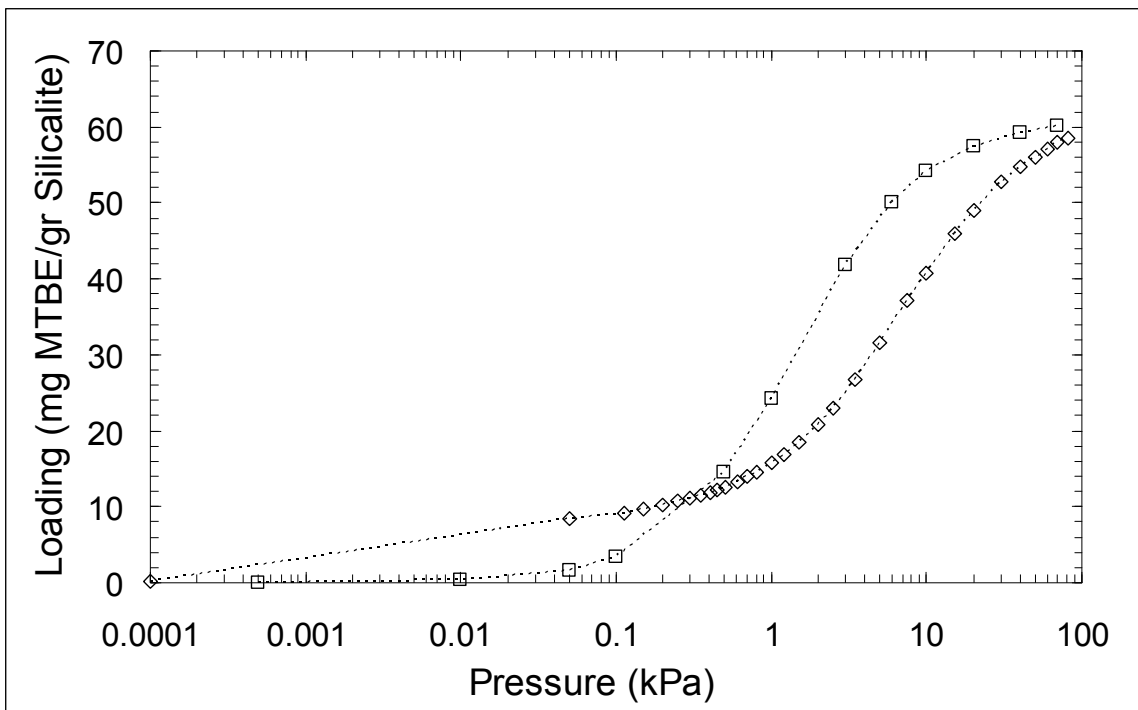


Figure 5.4. Gas phase pure MTBE adsorption isotherms in silicalite: ( $\diamond$ ) experiment<sup>23</sup> at 473.15 K, ( $\square$ ) simulation at 473.15 K.

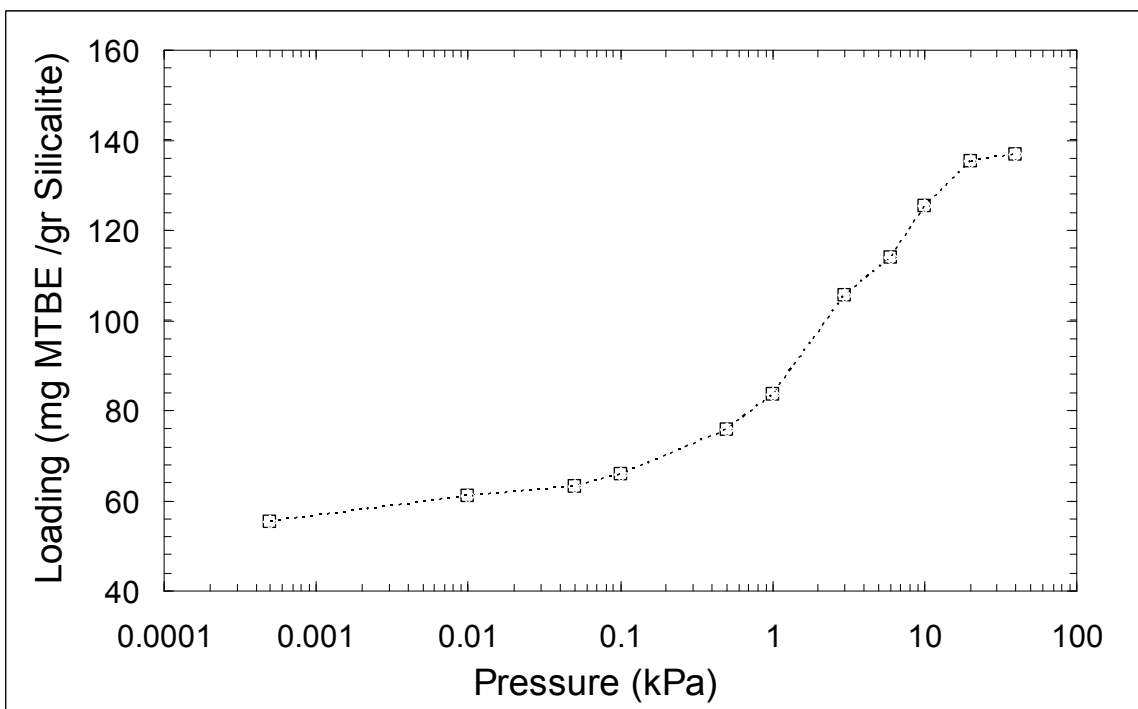


Figure 5.5. Gas phase pure MTBE adsorption isotherm in silicalite:( $\square$ ) simulation at 298.15 K.

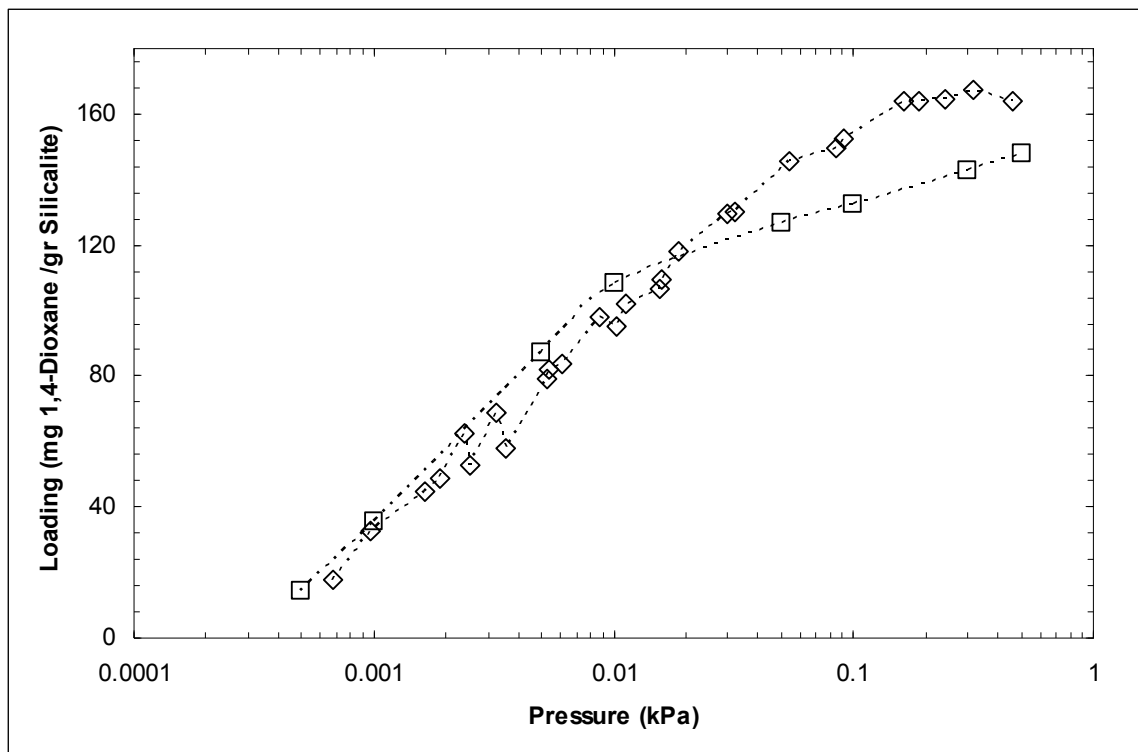


Figure 5.6. Gas phase pure 1,4-Dioxane adsorption isotherms in silicalite: (◇) experiment<sup>8</sup> at 298.15 K, (□) simulation at 298.15 K.

In Figure 5.6 adsorption isotherm of 1,4-Dioxane in silicalite obtained from GCMC simulations at 298.15 K is given in comparison with the isotherm obtained from experiment at the same temperature. The agreement between simulation results and experimental data at lower pressures is good. On the other hand, at higher pressures the amount of 1,4-Dioxane adsorbed is underestimated by the simulation. Lowering  $\sigma$ , which is the size parameter, of silicalite oxygen did not help to improve the fit around this region suggesting that adjustment of partial charges on silicalite or 1,4-Dioxane is required. However, this would have caused other problems considering. For instance, in the case of binary mixture of 1,4-Dioxane and Water, changing partial charges on silicalite atoms would effect the agreement of simulated water adsorption isotherms with experiments we obtained in Chapter 2. Considering that we are interested in very low

concentrations of 1,4-Dioxane we decided that the agreement at low pressure region is sufficient. The fitted LJ parameters of silicalite oxygen for its interaction with 1,4-Dioxane were  $\sigma = 2.64 \text{ \AA}$  and  $\varepsilon = 94 \text{ K}$ .

### **5.3.2. Adsorption of MTBE and 1,4-Dioxane from Water.**

In the previous section we derived the interaction parameters of silicalite oxygen with MTBE and 1,4-Dioxane by fitting the parameters to the available experimental data. By using these parameters we simulated the adsorption of MTBE and 1,4-Dioxane from water at 298.15 K in silicalite. In Figure 5.7 adsorption isotherm of MTBE from water in silicalite obtained from GCMC simulations is given in comparison with the experimental isotherm. Apparently, simulated isotherm underestimates the experimental isotherm and the difference is large. As an attempt to reproduce the experimental isotherm with simulations we increased  $\varepsilon$  of silicalite oxygen incrementally and simulated the isotherms again. When  $\varepsilon$  reached to 260 K a good agreement was obtained with the experimental data. This new isotherm is also shown in Figure 5.6. The main difference between two cases, ( $\varepsilon = 150 \text{ K}$  and  $\varepsilon = 260 \text{ K}$ ) besides the amount of MTBE adsorbed, is the presence of water molecules. In the first case water molecules were present in silicalite with MTBE even at high MTBE concentrations. On the other hand in the second case, except the small amount of water adsorbed at lower concentrations of MTBE almost no water molecules were observed in silicalite. In short, for the MTBE molecules to be adsorbed water molecules had to be ousted from silicalite.

In Figure 5.8 we present the isotherm of 1,4-Dioxane adsorption from water in silicalite at 298.15 K obtained from GCMC simulations. Unfortunately there is no experimental data to compare with results from our simulations. However, simulation of

1,4-Dioxane adsorption from water depicts a similar behavior with the simulation of MTBE adsorption from water. Although there is no experimental data to compare we can say that the amount of 1,4-Dioxane adsorbed from water is very low. Here we again observed significant amount of water presence in silicalite pores.

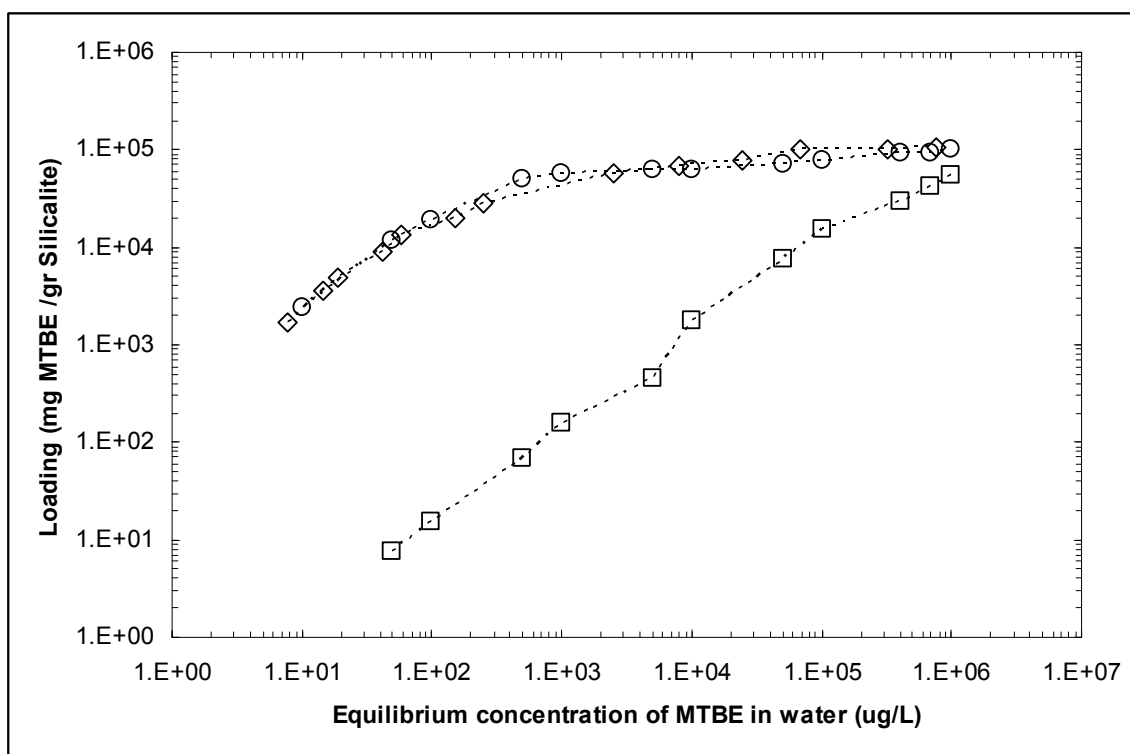


Figure 5.7. Isotherms of MTBE adsorption from water in silicalite at 298.15 K: ( $\diamond$ ) experiment<sup>24</sup>, ( $\square$ ) simulation (OZ  $\varepsilon = 150$  K), ( $\circ$ ) simulation, (OZ  $\varepsilon = 260$  K)

Although we were able to obtain reasonable agreement between simulated and experimental isotherms of pure MTBE and 1,4-Dioxane adsorption in silicalite, simulations of the adsorption of their binary mixtures with water did not yield promising results. There can be several reasons for this. First of all the three step procedure to obtain the adsorption isotherms in the case of binary mixtures; 1) obtaining gas phase fugacities, 2) measuring the chemical potential of species in the gas phase and 3) the adsorption simulations each introduce statistical errors. These statistical errors can be significant

considering the extremely low concentrations of MTBE and 1,4-Dioxane in water. Especially in the first step where an EOS is used to calculate the fugacities, ability of the EOS to predict the gas phase composition and fugacities for such very small concentrations is questionable.

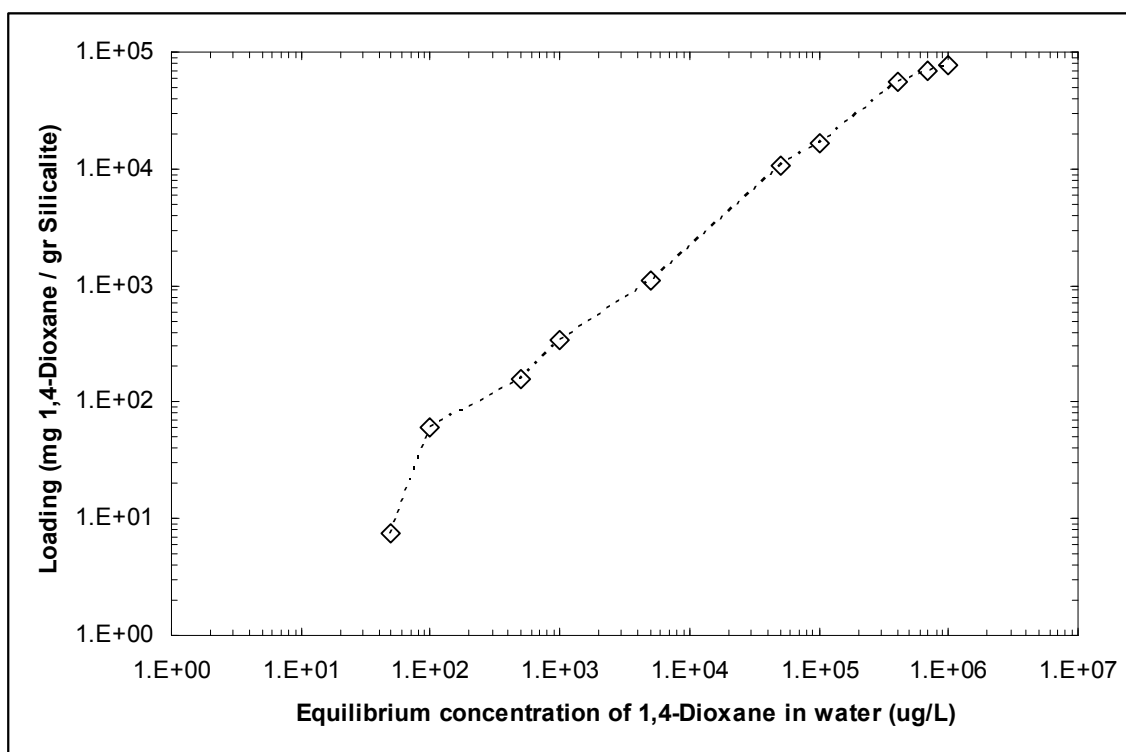


Figure 5.8. Isotherm of 1,4-Dioxane adsorption from water in silicalite: ( $\diamond$ ) simulation at 298.15 K.

Another reason for the unsuccessful simulation results might be due to the interaction parameters of water-MTBE and water-1,4-Dioxane. We used Lorentz-Berthelot mixing rules to derive the LJ parameters between the atoms of these molecules. The discussion of the validity of Lorentz-Berthelot mixing rules is beyond the scope of this text, however, these mixing rules are widely used at least to get an initial estimate to derive the LJ parameters between two unlike atoms. On the other hand, it is not difficult to claim that the LJ parameters obtained by Lorentz-Berthelot mixing rules are far from

being optimized due to the observation that water molecules had to be ousted from the pores of silicalite for MTBE molecules to be adsorbed. With these interaction parameters MTBE and 1,4-Dioxane did not want to be present with water together in the pores, despite the fact that they are known to be highly soluble in water<sup>18,19</sup> suggesting that the LJ parameters derived from Lorentz-Berthelot mixing rules do not represent the water-MTBE and water-1,4-Dioxane interactions correctly.

#### **5.4. Conclusions**

We performed GCMC simulations to obtain the isotherms of MTBE and 1,4-Dioxane adsorption from water in silicalite. First we optimized the interaction parameters between the atoms of silicalite and the atoms of MTBE and 1,4-Dioxane so that pure component adsorption can be predicted. This optimization yielded a reasonable agreement with available experimental data. Adsorption of water in silicalite was already studied and optimization of the interaction parameters was achieved in Chapter 2. Using these optimized parameters we simulated the adsorption of MTBE and 1,4-Dioxane from water in silicalite. Despite the agreement of simulated and experimental isotherms of pure components, simulated isotherm of MTBE adsorption from water in silicalite underestimated the experimental isotherm significantly. Only after the energy parameter,  $\epsilon$ , was increased to 260 K a good agreement was obtained. Basically, the MTBE molecules were adsorbed only after water molecules were ousted from silicalite. This phenomenon was also observed in the adsorption of TCE (Trichloroethylene) in Zeolite Y.<sup>25</sup>

Although we were unable to find experimental data for the adsorption of 1,4-Dioxane from water in silicalite, the simulated isotherm showed a similar behavior to MTBE adsorption with very little amount of 1,4-Dioxane adsorbed.

## **Bibliography**

1. Widom, B., *J. Chem. Phys.* **1963**, 39, 2808.
2. Chempath, S.; Denayer, J.F.M.; De Meyer, K.M.A.; Baron, G.V.; Snurr, R.Q., *Langmuir*, **2004**, 20, 150.
3. Chempath, S.; Snurr, R.Q.; Low, J.J., *AICHE Journal*, **2004**, 50, 463.
4. Artioli, G.; Lamberti, C.; Marra, G.L.; *Acta. Cryst. B* **2000**, 56, 2.
5. Berendsen, H.J.C.; Grigera, J.R.; Straatsma, T.P., *J. Phys. Chem.* **1987**, 91, 6269.
6. Martin, M.G.; Siepmann, J.I. *J. Phys. Chem. B* **1998**, 102, 2569.
7. Yazaydin, A.O.; Thompson, R.W., *Mol. Sim.* **2006**, 32, 657.
8. Moneyron, P.; Manero, M.; Foussard, J., *Environ. Eng. Sci.* **2003**, 37, 2410.
9. Jaramillo, E.; Grey, C. P.; Auerbach, S. M. *J. Phys. Chem. B* **2001**, 105, 12319.
10. Frenkel, D.; Smit, B., *Understanding Molecular Simulation from Algorithms to Applications*; 2<sup>nd</sup> ed., Academic Press: SanDiego, **2002**.
11. Siepmann, J.I., *Mol. Phys.* **1990**, 70, 1145.
12. Siepmann, J.I.; Frenkel, D., *Mol. Phys.* **1992**, 75, 59.

13. Frenkel, D.; Mooji, G.C.A.M.; Smit, B., *J. Phys.: Condens. Matter*, **1992**, 3053.
14. Laso, M.; de Pablo, J.J.; Suter, U.W., *J. Chem. Phys.* **1992**, 97, 2817.
15. Martin, M.G.; Frischknecht, A.L., *Mol. Phys.* **2006**, 104, 2439.
16. Ewald, P.P., *Ann. Phys.* **1921**, 64, 253.
17. <http://towhee.sourceforge.net>
18. Wilhelm, M.J.; Adams, D.D; Curtis, J.G.; Middlebrooks, J., *J. Env. Eng.* **2002**, 1, 813.
19. Zenker, J.M.; Borden, R.C.; Barlaz, M.A., *Env. Eng. Sci.* **2003**, 20, 423.
20. Martin, M.G.; Siepmann, J.I. *J. Phys. Chem. B* **1999**, 103, 4508.
21. Chen, B.; Potoff, J.J.; Siepmann, J.I. *J. Phys. Chem. B* **2001** 105, 3093.
22. Stubbs, J.M.; Potoff, J.J.; Siepmann, J.I. *J. Phys. Chem. B* **2004** 108, 17596
23. Erdem-Şenatalar, A.; Department of Chemical Engineering, Istanbul Technical University, Istanbul, TURKEY. Personal communication, December 22, 2006.
24. Erdem-Şenatalar, A.; Bergendahl, J.A.; Giaya, A.; Thompson, R.W. *Environ. Eng. Sci.* **2004**, 21, 722
25. Giaya, A., (2001). Ph.D. Dissertation Dept. of Chemical Engineering, Worcester, MA: Worcester Polytechnic Institute.

## 6. COMPUTING BINDING ENERGIES and HENRY'S CONSTANTS from MOLECULAR SIMULATIONS

### 6.1. Introduction

Until this chapter we have focused on obtaining adsorption isotherms of MTBE, 1,4-Dioxane and water in different zeolites. Isotherms give important information about the characteristics of an adsorbent-sorbate relation over a broad range of pressure or concentration. An adsorption isotherm usually has usually two typical regions. In the lower pressure/concentration region a rapid increase in the amount of the sorbate molecule is usually observed which eventually reaches to a limiting capacity in the second region by increasing pressure/concentration. The behavior of the isotherm in the first region is closely related with the affinity between the adsorbent and sorbate molecule. Considering that this study is focused on contaminants which are present in water or air in very small amounts, investigating the affinity between an adsorbent and a sorbate molecule can be more convenient instead of obtaining the full isotherm.

Affinity between an adsorbent and a sorbate molecule can be expressed in terms of the binding energy between two of them. This binding energy can be computed by inserting a sorbate molecule in to the adsorbent many times in a Monte Carlo simulation and taking the average interaction energy between the sorbate molecule and adsorbent. Once binding energy is computed this can be used to calculate Henry's constant,<sup>1</sup> which carries industrial importance for adsorption processes.

$$H = \frac{\left\langle \exp\left(-\frac{U}{k_B T}\right) \right\rangle}{k_B T} \quad (1)$$

In the above equation  $H$  is Henry's constant,  $U$  is the binding energy computed during the insertion of the sorbate molecule, and  $k_B$  is Boltzmann's constant. This method was used to compute the Henry's constant of several alkanes in silicalite<sup>2,3</sup> and water in activated carbon.<sup>1</sup>

In this chapter we utilized the approach summarized above to compute the binding energies and Henry's constants for 1,1-Dichloroethylene (1,1-DCE) and Perfluorooctanoic Acid (PFOA) in all silica silicalite, mordenite, Zeolite-Beta, and Zeolite-Y.

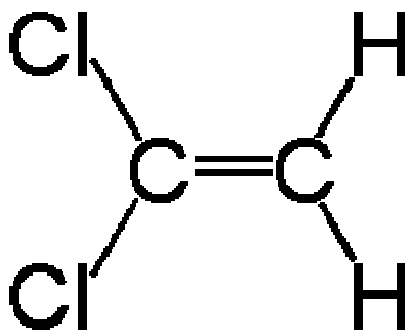


Figure 6.1. 1,1-Dichloroethylene

1,1-DCE ( $C_2H_2Cl_2$ ) is used in the production polyvinylidene chloride copolymers which are used in the production of flexible films for food packaging. It is also used as an intermediate for organic chemical synthesis.<sup>4</sup> Animals studied has showed that 1,1-DCE has a toxic effect on kidneys, liver, CNS and lungs.<sup>4-6</sup> EPA considers 1,1-DCE to be a possible human carcinogen.<sup>7</sup> PFOA ( $C_8HF_{15}O_2$ ) is an industrial surfactant. It is a fully fluorinated carboxylic acid and most commonly used for processing polytetrafluoroethylene PTFE. The durability of PFOA prevents it from breaking down once in the environment, leading to widespread buildup and bioaccumulation in food

chains. Traces of PFOA-family chemicals can now be found in the blood of nearly all Americans and in the environment worldwide.<sup>8</sup> EPA has identified potential human health concerns from exposure to PFOA and its salts.<sup>9</sup>

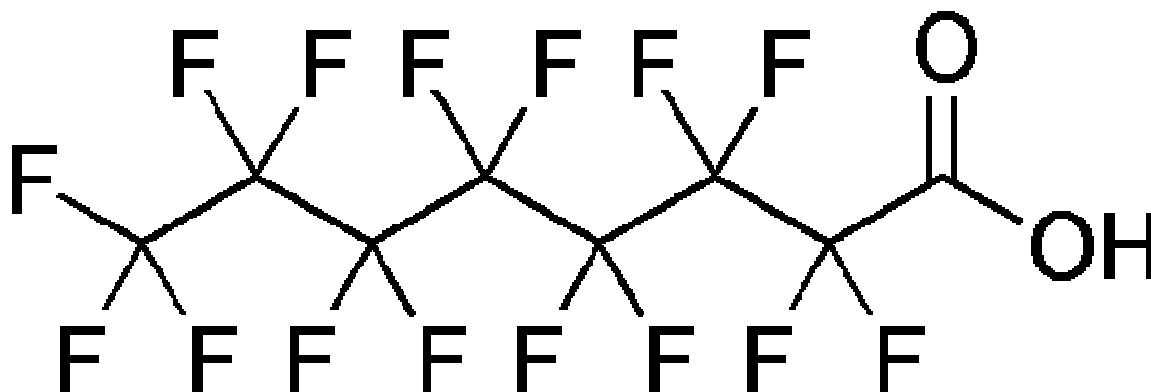


Figure 6.2. Perfluorooctanoic Acid

We also computed the binding energies and Henry's constant for water and 1,4-Dioxane in activated carbon possessing different surface groups to investigate why activated carbon is ineffective to remove 1,4-Dioxane from water.<sup>10</sup>

## 6.2. Models and Methods

### 6.2.1. Zeolite, Activated Carbon, PFOA, 1,1-DCE, 1,4-Dioxane and Water Models

Unitcell structures of silicalite, mordenite, zeolite beta, and zeolite Y were taken from the works of Artioli et al.<sup>11</sup>, Gramlich<sup>12</sup>, Newsam et al.<sup>13</sup>, and Hriljac et. al.<sup>14</sup> respectively. . For simulations in silicalite two unitcells, in mordenite and zeolite beta four unitcells were used and in zeolite-Y we used a single unitcell. Final simulations box dimensions for silicalite were  $a=20.0511 \text{ \AA}$ ,  $b=19.87570 \text{ \AA}$ ,  $c=26.73640 \text{ \AA}$ , for mordenite were  $a=18.011 \text{ \AA}$ ,  $b=20.53 \text{ \AA}$ ,  $c=30.112 \text{ \AA}$ , for zeolite beta were

$a=25.32278 \text{ \AA}$ ,  $b=25.32278 \text{ \AA}$ ,  $c=26.40612 \text{ \AA}$ , and for zeolite-Y were  $a=24.2576 \text{ \AA}$ ,  $b=24.2576 \text{ \AA}$ ,  $c=24.2576 \text{ \AA}$ .

The activated carbon pore was modeled with two graphite plates. Each plate has three layers of carbon sheets. Plate dimensions were of  $a=24.56 \text{ \AA}$ ,  $b=24.56 \text{ \AA}$ , and these plates were separated with a distance of  $c=12.0 \text{ \AA}$ . Figure 6.3 shows a representation of the activated carbon pore modeled.

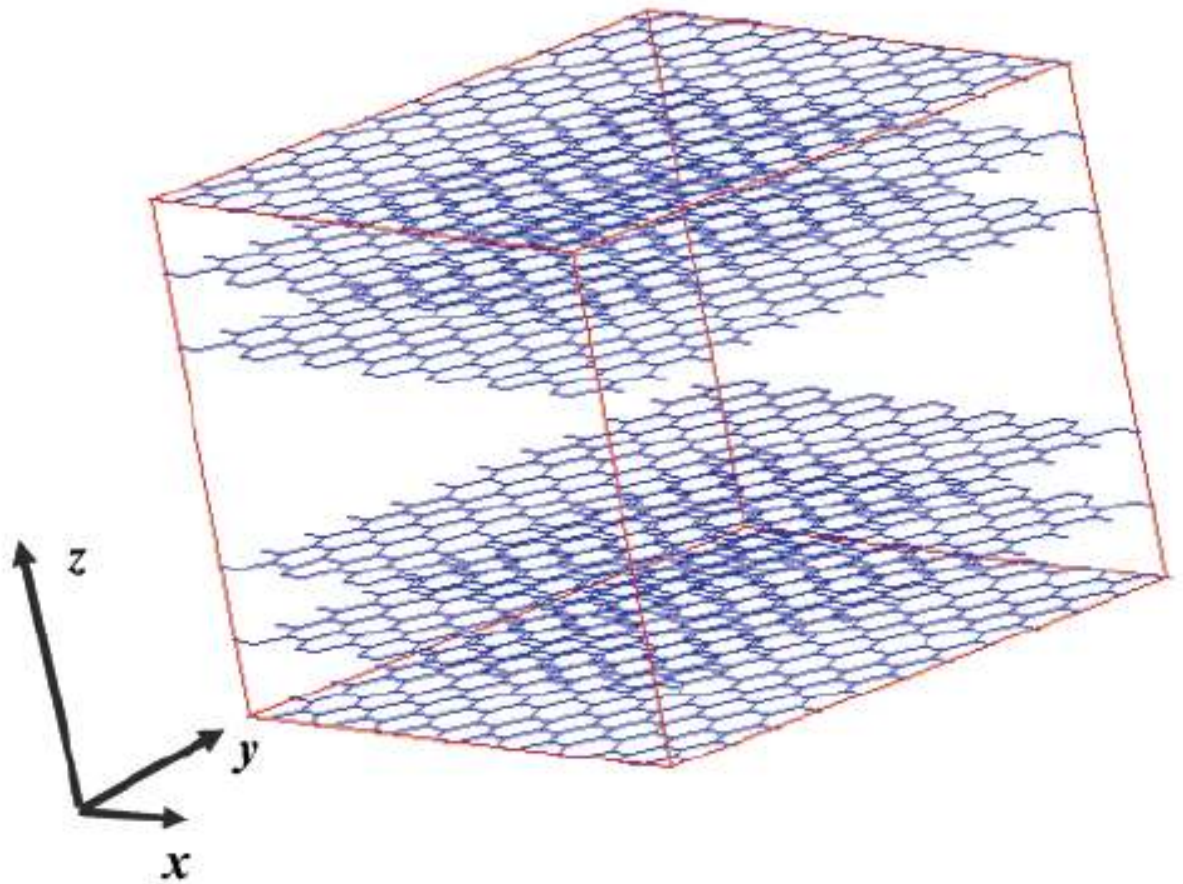


Figure 6.3. Schematic representation for the simulated carbon slit pores. Three carbon layers are considered both above and below the pore. (from reference 25)

Three types of polar surface sites were considered; carboxyl, hydroxyl and carbonyl. Figure 6.4 shows a schematic representation of these surface groups and Table 6.1 lists the geometric parameters.

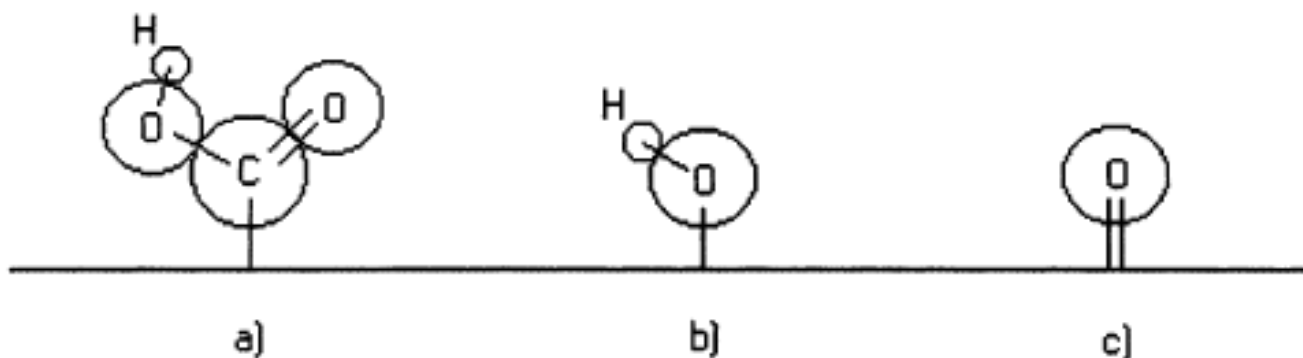


Figure 6.4. Schematic representation of the polar surface sites studied in this work: (a) a carboxyl group; (b) a hydroxyl group; (c) a carbonyl group. (from reference 1)

**Table 6.1. Geometric Parameters for Polar Surface Groups on Graphite Surface.**

	bond	bond length (Å)	angle	amplitude, (deg)
carbonyl	C <sup>a</sup> O	1.0		
hydroxyl	C <sup>a</sup> O	1.233	C <sup>a</sup> OH	110.5
	OH	0.96		
carboxyl	C <sup>a</sup> C	1.52	C <sup>a</sup> CO	111
	C=O	1.214	OCO	123
	CO	1.364	COH	107
	OH	0.97		

<sup>a</sup> Carbon atom in the graphite basal plane. (from reference 1)

PFOA and 1,1-DCE were modeled by using OPLS-AA force field<sup>15-17</sup>. Water molecule was modeled using SPC-E model<sup>18</sup> and 1,4-Dioxane was modeled by the model developed in Chapter 4.

### 6.2.2. Force Field.

We used a pairwise-additive potential which is in the form of 12-6 Lennard-Jones (LJ) plus columbic potential to compute the site-site nonbonded interactions:

$$V_{ij} = 4\varepsilon_{ij} \left[ \left( \frac{\sigma_{ij}}{r_{ij}} \right)^{12} - \left( \frac{\sigma_{ij}}{r_{ij}} \right)^6 \right] + \frac{q_i q_j}{4\varepsilon_0 r_{ij}} \quad (1)$$

where  $i$  and  $j$  are atoms of water, silicalite lattice and defects, and  $r_{ij}$  is the distance between atoms  $i$  and  $j$ .  $\varepsilon_{ij}$  and  $\sigma_{ij}$  are LJ well depth and diameter, respectively.  $q_i$  and  $q_j$  are the partial charges of the interacting sites.

The activated carbon pore interacted with other molecules through the Steele-Potential<sup>19</sup>.

$$V_{Ci}(z) = 2\pi\rho_c \varepsilon_{Ci} \sigma_{Ci}^2 \Delta \left[ \frac{2}{5} \left( \frac{\sigma_{Ci}}{z} \right)^{10} - \left( \frac{\sigma_{Ci}}{z} \right)^4 - \left( \frac{\sigma_{Ci}^4}{3\Delta(z + 0.61\Delta)^3} \right) \right] \quad (2)$$

$V_{Ci}$ , is the energy between the graphite plate and atom  $i$ .  $\rho_c$  is the density of the carbon atoms on the graphite plates,  $\Delta$  is the separation distance between carbon sheets in a single graphite plate,  $z$  is the distance between the graphite plate and an atom in the pore,  $\varepsilon_{Ci}$  and  $\sigma_{Ci}$  are LJ well depth and diameter between the carbon atom of graphite plate and atom  $i$  in the pore, respectively. Steele-Potential models the interaction between the carbon atoms on the activated carbon surface and atoms of other molecules in the pore. Instead of computing the interaction between all carbon atoms on the surface and an atom of a molecule in the pore, it represents all carbon atoms as a field. This accelerates computation time significantly.

Partial charges on the zeolite atoms were taken from the work of Jaramillo et.al.<sup>20</sup> and LJ parameters of the oxygen atom of the silicalite were taken from the work of Snurr et.al.<sup>21</sup> As we explained previously silicon atom of silicalite interacted with the atoms of

sorbate molecules only through the electrostatic potential. OPLS-AA force field which was used to model 1,1-DCE, and PFOA uses geometric mixing rules so LJ terms between unlike atoms of 1,1-DCE, PFOA and oxygen of zeolites were computed using geometric mixing rules.

$$\varepsilon_{ij} = \sqrt{\varepsilon_{ii}\varepsilon_{jj}} \quad \sigma_{ij} = \sqrt{\sigma_{ii}\sigma_{jj}} \quad (3)$$

Table 6.2 lists all non-bonded interaction parameters for zeolite atoms and 1,1-DCE, and PFOA.

**Table 6.2. Non-bonded Forcefield Parameters for Zeolite Atoms and 1,1-DCE, and PFOA.**

Lennard-Jones			Columbic	
Interacting Sites <sup>a</sup>	$\sigma$ (Å)	$\varepsilon$ (K)	Sites	q(e)
Si	0.0	0.0	Si	2.050
OZ	2.806	89.6	OZ	-1.025
CM	3.55	38.2445	CM	0.12 / -0.23 (bonded to Cl / HC~2)
Cl	3.4	150.965	Cl	-0.06
HC~2	2.42	15.0965	HC~2	0.115
C_a	3.75	52.8377	C_a	0.52
CTf	3.5	33.2123	CTf	0.36 / 0.24 (bonded to 3 Fpf / 2Fpf)
Fpf	2.95	26.6705	Fpf	-0.12
HO	0.0	0.0	HO	0.45
O2	2.96	105.6755	O2	-0.44
OHa	3.0	85.5468	OHa	-0.53

CM, Cl, HC~2: carbon, chlorine, hydrogen atoms of 1,1-DCE; CTf: carbon atom bonded to fluorine in PFOA; Fpf: fluorine atom bonded to carbon in PFOA; C\_a: carbon atom of carboxylic acid group in PFOA; O2: oxygen double bonded to the carbon atom of carboxylic group in PFOA; OHa: oxygen atom bonded to carbon and hydrogen of carboxylic group in PFOA; HO; hydrogen atom bonded to oxygen atom of carboxylic group in PFOA. <sup>a</sup> Geometric mixing rules were used to calculate cross terms.

**Table 6.3. Non-bonded Forcefield Parameters for Graphite Plates, Polar Surface Groups, Water and 1,4-Dioxane.**

Lennard-Jones			Columbic	
Interacting Sites <sup>a</sup>	$\sigma$ (Å)	$\epsilon$ (K)	Sites	q(e)
C	4.30	28.0	C	0.5/0.08/0.2 (carbonyl / carboxyl /hydroxyl)
Oonyl	2.96	105.791	Oonyl	-0.5
H	0.0	0.0	H	0.45/0.44 (carboxyl/ hydroxyl)
Ca	3.75	52.8	Ca	0.55
Ohxyl	3.0	85.6	Ohxyl	-0.58
Oxyl	2.96	105.695	Oxyl	-0.50
Oh	3.5	33.2123	Oh	-0.64
CH2c	3.85	51.3	CH2c	-0.25
Oc	2.8	98.0	Oc	0.5
OW	3.1656	78.197	OW	-0.8476
HW	0.0	0.0	HW	0.4238

C: carbon atom on the basal plane of graphite connected to a polar group atom; Oonyl: oxygen atom of carbonyl group; Ca: carbon atom of the carboxyl group; Ohxyl: oxygen atom bonded to hydrogen in the carboxyl group; Oxyl: oxygen atom double bonded to carbon atom in the carboxyl group; Oh: oxygen atom in the hydroxyl group; H: hydrogen bonded to any oxygen atom; OW: oxygen atom of water; HW: hydrogen atom of water; CH2c: methylene united atom in 1,4-Dioxane; Oc: oxygen atom in 1,4-Dioxane. <sup>a</sup> Lorentz-Berthelot mixing rules were used to calculate cross terms.

Partial charges and LJ parameters of the polar surface groups attached to graphite plates were taken from the work of Jorge et.al.<sup>1</sup> LJ terms between unlike atoms of water, 1,4-Dioxane, carbon atom of graphite plate and atoms of polar surface groups were computed using Lorentz-Berthelot mixing rules.

$$\varepsilon_{ij} = \sqrt{\varepsilon_{ii}\varepsilon_{jj}} \quad \sigma_{ij} = \frac{\sigma_{ii} + \sigma_{jj}}{2} \quad (4)$$

Table 6.3 lists all non-bonded interaction parameters for graphite plates, polar surface groups, water and 1,4-Dioxane.

### 6.2.3. Simulations.

All simulations were performed in the NVT ensemble at 298.15 K. In this ensemble number of molecules, volume of the system and temperature are kept fixed. Columbic interactions were handled by the Ewald Sum method.<sup>22</sup> Periodic boundary conditions in all directions were applied in the simulations with zeolites. On the other hand, in the simulations with activated carbon pore periodic boundary conditions were only applied in two directions which are parallel to the graphite surface. The non-bonded potential cutoff distance was 9.5 Å for simulations with silicalite, 9.0 Å for simulations with mordenite and 12.0 Å for simulations with zeolite-beta, zeolite-Y and activated carbon. Four different structures of activated carbon pore were considered in the simulations. One with no polar sites attached and one simulation for each type of polar site attached on the surface of the graphite plates. Four polar sites were placed on each graphite plate totaling in eight polar sites per pore. These polar sites were placed such that they are as far as possible from each other. In the simulations of 1,1-DCE, water and 1,4-Dioxane  $5 \times 10^6$  insertions were performed and in the case of PFOA number of insertions was  $2 \times 10^5$ . One should note that this insertion move is different than the one we sampled in adsorption simulations. In this case a molecule is inserted in to a randomly selected position in the simulation box and after the energy on this test particle is computed, the molecule is removed.

In all simulations Towhee Monte Carlo simulation code was used.<sup>23</sup>

### 6.3. Results and Discussion

#### 6.3.1. PFOA and 1,1-DCE.

In Table 6.4 binding energies and Henry's constants of PFOA and 1,1-DCE are given in four different zeolites. The results for PFOA reveal that zeolite-beta and mordenite have the highest affinities for PFOA followed by zeolite-Y. On the other hand silicalite has no affinity at all for PFOA. Zeolite-beta and zeolite-Y has large pores to accommodate PFOA and the straight channels of mordenite seem to have a perfect fit for PFOA. The pores at the intersection of the straight and zigzag channels of silicalite are known to be favorable sites for adsorbing molecules; however, they are not large enough to accommodate a long chain. It is known that alkanes with long chains are flexible enough to bend themselves<sup>24</sup> but the value of the binding energy of PFOA in silicalite suggest that PFOA does not have this flexibility.

**Table 6.4. Binding Energies and Henry's Constants of PFOA and 1,1-DCE in silicalite, mordenite, zeolite-beta, zeolite-Y.**

	PFOA			
	silicalite	mordenite	zeolite-beta	zeolite-Y
binding energy (kcal /mol)	36.43	-6.82	-7.51	-2.97
Henry's constant (mol / kg . Pa)	$4.44 \times 10^{-34}$	$2.36 \times 10^{-2}$	$8.60 \times 10^{-2}$	$4.50 \times 10^{-5}$
	1,1-DCE			
	silicalite	mordenite	zeolite-beta	zeolite-Y
binding energy (kcal /mol)	-6.12	-5.55	-6.58	-4.60
Henry's constant (mol / kg . Pa)	$6.84 \times 10^{-3}$	$2.75 \times 10^{-3}$	$1.79 \times 10^{-2}$	$7.06 \times 10^{-4}$

Looking at the binding energies for 1,1-DCE we can conclude that all of the zeolites we considered have an affinity towards 1,1-DCE. This affinity is in the order of zeolite-beta > silicalite > mordenite > zeolite-Y.

**Table 6.5. Binding Energies and Henry's Constants of Water and 1,4-Dioxane in activated carbon pore with polar surfaces of carbonyl, carboxyl, and hydroxyl.**

Water				
	no polar group	carbonyl	carboxyl	hydroxyl
binding energy (kcal /mol)	0.14	-1.20	-2.77	-1.52
Henry's constant (mol / m <sup>3</sup> . Pa)	3.19 x 10 <sup>-4</sup>	3.07 x 10 <sup>-3</sup>	4.35 x 10 <sup>-2</sup>	5.28 x 10 <sup>-3</sup>
1,4-Dioxane				
	no polar group	carbonyl	carboxyl	hydroxyl
binding energy (kcal /mol)	16.61	16.62	15.80	16.29
Henry's constant (mol / m <sup>3</sup> . Pa)	2.76 x 10 <sup>-16</sup>	2.65 x 10 <sup>-16</sup>	1.05 x 10 <sup>-15</sup>	4.60 x 10 <sup>-16</sup>

### 6.3.2. Water and 1,4-Dioxane.

In Table 6.5 binding energies and Henry's constants of water and 1,4-Dioxane are given in pure activated carbon and with carbonyl, carboxyl and hydroxyl attached on the surface. While we can say that there is not much an affinity between 1,4-Dioxane and activated carbon, the most important outcome of these figures can be seen when we take a close look at the change in binding energies and Henry's constants at the presence of polar sites. The addition of polar sites increases the binding energy of water significantly resulting in an increase of the Henry's constants by an order of magnitude

one or two. On the other hand, addition of polar sites did not have a significant effect on the binding energy of 1,4-Dioxane except in the case of carboxyl. Having a activated carbon surface with no impurities is simply impossible. These polar groups are always present on the surface and according to the simulation results the polar groups favors the adsorption of water over 1,4-Dioxane. This might be one of the reasons why activated carbon is ineffective to remove 1,4-Dioxane from water.

#### **6.4. Conclusions**

We performed Monte Carlo simulations to investigate the affinity between two hazardous materials, PFOA and 1,1-DCE; and four different zeolites; silicalite, mordenite, zeolite-beta, and zeolite-Y. Binding energies and Henry's constants were computed. For both PFOA and 1,1-DCE zeolite-beta had the highest affinity. The affinity between activated carbon with polar surface groups attached and water, and 1,4-Dioxane were also investigated in attempt to shed light why activated carbon is not effective to remove 1,4-Dioxane from water. Results showed that presence of carbonyl, carboxyl, and hydroxyl groups increased the affinity between water and activated carbon, while the affinity between 1,4-Dioxane and activated carbon was not effected by the presence of polar surface groups.

## Bibliography

1. Jorge, M.; Schumacher, C.; Seaton, N.A., *Langmuir* **2002**, 18, 9296.
2. Vlugt, T.J.H.; Krishna;N., Smit, B., *J. Phys. Chem.* **1999**, 103, 1102.
3. Smit, B.; Siepmann, J.I., *J. Phys. Chem.* **1994**, 98, 8442.
4. Agency for Toxic Substances and Disease Registry (ATSDR). *Toxicological Profile for 1,1-Dichloroethene*. (Update). Public Health Service, U.S. Department of Health and Human Services, Atlanta, GA. 1994.
5. U.S. Department of Health and Human Services. Hazardous Substances Data Bank. National Library of Medicine, National Toxicology Information Program, Bethesda, MD. 1993.
6. U.S. Department of Health and Human Services. Registry of Toxic Effects of Chemical Substances. National Toxicology Information Program, National Library of Medicine, Bethesda, MD. 1993.
7. U.S. Environmental Protection Agency. *Integrated Risk Information System (IRIS) on 1,1-Dichloroethylene*. National Center for Environmental Assessment, Office of Research and Development, Washington, DC. 1999.
8. <http://en.wikipedia.org/wiki/PFOA>
9. <http://www.epa.gov/opptintr/pfoa/index.htm>
10. Zenker, J.M.; Borden, R.C.; Barlaz, M.A., *Env. Eng. Sci.* **2003**, 20, 423.
11. Artioli, G.; Lamberti, C.; Marra, G.L.; *Acta. Cryst. B* **2000**, 56, 2.

12. Gramlich, V. Ph.D. Thesis, ETH, Zürich, Switzerland, (1971).
13. Newsam, J.M.; Treacy, M.M.J.; Koetsier, W.T.; de Gruyter, C.B.; *Proc. R. Soc. Lond. A* **1998**, 420, 375.
14. Hriljac, J.J.; Eddy, M.M.; Cheetham, A.K.; Donohue, J.A.; Ray, G.J., *J. Solid State Chem.* **1993**, 106, 66.
15. W. L. Jorgensen; "OPLS all-atom parameters for organic molecules, ions, & nucleic acids 5/01", available by sending an email to W. L. Jorgensen.
16. G. A. Kaminski; R. A. Friesner; J. Tirado-Rives; W. L. Jorgensen,; *J. Phys. Chem. B* **2001**, 105, 6474.
17. W. L. Jorgensen; "OPLS all-atom parameters for organic molecules, ions, & nucleic acids 12/96", available by sending an email to W. L. Jorgensen.
18. Berendsen, H.J.C.; Grigera, J.R.; Straatsma, T.P., *J. Phys. Chem.* **1987**, 91, 6269.
19. Steele, W. A. *The Interaction of Gases with Solid Surfaces*; Pergamon Press: Oxford, 1974.
20. Jaramillo, E.; Grey, C. P.; Auerbach, S. M. *J. Phys. Chem. B* **2001**, 105, 12319.
21. Snurr, R.Q.; Bell, A.T.; Theodorou, D.N., *J. Phys. Chem.* **1993**, 97, 13742.
22. Ewald, P.P., *Ann. Phys.* **1921**, 64, 253.
23. <http://towhee.sourceforge.net>
24. Maginn, J.E.; Bell, A.T.; Theodorou, D.N., *J. Phys. Chem.* **1995**, 100, 7155.

25. Striolo, A.; Chialvo, A.A.; Cummings, P.T.; Gubbins, K.E., *Langmuir* **2003**, *19*, 8583.

## **7. CONCLUDING REMARKS and RECOMMENDATIONS for FUTURE RESEARCH**

Monte Carlo and Molecular Dynamics simulations were performed to investigate the adsorption of hazardous organics and water in different adsorbents. The simulations in which the adsorption of a pure fluid was investigated turned out very useful information for understanding the factors affecting the adsorption process. On the other hand, in the case of the adsorption of binary mixtures the results were not as successful as they were in the case of single component adsorption simulations.

Extremely low concentrations of the organics in water and the uncertainties introduced by the complex steps of the simulation of the adsorption of binary mixtures could have played a negative role. As a future work, one can study the affinity between hazardous organics and adsorbents in the presence of water in a similar way summarized in Chapter 6. Considering that the hazardous organics are present in water at very low concentrations just evaluating affinities can be a quick alternative over obtaining full isotherms.

Another suggestion for future work is to study the adsorption of molecules which has same functional groups, such as alcohols. This would eliminate the time consuming force field parameterization process as interaction parameters for molecules belonging to the same family are same.

## APPENDIX

**Table 1. Short range Buckingham parameters for zeolite framework atoms and out of framework Na<sup>+</sup> cation. (from references 25 and 48 of Chapter 30)**

$$V_{ij} = \sum_{ij} \left[ A_{ij} e^{-r_{ij}/\rho_{ij}} - \frac{C_{ij}}{r_{ij}^6} \right]$$

species	$A$ (K)	$\rho$ (Å)	$C$ (K Å <sup>6</sup> )
Si-O	206513934.8	0.2049	1571242.395
Al-O	206513934.8	0.2049	1571242.395
O-O	15154249.95	0.3594	2275632.449
Na <sup>+</sup> -O	61155446.23	0.2468	765893.634

**Table 2. Three-body interaction parameters for zeolite framework atoms. (from reference 48 of Chapter 3)**

$$V_{ijk} = \sum_{ijk} \frac{1}{8} \frac{M_{ijk}}{(\theta_0 - \pi)^2} [(\theta_0 - \pi)^2 - (\theta_{ijk} - \pi)^2] e^{-r_{ij}/\rho_1} e^{r_{kj}/\rho_2}$$

species	$M$ (K rad <sup>2</sup> )	$\rho_1$ (Å)	$\rho_2$ (Å)	$\theta_0$ (deg)
O-Si-O	8459862.645	0.3277	0.3277	109.47
O-Al-O	8459862.645	0.3277	0.3277	109.47

**Table 3. Lennard-Jones parameters for MTBE atoms. (from references 20-23 of Chapter 3)**

$$V_{ij} = 4\varepsilon_{ij} \left[ \left( \frac{\sigma_{ij}}{r_{ij}} \right)^{12} - \left( \frac{\sigma_{ij}}{r_{ij}} \right)^6 \right] \text{ with Lorentz-Berthelot mixing rules } (\varepsilon_{ij} = \sqrt{\varepsilon_{ii}\varepsilon_{jj}} \text{ and } \sigma_{ij} = \frac{\sigma_{ii} + \sigma_{jj}}{2})$$

species	$\sigma$ (Å)	$\varepsilon$ (K)
CH <sub>3</sub>	3.75	98.0
O	2.80	55.0
C	5.80	0.5

**Table 4. Intramolecular terms for MTBE. (from references 20-23 of Chapter 3)**

Bond stretching: bond lengths are fixed

species	Distance (Å)
CH <sub>3</sub> -O	1.41
C-O	1.41
CH <sub>3</sub> -C	1.54

$$\text{Angle bending: } V_{ij} = \frac{k}{2} (\theta - \theta_0)^2$$

species	$\theta_0$ (deg)	$k$ (K)
CH <sub>3</sub> -O-C	112.0	60400.0
O-C-CH <sub>3</sub>	112.0	50300.0
CH <sub>3</sub> -C-CH <sub>3</sub>	109.47	62500.0

$$\text{Torsion: } V_{ijkl} = c_0 + c_1(1 + \cos(\phi)) + c_2(1 - \cos(2\phi)) + c_3(1 + \cos(3\phi))$$

species	$c_0$ (K)	$c_1$ (K)	$c_2$ (K)	$c_3$ (K)
CH <sub>3</sub> -O-C-CH <sub>3</sub>	0	725.35	-163.75	558.20